IntechOpen

Accuracy of GNSS Methods

Edited by Dogan Ugur Sanli

ACCURACY OF GNSS METHODS

Edited by **Dogan Ugur Sanli**

Accuracy of GNSS Methods
http://dx.doi.org/10.5772/intechopen.75424
Edited by Dogan Ugur Sanli

Contributors

Olalekan Isioye, Mefe Moses, Abdulmumin Lukman, Ha Minh Hoa, Mustafa Ulukavak, Enik Shytermeja, Emilia Correia, Marcio Muella, Lucilla Alfonsi, Fabricio Prol, Paulo Camargo, Dr. Wang, Dogan Ugur Sanli

© The Editor(s) and the Author(s) 2019
The rights of the editor(s) and the author(s) have been asserted in accordance with the Copyright, Designs and Patents Act 1988. All rights to the book as a whole are reserved by INTECHOPEN LIMITED. The book as a whole (compilation) cannot be reproduced, distributed or used for commercial or non-commercial purposes without INTECHOPEN LIMITED's written permission. Enquiries concerning the use of the book should be directed to INTECHOPEN LIMITED rights and permissions department (permissions@intechopen.com).
Violations are liable to prosecution under the governing Copyright Law.

Individual chapters of this publication are distributed under the terms of the Creative Commons Attribution 3.0 Unported License which permits commercial use, distribution and reproduction of the individual chapters, provided the original author(s) and source publication are appropriately acknowledged. If so indicated, certain images may not be included under the Creative Commons license. In such cases users will need to obtain permission from the license holder to reproduce the material. More details and guidelines concerning content reuse and adaptation can be foundat http://www.intechopen.com/copyright-policy.html.

Notice

Statements and opinions expressed in the chapters are these of the individual contributors and not necessarily those of the editors or publisher. No responsibility is accepted for the accuracy of information contained in the published chapters. The publisher assumes no responsibility for any damage or injury to persons or property arising out of the use of any materials, instructions, methods or ideas contained in the book.

First published in London, United Kingdom, 2019 by IntechOpen
eBook (PDF) Published by IntechOpen, 2019
IntechOpen is the global imprint of INTECHOPEN LIMITED, registered in England and Wales, registration number: 11086078, The Shard, 25th floor, 32 London Bridge Street
London, SE19SG – United Kingdom
Printed in Croatia

British Library Cataloguing-in-Publication Data
A catalogue record for this book is available from the British Library

Additional hard and PDF copies can be obtained from orders@intechopen.com

Accuracy of GNSS Methods
Edited by Dogan Ugur Sanli

p. cm.

Print ISBN 978-1-78984-925-7

Online ISBN 978-1-78984-926-4

eBook (PDF) ISBN 978-1-83881-824-1

Meet the editor

Dogan Ugur Sanli obtained his PhD from Newcastle University, UK. For his PhD thesis, he studied sea level rise using GPS. In particular, he specialized in vertical crustal deformation monitoring using GPS. He then moved into the area of GPS positioning accuracy and he managed to model both vertical and horizontal accuracy for relative-PPP and PPP. He also studied GPS positioning accuracy for rapid-static positioning for BERNESE and OPUS-RS software. He has also continued to co-author sea level studies. He was involved in NEAMTWS Tsunami Warning efforts under the auspices of UNESCO. He was a member of Sea Level Working Group 3. Currently he is interested in assessing the accuracy of GPS positioning velocities with the focus on PPP derived positions from repeated GPS surveys.

Contents

Preface

GPS has revolutionised the history of positioning in terms of monitoring global deformations of the earth and in the establishment of geodetic control networks. It followed the mission of its predecessor TRANSIT by producing more accurate position information and enabling far better achievements. As a young PhD student, I was always amazed that the GPS results were changing (sometimes significantly) when applying different processing strategies on the same data! Following my PhD, I have spent more than two decades studying analysis and surveying strategies to assess GPS positioning and velocity accuracies.

Studying the positioning accuracy of satellite systems is important considering the wide variety of surveying methods, software, equipment, and processing strategies available. Furthermore, the quality of satellite orbits, terrestrial reference frames (TRF), atmospheric models, etc. is continuously improved by the development of new mathematical theories by their vendors. Therefore, various combinations of the above items in producing results would terminate in different positioning accuracies. For this reason, research assessing the accuracy of satellite positioning techniques should keep playing a key role in the future. Our era is now prone to the emergence of new satellite positioning systems called Global Navigation Satellite Systems (GNSS). Almost nearing the quality of GPS is the satellite positioning system of Russia's GLONASS, which is already available on the market today. Another two systems that are nearing completion are the European's GALILEO and China's BeiDou. There are also other satellite positioning systems that are especially developed to serve their countries such as Japan's Quasi-Zenith Satellite System (QZSS) and India's Regional Navigation Satellite System (IRNSS).

Researchers have spent a lot of time improving the positioning accuracy of GPS either by experience from various geophysical experiments or directly developing new mathematical and analysis theories followed by the new instrumentation providing the data. With the emergence of the new GNSS, multi-GNSS experiments designed by the International GNSS Service (IGS) were carried out. In this book, I aimed to gather results from various GNSS techniques and methodologies as well as multi-GNSS experiments assessing positioning accuracy. My mind is now broadened since the book contains accuracy results not only based on the application of different processing and surveying strategies but also based on designing new receiver infrastructures to improve the quality of GNSS signal, assessing performance status of GNSS constellations, and assessing the accuracy of GNSS signal under the effect of severe atmospheric disturbances such as scintillations in the ionosphere. Therefore, the book title has been given as "Accuracy of GNSS methods". With the term "accuracy", we mean "the accuracy of the results delivered by the method". I hope this book will emphasize the crucial role of the accuracy assessment and make the necessary impact on future generations.

The IGS has been home to GPS products for more than two decades now with the effort of colleagues from different nations. This period corresponds to my past career life! Therefore, I am indebted to the IGS, which played a crucial role in my entire career and its motivation to young researchers, GPS data, and various other products. I hope IGS will also be host to upcoming GNSS products and activities. We have witnessed it with applications such as the Multi GNSS Experiment (MGEX).

Before I leave the reader alone with the book, I would like to mention the name of my teacher, my PhD supervisor, Professor Geoffrey Blewitt. I first heard the term "processing strategy" from him. Last but not least, I also thank him for inspiring me and introducing me to those magic words that were going to take most of my time in doing research throughout my career.

Dogan Ugur Sanli
Department of Geomatic Engineering
Civil Engineering Faculty
Yildiz Technical University
Istanbul, Turkey

Section 1

Introduction

Chapter 1

Introductory Chapter: The Philosophy Behind the Accuracy Assessment of GNSS Methods

Dogan Ugur Sanli

Additional information is available at the end of the chapter

http://dx.doi.org/10.5772/intechopen.81288

1. Introduction

Satellite geodesy was developed to overcome the tasks which cannot be accomplished using traditional geodetic techniques, for instance, to measure the motion of continents more precisely, to eliminate the difficulty in line of site problems, to gain performance in all weather conditions, and to be able to monitor global deformations of the earth leading to the contribution in the emerge of a terrestrial reference frame (TRF) which is compatible with the geodynamic events of the earth.

Today, global navigation satellite system (GNSS) data are used for various purposes, not only in geodesy but also in all earth science disciplines such as geophysics, geology, meteorology, oceanography, and others. In geodesy, applications range from establishing geodetic control networks to detail surveys. The GNSS instrumentation is designed according to various purposes. Cost-effective instrumentation, hardware, and software are preferred suitable to application and accuracy expectations. The accuracy expectation of users according to their aims is multifold. The instrumentation and the GNSS products are always improved with the developments in technology and analysis methodologies, coding, etc. Hence the user, the GNSS community, needs to be updated in terms of accuracy of the positioning results, orbital products, TRF quality, etc. with continuous research.

2. Positioning accuracy of GNSS

The accuracy of GNSS was studied by many researchers; however, the first organized study in which the accuracy prediction formulas for coordinate components were developed for the user was produced by [1] based on an experiment using only GPS data. There the authors emphasized that the accuracy of GNSS positioning was mainly dependent on observation session duration. The dependency on baseline length, which for instance was the essence as emphasized in [2–4], was mainly changed with the release of the IGS precise orbit (i.e., with the improvement in orbit quality).

Eckl et al. [1] were targeting GPS studies at the national level with Continuously Operating Reference Station (CORS) inter-station distances of up to 300 km. Sanli and Engin [5] changed the angle to tectonic studies in which GPS processing was handled using baseline lengths of up to thousands of kilometers. Again, the dependency on baseline length came back to the agenda. From these studies the authors produced prediction formulas for north, east, and up positioning components. The formulas were useful for the GPS community with various accuracy expectations for various applications. Before field works, they were able to obtain a priory accuracy levels and hence taking necessary precautions in the field to guarantee the desired position accuracy.

Then, the research continued to present details in the accuracy assessment of point positions. For instance, Ozturk and Sanli [6] made an attempt to unify accuracy models for baselines of 1–3000 km resulting in a complete accuracy model. Sanli and Kurumahmut [7] took into account the effect of large height difference on positioning and extended the traditional formulation. Ghoddousi-Fard and Dare [8] were among those who studied the accuracy of GPS positioning for web-based GPS software. Schwarz et al. [9] and Hastaoglu and Sanli [10] assessed the accuracy of GPS rapid static positioning. At the end of the day, GPS positioning accuracy prediction formulas from static GPS surveys were produced for three major GNSS software, Bernese, GIPSY/OASIS II, and GAMIT by [11–13], respectively.

3. Scope of book

Besides the GPS positioning accuracy efforts that are well documented in the literature and discussed above, this book embraces the present day work documenting the performance evaluation of GNSS systems and new receiver designs to improve GNSS signal quality before the processing. The up-to-date experiment results on positioning accuracy are also evaluated for online GNSS software which is freely available to user community. In addition, the positioning accuracy under severe atmospheric disturbances is evaluated for single-frequency receivers which are widespread in surveying practice today. The structure of the sections and chapters is as in the following:

In the first section, the performance of the two GNSS systems, GPS and BeiDou, is evaluated. Referring to well-established standards developed for the GPS, the performance assessment of BeiDou satellite navigation system is performed. The available signal in space (SIS) model is improved based on the reliability theory using exponential distribution and Gauss-Markov process, and constellation models are refined taking into consideration satellite failure rate, repair rate, and backup situation.

The second section reviews the quality of the GNSS measurements. In the first chapter, a new GNSS receiver design in which the GNSS signal is repaired using a new vector tracking architecture is proposed. In the second chapter, how the GNSS signal is degraded under severe atmospheric disturbances such as ionospheric scintillations is investigated. A calibration model improving single-frequency PPP results is presented.

The third section is devoted to GNSS positioning assessments:

Chapter 1 in Section 3 assesses GPS relative positioning accuracy for a single-frequency GPS receiver. Single-frequency receivers are economic and suitable for nationwide surveying practices. Therefore, researchers are eager to develop methodologies in which single-frequency receivers are employed. Here the positioning accuracy is assessed taking into consideration the mode of surveying, baseline, and precision dilution of position (PDOP), signal-to-noise ratio (SNR), and occupation time. Chapters 2 and 3 in this section assess results from online GNSS software. Results from available software are compared. Chapter 2 presents results in ITRF14 and Chapter 3 in a national grid system.

The fourth section is devoted to the construction of national spatial reference systems by combining terrestrial geodetic networks with GNSS networks. A recurrent adjustment methodology which uses GPS data from GNSS methods is presented applying sparse matrix operations, outlier detection, and simplified subsystem of observation equations. Namely, present day accuracy of establishing national spatial reference systems based on GNSS is presented.

Author details

Dogan Ugur Sanli

Address all correspondence to: usanli@yildiz.edu.tr

Yildiz Technical University, Turkey

References

[1] Eckl MC, Snay RA, Soler T, Cline MW, Mader GL. Accuracy of GPS-derived relative positions as a function of inter-station distance and observing-session duration. Journal of Geodesy. 2001;**75**:633-640

[2] Dong DN, Bock Y. Global positioning system network analysis with phase ambiguity resolution applied to crustal deformation studies in California. Journal of Geophysical Research. 1989;**94**(B4):3949-3966

[3] Larson KM, Agnew DC. Application of the global positioning system to crustal deformation measurement, 1, precision and accuracy. Journal of Geophysical Research. 1991;**96**(B10):16547-16565

[4] Feigl KL, Agnew DC, Bock Y, Dong D, Donellan A, Hager BH, et al. Space geodetic measurement of crustal deformation in central and Southern California, 1984-1992. Journal of Geophysical Research. 1993;**98**(B12):21677-21712

[5] Sanli DU, Engin C. Accuracy of GPS positioning over regional scales. Survey Review. 2009;**41**:192-200

[6] Ozturk D, Sanli DU. Accuracy of GPS positioning from local to regional scales: A unified prediction model. Survey Review. 2011;**43**:79-589

[7] Sanli DU, Kurumahmut F. Accuracy of GPS positioning in the presence of large height differences. Survey Review. 2011;**43**(320):162-176

[8] Ghoddousi-Fard R, Dare P. Online GPS processing services: An initial study. GPS Solutions. 2006;**10**:12-20

[9] Schwarz CR, Snay RA, Soler T. Accuracy assessment of the national geodetic survey's OPUS-RS utility. GPS Solutions. 2009;**13**:119-132

[10] Hastaoglu KO, Sanli DU. Monitoring Koyulhisar landslide using rapid static GPS: A strategy to remove biases from vertical velocities. Natural Hazards. 2011;**58**:1275-1294

[11] Doğan U. Accuracy analysis of relative positions of permanent GPS stations in the Marmara region, Turkey. Survey Review. 2007;**39**:156-165

[12] Sanli DU, Tekic S. Accuracy of GPS precise point positioning: A tool for GPS accuracy prediction. Saarbrücken: LAP Lambert Academic Publishing; 2010. 60 p

[13] Firuzabadi D, King RW. GPS precision as a function of session duration and reference frame using multi-point software. GPS Solutions. 2012;**16**:191-196

Section 2

Performance Evaluation of GNSS

Chapter 2

Evaluation Methods of Satellite Navigation System Performance

Ershen Wang, He He and Chaoying Jia

Additional information is available at the end of the chapter

http://dx.doi.org/10.5772/intechopen.81034

Abstract

With the development of global satellite navigation system, for example, global positioning system (GPS) and so on, some regional navigation systems and augmentation systems are developing rapidly. The continuous development of satellite navigation system has attracted the users' attention to satellite navigation performance, which makes the navigation system performance become the key of satellite navigation system competition in the field of GNSS applications. The signal in space (SIS) continuity evaluation model based on the reliability is established, and the mean time between failures (MTBF) is used to characterize the probability that there is no continuity loss in unit time. Aiming at the incompleteness of the current availability model, a per-satellite availability evaluation models based on Markov process is established. Moreover, the constellation availability evaluation model is proposed by combining the satellite failure rate, repair rate and backup situation. By analyzing the measured data, the probability of the continuity and availability of GPS and BeiDou Navigation Satellite System (BDS) are calculated respectively. The results are instructive for the study of the availability performance monitoring and the evaluation of global BDS.

Keywords: GNSS, performance evaluating, accuracy, integrity, availability

1. Introduction

With the development of global satellite navigation system, for example, GPS and so on, some regional navigation systems and augmentation systems are developing rapidly. The continuous development of satellite navigation system has attracted the users' attention to satellite navigation performance, which makes the navigation system performance become the key of satellite navigation system competition in the field of GNSS application [1–4]. Meanwhile, the

IntechOpen

compatibility, interoperability and service performance of GNSS have become an important issue regarding the system construction and the users' requirements [5]. However, there is not a unified standard for satellite navigation service, e.g., there are non-negligible differences in the indicators of each navigation system [6–8], including the name, the manner and the prescribed scope. GPS is the earliest construction and longest-developing satellite navigation system. Since its official operation, research on GPS performance has continued, and the results are relatively rich [9]. So far, there are four different versions of the "GPS Standard Positioning Service Performance Standard" [10–13], this document was published by the US Department of Defense and played a leading role in the development of satellite navigation system performance evaluation systems. In addition, in order to ensure the safe and efficient operation of GPS and its enhanced systems WAAS and LAAS, and to analyze the navigation performance and the cause of service interruption, the United States Federal Aviation Administration (FAA) has set the GPS Standard Positioning Service (GPS SPS) and wide area enhancement since 1993. The performance of the system (WAAS) is monitored and analyzed, and a corresponding performance analysis report is provided on a quarterly basis [14]. Amongst existing standards, the GPS Standard Positioning Service Performance Standards released by USA is more widely used to evaluate satellite navigation systems [15].

Each stage of a satellite navigation system is inseparable from its performance assessment. The performance evaluation of a navigation system can not only verify whether the performance meets the original design requirements, but also monitor the operating status of the system in real time, provide a basis for performance enhancement of the system, and promote the modernization process of the navigation system [16]. Therefore, in the development of satellite navigation systems, the evaluation of the performance of navigation systems has become a very important part.

At present, China's Beidou satellite navigation system has been able to be compatible with other satellite navigation systems. The development of Beidou satellite navigation system follows the "three-step" strategy, namely: firstly to achieve navigation services in China, secondly to achieve regional navigation services in the Asia-Pacific region, and finally to build a global satellite navigation system with global navigation capabilities. Now it has completed the construction of the second-step regional navigation system and will achieve global coverage in 2020.

The construction of BDS has very important practical significance, but at present it has not yet established a complete performance evaluation system, and it faces severe performance test evaluation problems [17]. Therefore, considering the construction and subsequent development of BDS in China, it is very necessary to carry out research on the performance evaluation method of the satellite navigation system. In-depth analysis of the evaluation index system and method, and the use of measured data to verify it, in order to establish a sound BDS performance evaluation system to accumulate certain experience.

2. Evaluation algorithm of GNSS signal in space availability

There are lots of researches working on per-satellite availability and constellation availability. Ochieng et al. established a per-satellite availability evaluation model that calculates instantaneous availability based on failure rate and reliability without considering on-orbit restoration performance [18]. In fact, most satellite failures can be restored by ground control segments or resolved by spare satellites. Based on this, Section 2.1 mainly introduces and analyzes the definition and performance evaluation indicators of GNSS. Based on the "GPS Standard Positioning Service Performance Standards" and "Beidou Satellite Navigation System Open Service Performance Specification", the accuracy, integrity, continuity and availability definition as well as evaluation indicators of GPS and BDS are analyzed respectively, which is convenient for subsequent performance evaluation. The results provide the basis. In Section 2.1.2, the SIS availability of GPS and BDS are evaluated and analyzed. The model of satellite availability algorithm is constructed based on the Markov process. Based on the evaluation models, the performance of GPS SIS and BDS SIS is evaluated by using the measured data in Section 2.2. Finally, combined with the backup situation of satellites, the constellation availability evaluation models of SIS and service are proposed in Section 2.3.

2.1. Satellite navigation system performance evaluation criteria

Accuracy, integrity, continuity and availability are the four basic properties of satellite navigation systems. Performance indicators and assessment methods vary for different navigation systems. Compared with GLONASS and Galileo, GPS navigation system is more perfect for performance evaluation indicators and results, especially the release of GPS SPS PS, which is the leading direction of satellite navigation system performance standards and evaluation system.

2.1.1. Standard positioning service performance standard of GPS

GPS is the first satellite navigation system to perform performance evaluation, and its civilian standard location service is applicable to civilian users (L1 C/A code) worldwide. Compared with the precision positioning service and the enhanced system WAAS service, the civilian standard positioning service has the lowest positioning accuracy, but the user quantity is the largest.

Up to now, the US Department of Defense has released four versions of GPS SPS PS to show GPS service performance to users around the world [10–13]. Based on the comprehensive comparison, it is found that with the improvement of GPS performance level, the relevant performance evaluation theory is gradually improved. In the late 1990s, GPS service performance was greatly improved by the implementation of a series of performance enhancement programs. With the cancelation of the optional availability SA policy, the third edition of the GPS SPS PS released in 2001 was revised accordingly. Although the overall framework has not changed, the connotation of the accuracy index has changed a lot, the index parameters of the SIS precision are compressed, and the service reliability is also redefined. At present, the latest version of GPS SPS PS was released in 2008. Based on the summary of the first three editions, the original index system was reorganized and improved.

2.1.2. Satellite navigation system public service performance specification of Beidou

The space segment of the Beidou satellite navigation system consists of five geostationary orbit (GEO) satellites, 27 medium-Earth orbit (MEO) satellites and three inclined geosynchronous orbit (IGSO) satellites. Taking into account the characteristics of the BDS, the China Satellite Navigation System Management Office released the BDS-OS-PS-1.0, which is used to illustrate the performance characteristics and indicators of the public service B1I signal in the regional phase of the Beidou satellite navigation system [19, 20].

2.2. SIS evaluation algorithm based on Markov process

GPS SPS PS pointed out that the availability of navigation system refers to the percentage of time that the navigation system can provide users with available services within its service area, which characterizes the service capability of satellite navigation systems [13]. As one of the four basic service performances of satellite navigation systems, usability has become a key performance indicator in civil aviation and other application fields, and is an important basis for judging whether the navigation system is reliable [21, 22]. The usability study content of the four released versions of GPS SPS PS is compared, and the development trend is shown in **Table 1**.

SIS from the development trend of the availability indicators is given in **Table 1**, as the research progresses, the availability of satellites is gradually divided into SIS layer availability and service layer availability, and SIS availability is receiving more and more attention.

SIS availability can be described in terms of per-satellite availability and constellation availability [13]. From the definition of availability, the availability of SIS is essentially an assessment of satellite availability, i.e., the availability of per-satellite is analyzed, and then the study of per-satellite availability transitions to constellation availability, which in turn reflects the SIS availability of all satellites.

2.2.1. Evaluation model for per-satellite availability

The instantaneous reliability function of a satellite is given in the literature, which only considered the failure rate but ignored the restoration rate. In fact, part of satellite failures can be resolved by the repair of ground control section or the backup of spare satellites. And this is one of the functions of the Markov chain. The life distribution and the failure restoration time distribution are assumed to follow exponential distributions. As long as the satellite navigation system status is given properly, the system can always be described by the Markov process [23, 24]. The exponential distribution model is used to describe the reliability of the satellites in many of the literature. When the failure rate of a satellite is assumed to be of exponential distribution, the Markov state transition process of per-slot is shown as **Figure 1**.

GPS SPS PS document	Research content
1993 edition	Service availability standard
1995 edition	Service availability standard
2001 edition	SPS Service Availability Standard, PDOP Availability Standard
2008 edition	SIS Availability Standard, SPS Service Availability Standard, PDOP Availability Standard

Table 1. Comparison of GPS SPS PS to usability research content.

In **Figure 1**, 0 indicates the system status is normal; 1 indicates the system status is failed; λ is the failure rate of satellite, it is the inverse of mean time between failure (MTBF); μ is the restoration rate of satellite, it is the inverse of mean time to restoration (MTTR); and Δt is the time interval of state transition.

According to reliability theory [25, 26], we can get the instantaneous availability of per-slot by utilizing the Markov state transition process:

$$A(t) = \frac{\mu}{\lambda+\mu} + \frac{\lambda}{\lambda+\mu} e^{-(\lambda+\mu)t}. \tag{1}$$

In order to express the per-slot availability more reasonably, when $t \to \infty$, we get the steady state availability of per-slot through formula (1), and it would be as follows:

$$A = \frac{\mu}{\lambda+\mu}. \tag{2}$$

According to the relationship between and MTBF, and the relationship between and MTTR, formula (1) is equivalent to:

$$A = \frac{MTBF}{MTBF + MTTR}. \tag{3}$$

where A is the per-satellite availability; $MTBF$ is the reciprocal of λ, and $MTTR$ is the reciprocal of μ.

In **Figure 2**, λ_i ($i = 1, 2, 3, 4$) is the satellite failure rate of different failure type. μ_i ($i = 1, 2, 3, 4$) is the satellite restoration rate of different failure type. Considering the influence of different failure type, the satellite failure rate λ and the satellite restoration μ rate in formula (2) are equivalent to the following formula:

$$\begin{cases} \lambda = \lambda_1 + \lambda_2 + \lambda_3 + \lambda_4 \\ \mu = \dfrac{\lambda}{\dfrac{\lambda_1}{\mu_1} + \dfrac{\lambda_2}{\mu_2} + \dfrac{\lambda_3}{\mu_3} + \dfrac{\lambda_4}{\mu_4}} \end{cases}. \tag{4}$$

2.2.2. *Evaluation algorithm for constellation availability*

In the previous constellation availability models [27], a specific constellation with a defined number (generally 24) of space vehicles was considered, when more space vehicles than required for the constellation have actually been on orbit for most of the time since the declaration of Full

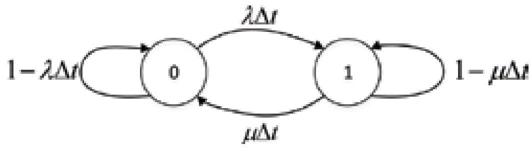

Figure 1. Markov state transition process of per-slot.

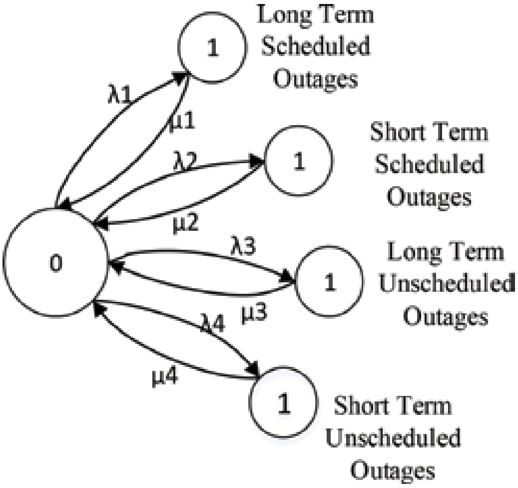

Figure 2. Markov state transition process of satellite based on different failure types.

Operational Capability (FOC); Zheng and Ren pointed out that a study on constellation availability is based on per-satellite availability, and MTBF and MTTR of different per-satellite outages directly influence constellation availability in different states [28]; U.S. Department of Defense refers that constellation availability model is based on binomial probability distribution [15], and it can be described as the following formula:

$$p(k) = C_N^k (1 - A)^k A^{N-k}. \tag{5}$$

where, $p(k)$ is the constellation availability when there are faulted satellites. N represents the total number of satellites in the constellation. k is the number of faulted satellites, and A is the availability of per-satellite.

Formula (5) calculates the constellation availability based on the stationary state of per-satellite availability. The model calculates the availability of the constellation based on the availability of per satellite steady-state. Although it reflects the availability of the constellation under different fault conditions to some extent, it ignores the impact of satellite backup strategy on constellation availability and is a relatively static constellation availability. The availability of constellations is affected by many factors. Because the factors affecting the state of the constellation are more complicated, this section proposes a mathematical model of constellation availability considering the satellite's failure rate, repair rate and backup situation based on the traditional constellation availability model.

Let's explain the state of the constellation: suppose the constellation consists of a basic orbital satellite and a non-orbital satellite. When there is no satellite failure, the state of the constellation is N. if there is a failure of the basic orbital satellite, and the faulty satellite is replaced by the non-orbiting satellite in time, the state of the constellation is considered to have not changed. If the failed satellite is not replaced by the non-orbital satellite in time, the state of the constellation will change. When the base orbit satellite fails, the ground control station will repair the faulty satellite while replacing the non-orbital satellite, and only repair one satellite at a time.

Failure state of constellation system will change with the number of failed satellites. Therefore, on the condition of the above assumptions, the failure state spaces of baseline satellites and spare satellites respectively are $\{0, 1, 2, \cdots, N\}$ and $\{0, 1, 2, \cdots, M\}$. The SIS constellation availability model based on Markov chain is set up. In addition, this model the baseline satellites constellation availability and the spare satellites constellation availability are considered respectively. Moreover, the backup situations of spare satellites are combined with the failure state of baseline satellites constellation. Finally, the availability of whole constellation system can be attained.

$\lambda_i (i = 1, 2, 3, \cdots, N)$ are used to indicate the failure rates of baseline satellites constellation; $\mu_i (i = 1, 2, 3, \cdots, N)$ are used to indicate the restoration rates of baseline satellites constellation, and both failure rates and restoration rates are on different failure conditions. The corresponding Markov failure state transition process of baseline satellites is shown in **Figure 3**.

In **Figure 3**, $\lambda_i = C_{N+1-i}^1 \cdot \lambda \cdot (1-\lambda)^{N-i} (i = 1, 2, \cdots, N)$ (λ is the average failure rates of N baseline satellites); $\mu_i = C_i^1 \cdot \mu \cdot (1-\mu)^{i-1} (i = 1, 2, \cdots, N)$ (μ is the average restoration rates of N baseline satellites).

If the state of failure state space is i at the time of t, then the probability of this situation can be indicated with $G_i(t)(i = 0, 1, 2, \cdots, \mathrm{N})$, and assuming that the time of initial state is $t = t_0$. When time increases to $t = t_0 + \Delta t$, the probability that the baseline constellation not having failed satellites is:

$$G_0(t_0 + \Delta t) = G_0(t_0) \cdot (1 - \lambda_1 \Delta t) + G_1(t_0) \cdot \mu_1 \Delta t \tag{6}$$

The failure state space of baseline constellation also has other states, and the probability of these states is as follows:

$$G_1(t_0 + \Delta t) = G_0(t_0) \cdot \lambda_1 \Delta t + G_1(t_0) \cdot \left(1 - \left(\lambda_2 + \mu_1\right)\Delta t\right) + G_2(t_0) \cdot \mu_2 \Delta t \tag{7}$$

$$G_2(t_0 + \Delta t) = G_1(t_0) \cdot \lambda_2 \Delta t + G_2(t_0) \cdot \left(1 - \left(\lambda_3 + \mu_2\right)\Delta t\right) + G_3(t_0) \cdot \mu_3 \Delta t \tag{8}$$

$$G_{N-1}(t_0 + \Delta t) = G_{N-2}(t_0) \cdot \lambda_{N-1} \Delta t + G_{N-1}(t_0) \cdot \left(1 - \left(\lambda_N + \mu_{N-1}\right)\Delta t\right) + G_N(t_0) \cdot \mu_N \Delta t \tag{9}$$

$$G_N(t_0 + \Delta t) = G_{N-1}(t_0) \cdot \lambda_N \Delta t + G_N(t_0) \cdot \left(1 - \mu_N \Delta t\right) \tag{10}$$

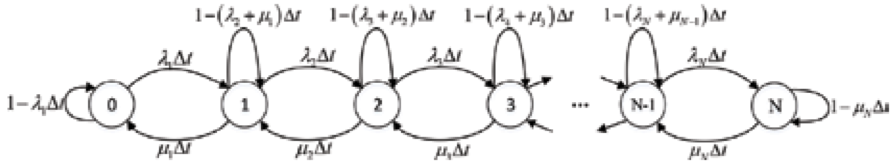

Figure 3. Markov failure state transition process of baseline constellation.

Failure state space of baseline constellation has different states in different time. The formulas (6)–(10) can be shown by matrix form, then the probabilities of the above different states can be expressed as:

$$\vec{G}(t_0 + k\Delta t) = \vec{G}(\Delta t) \cdot \vec{G}(t_0 + (k-1)\Delta t) \tag{11}$$

Therefore,

$$\left\{ \begin{array}{l} \vec{G}(t_0 + k\Delta t) = [G_0(t_0 + k\Delta t) \;\; G_1(t_0 + k\Delta t) \;\; \cdots \;\; G_N(t_0 + k\Delta t)]^T, \\ \vec{G}(t_0 + (k-1)\Delta t) = [\,G_0(t_0 + (k-1)\Delta t) \quad G_1(t_0 + (k-1)\Delta t) \quad \cdots \quad G_N(t_0 + (k-1)k\Delta t)\,]^T, \\ \vec{G}(\Delta t) = \begin{bmatrix} 1-\lambda_1\Delta t & \mu_1\Delta t & 0 & 0 & \cdots & \cdots & 0 & 0 & 0 \\ \lambda_1\Delta t & 1-(\lambda_2+\mu_1)\Delta t & \mu_2\Delta t & 0 & \cdots & \cdots & \vdots & \vdots & \vdots \\ 0 & \lambda_2\Delta t & 1-(\lambda_3+\mu_2)\Delta t & \mu_3\Delta t & 0 & \vdots & \vdots & \vdots & \vdots \\ \vdots & 0 & \vdots & \vdots & \vdots & \ddots & \vdots & \vdots & \vdots \\ \vdots & \vdots & \vdots & \vdots & \vdots & \vdots & \vdots & \ddots & 0 \\ 0 & \cdots & \cdots & \cdots & 0 & 0 & \lambda_{N-1}\Delta t & 1-(\lambda_N+\mu_{N-1})\Delta t & \mu_N\Delta t \\ 0 & \cdots & \cdots & \cdots & 0 & 0 & 0 & \lambda_N\Delta t & 1-\mu_N\Delta t \end{bmatrix} \end{array} \right.$$

According to the formula (11) and the initial condition, the probabilities of different states of baseline constellation after the time of $T = k\Delta t$ can be calculated.

Similar to the baseline constellation, failure state space of spare satellites constellation also has different states in different time. And the probabilities of these states can be expressed as:

$$\vec{F}(t_0 + k\Delta t) = \vec{F}(\Delta t) \cdot \vec{F}(t_0 + (k-1)\Delta t) \tag{12}$$

According to the formula (12) and the initial condition of spare satellites constellation, the probabilities of different states of spare satellites constellation after the time of $T = k\Delta t$ can be also calculated.

Both baseline constellation and spare satellites constellation have important influence on SIS constellation availability. Considering these influences comprehensively, the model of SIS constellation availability is considered:

$$\left\{ \begin{array}{l} P_s(t_0 + k\Delta t) = G_0(t_0 + k\Delta t) + G_1(t_0 + k\Delta t) \cdot (F_0(t_0 + k\Delta t) + F_1(t_0 + k\Delta t) + \cdots + F_{M-1}(t_0 + k\Delta t)) \\ \qquad + G_2(t_0 + k\Delta t) \cdot (F_0(t_0 + k\Delta t) + F_1(t_0 + k\Delta t) + \cdots + F_{M-2}(t_0 + k\Delta t)) + \cdots \\ \qquad + G_M(t_0 + k\Delta t) \cdot F_0(t_0 + k\Delta t) \quad (s = 0) \\ P_s(t_0 + k\Delta t) = \sum\limits_{q=s}^{M+s} G_q(t_0 + k\Delta t) \cdot F_{M+s-q}(t_0 + k\Delta t) \quad (s = 1, 2, \cdots, N) \end{array} \right. \tag{13}$$

In this formula, when the number of failed satellites is S, the probability of SIS constellation availability is $P_s(t_0 + k\Delta t)$.

2.3. Per-satellite availability evaluation

2.3.1. Per-satellite availability evaluation of GPS

According to the Markov state transition model, it can be seen that the key to calculate satellite availability is to get satellite failure rate λ and restoration rate μ. Therefore, by analyzing the GPS status report provided by the FAA, the MTBF and MTTR of each satellite with different types of failures can be respectively obtained, and then the availability of the satellite can be obtained.

In order to guarantee the reliability of the evaluated results, this paper makes the statistics based on all outages according to the GPS failure report of FAA. According to analysis, it can be seen that a total number of 51 satellites generates different types of outages from 1999 to 2015. By processing the MTBF and MTTR of satellites, the per-satellite average failure rate and restoration rate can be obtained, which are shown in **Figure 4**.

The spacecraft number (SVN) has a certain relationship with the order of launch of GPS satellites. Satellites with smaller numbers are launched earlier and satellite models are lower; while satellites with larger numbers are launched later, and satellite models are relatively high. From the analysis of **Figure 4** in general, the average repair rate of the higher-model satellites is generally far greater than the average failure rate compared with the low-model satellites. Combined with the analysis of formula (4), it can be inferred that the availability of higher-profile satellites is generally higher, which reflects the continuous development of GPS satellites to some extent.

By bringing the average failure rate and restoration rate of each of the above satellites into the per-satellite availability model, the availability of GPS per-satellite can be obtained, as shown in **Figure 5**.

The dotted line is the per-satellite availability minimum standard (0.957) of GPS SPS PS (2008) in **Figure 5**. If the availability of the satellite is greater than this value, the satellite is considered to meet the availability criteria. As can be seen from **Figure 5**, except for the availability of

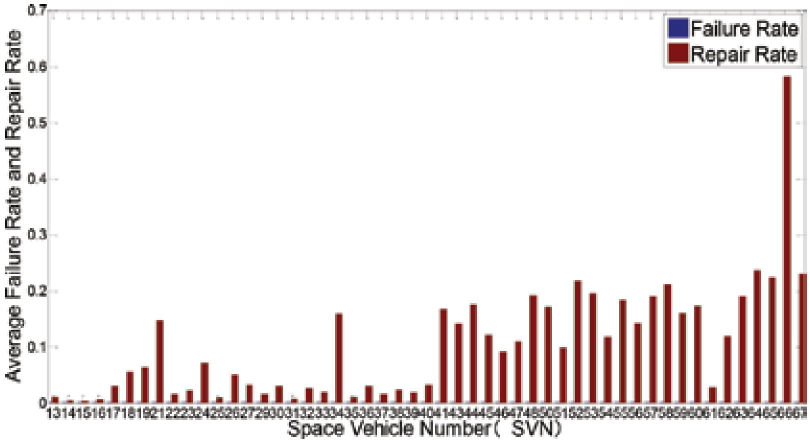

Figure 4. Average failure rate and restoration rate of GPS satellites.

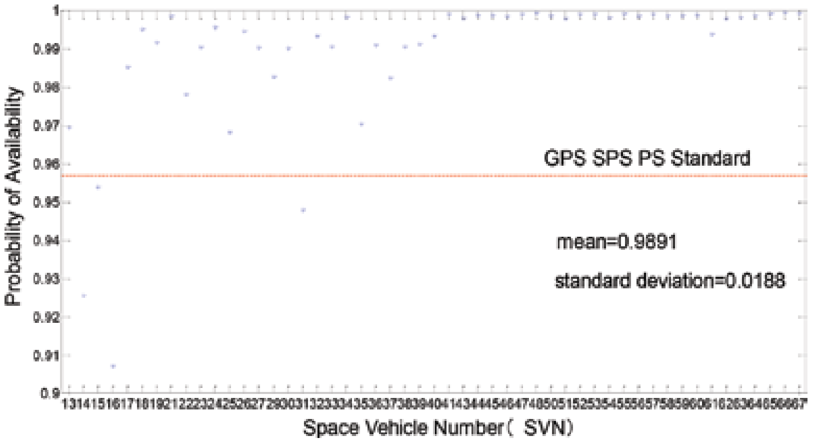

Figure 5. Distribution of GPS per-satellite availability.

retired SVN14, 15, 16 and 31 satellites, the availability of the remaining satellites is greater than 0.957, which satisfies the availability criteria of GPS SPS PS (2008), and basically verifies the above GPS. The correctness and effectiveness of the single-star usability assessment model. It can also be seen from **Figure 5** that the average availability of GPS satellites can reach 0.9891, and it is calculated that as of 2015, the average availability of all GPS satellites in orbit is 0.9985, far exceeding 0.957.

In addition, the section compares the availability of satellites according to the type of satellite, as shown in **Figure 6**.

As can be seen from **Figure 6**, the average availability of the BLOCK II series satellites is the lowest, and the average availability of the BLOCK IIF series satellites is the highest. With the continuous upgrading of satellite models, the availability of GPS satellites is significantly

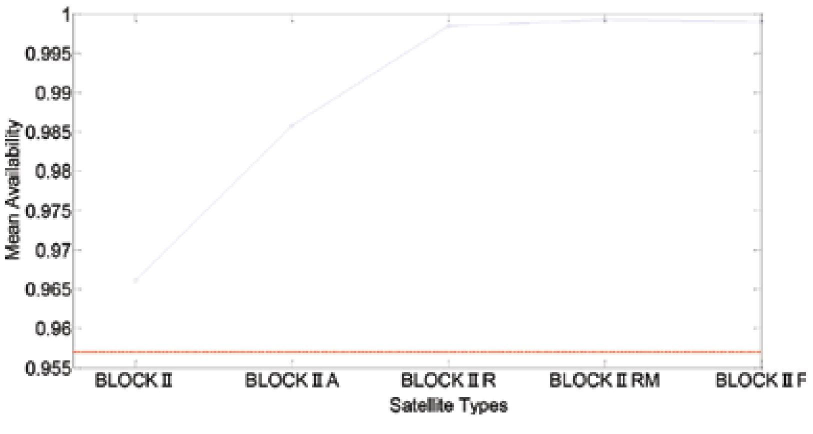

Figure 6. Availability of different satellite types.

enhanced. With the continuous advancement of GPS modernization, the availability of GPS satellites is constantly improving.

2.3.2. Per-satellite availability evaluation of BDS

BDS has not yet established a sound outage forecasting mechanism. Therefore, there is no FAA-like department in China to provide a measured fault report on BDS. Therefore, the paper mainly obtains the Beidou navigation message published by IGS, and extracts its "health word" data as the data source according to the Beidou satellite navigation system spatial signal interface control file (2.1) [29–31]. The average failure rate and average repair rate of the satellites obtained by collating the data sources are shown in **Figure 7**.

Since December 24, 2013, the C13 satellite is in the unhealthy state, and its restoration rate is zero. Comparing **Figure 4** and **Figure 7**, it can be found that the average restoration rate of BDS satellites is generally higher than that of GPS, indicating that the BDS satellite system can repair the satellites more timely when the satellites fail. However, the average failure rate of BDS satellites is also significantly higher than that of GPS, indicating that the frequency of BDS failures is greater.

Bringing the average failure rate and average restoration rate of the BDS into the per-satellite availability model, you can get the single-star availability probability of the BDS, as shown in **Figure 8**.

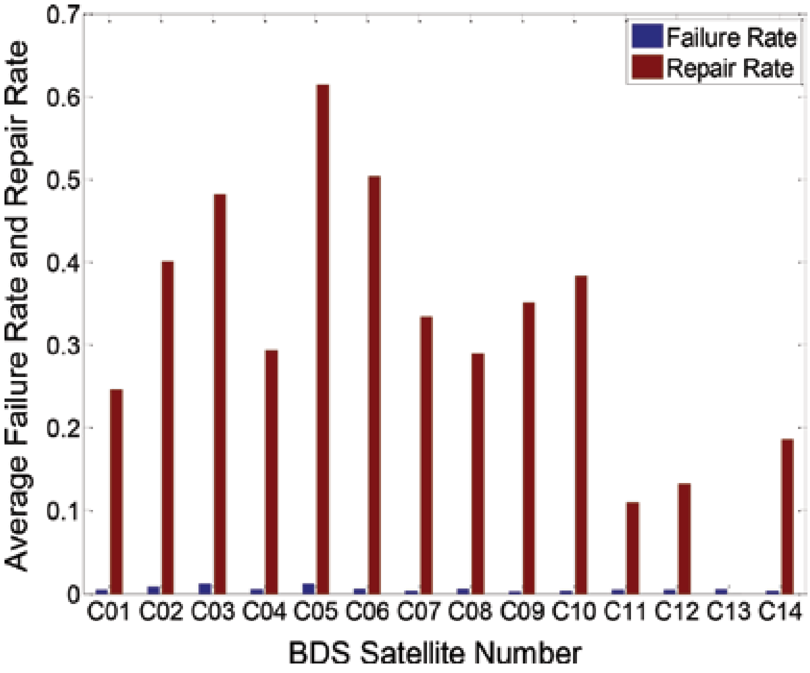

Figure 7. Average failure rate and restoration rate of BDS satellites.

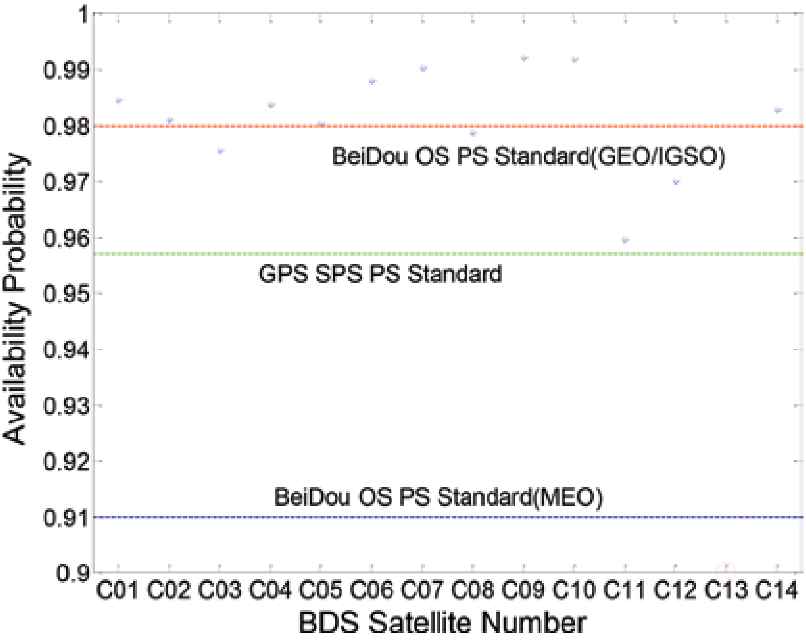

Figure 8. Distribution of BDS per-satellite availability.

In **Figure 8**, since the restoration rate of the C13(MEO) satellite is zero, the satellite's per-satellite availability is 0 (indicated by a circle). As can be seen from **Figure 8**, except for the C13 satellite, the availability of other MEO satellites is in line with the minimum availability standard of 0.91 for MEO satellites in BDS-OS-PS-1.0. In addition to the poor SIS availability of C03(GEO) and C08(IGSO) satellites due to factors such as switching satellites and system instability, the remaining GEO and IGSO satellites meet their respective minimum availability standards of 0.98.

2.4. Constellation availability evaluation

2.4.1. Constellation availability evaluation of GPS SIS

As of 2015, the number of remaining in-orbit satellites was 27 except for satellites that were unable to count MTBF and MTTR values just after launch. The 27 satellites in orbit are distributed over six orbital planes, as shown in **Table 2**.

In order to keep the status that four baseline slot satellites located on the same orbital plane, the satellites of SVN23, SVN46, SVN67 were selected as non-orbital satellites according to the satellite distribution principle, and the remaining 24 satellites are based on the orbital position, that is, the constellation consists of 24 + 3 satellites.

Through the analysis of per-slot availability, the average failure rate of the 24 baseline constellation is 1.6551e−04, and the average restoration rate is 0.1796. Similarly, the average failure rate of the 3 spare satellites is 1.4881e−04, and the average restoration rate of the 3 spare

Slot	A2	A4	A5	A6	B1	B2	B3	B4	C1
SVN	52	48	65	64	56	62	44	58	57
Slot	C2	C3	C4	D1	D2	D3	D4	D5	D6
SVN	66	59	53	61	63	45	34	46	67
Slot	E1	E2	E3	E4	E5	F1	F2	F3	F4
SVN	51	47	50	54	23	41	55	43	60

Table 2. Distribution of the satellites.

satellites is 0.1144. Then both the state transition matrix $\vec{G}\ (\Delta t)$ of baseline constellation and the state transition matrix $\vec{\mathrm{F}}\ (\Delta t)$ of spare satellites constellation can be calculated. Assuming the time interval of state transition is 1 h, then as long as the initial state $\vec{G}\ (t_0)$ of baseline constellation and the initial state $\vec{\mathrm{F}}\ (t_0)$ of spare satellites constellation can be determined, the SIS constellation availability of navigation system can be calculated according to the formulas (11)–(13).

The initial state $\vec{G}\ (t_0)$ and $\vec{\mathrm{F}}\ (t_0)$ can be divided into two cases:

1. Regardless of the per-slot availability in initial state.

Regardless of the per-slot availability means that there is no failed baseline constellation and spare satellites at the beginning time. Therefore, it can be attained as follows.

$$\vec{G}(t_0) = [1 \quad 0 \quad 0 \quad \cdots \quad 0]^T$$

$$\vec{F}(t_0) = [1 \quad 0 \quad 0 \quad 0]^T$$

Through the experiment, the constellation availability has been in stable state under the condition of $T = 300\Delta t$. Then the constellation availability probability of SIS on different failure conditions is listed in **Table 3**.

2. Considering the per-slot availability in initial state.

The initial state of baseline constellation and spare satellites constellation will be changed after considering the per-slot availability. In order to simplify the calculation process, the average per-slot availability probabilities of 24 baseline constellation and 3 spare satellites are calculated, respectively. And the calculation is in terms of the per-slot availability probability showed in **Figure 7**. Therefore, p_0 is the average per-slot availability probability of 24 baseline

P_0	P_1	P_2	P_3	P_4	…
0.999999963	3.6599e−08	3.0692e−10	2.4458e−12	1.9073e−14	…

Table 3. SIS constellation availability (regardless of the per-slot availability in initial state).

P_0	P_1	P_2	P_3	P_4	…
0.999999963	3.6599e−08	3.0692e−10	2.4458e−12	1.9073e−14	…

Table 4. SIS constellation availability (considering the per-slot availability in initial state).

constellation, its value is 0.9988. And p_1 is the average per-slot availability probability of 3 spare satellites, its value is 0.9963. Then, it can be calculated as follows:

$$\vec{G}(t_0) = \left[(p_0)^{24} \quad C_{24}^{1}(1-p_0)(p_0)^{23} C_{24}^{2}(1-p_0)^{2}(p_0)^{22} \cdots (1-p_0)^{24} \right]^{T}$$
$$= [0.9713 \quad 0.02830.00043.5036\text{e-}06 \cdots 9.882\text{e-}71]^{T}$$

$$\vec{F}(t_0) = \left[(p_1)^{3} \quad C_{3}^{1}(1-p_1)(p_1)^{2} \quad C_{3}^{2}(1-p_1)^{2} p_1 \quad (1-p_1)^{3} \right]^{T}$$
$$= [0.9889 \quad 0.0110 \quad 4.1056\text{e-}05 \quad 5.0911\text{e-}08]^{T}$$

By the experiment, the constellation availability probability of SIS under the condition of considering the per-slot availability in initial state is listed in **Table 4**.

Analyzing the above two cases, it can be concluded that:

1. On the condition of considering the per-slot availability in initial state, since the on-orbit satellites all have a large per-slot availability probability, $G_0(t_0)$ and $F_0(t_0)$ are basically close to 1. In other words, whether considering per-slot availability in initial state have little influence on the element values of initial state matrix. When $T = k\Delta t$ is large enough, the constellation availability reaches stable state. Then, the tiny gaps between the initial state matrix of the above two cases have no effect on the system availability. So, when per-slot availability is large enough, whether or not to consider per-slot availability in initial state has no effect on SIS constellation availability.
2. **Tables 2–4** show that when there are no failed satellites in satellite constellation, the constellation availability probability can reach 0.999999963. It is basically close to 1. By contrast, the probability of other failure states can be neglected. Thus, it can be seen that the constellation, which is made up of the 27 satellites has a very high availability.

2.4.2. Constellation availability evaluation of BDS SIS

The spatial constellation of the BDS consists of 35 satellites. At present, BDS is in the construction stage of global satellite navigation system. As of the end of 2015, there are only 20 BDS satellites launched, which is not enough to form a complete constellation. Moreover, due to the small number of satellites, the BDS does not currently have a backup satellite dedicated to replacing faulty satellites. Therefore, the constellation availability model of GPS SIS is not suitable for the current BDS system.

In addition, due to the incomplete BDS constellation, only BDS SIS availability in BDS-OS-PS-1.0 and BDS-SIS-ICD-2.1 is indicated by per-satellite availability, and there is no definition of BDS SIS constellation availability and related indicators [22].

Based on the above reasons, the constellation usability should be evaluated after the Beidou global satellite navigation system constellation is fully completed and the corresponding evaluation indicators are perfected. At present, the practical significance of analyzing the availability of BDS SIS constellation is not significant.

3. Conclusions

This chapter mainly studies the per-satellite availability and constellation availability evaluation methods of GPS and BDS SIS, including the establishment of evaluation models and performance verification based on measured data.

The first part of this chapter establishes a single-star usability evaluation model based on Markov process from the reliability principle, and proposes a constellation usability evaluation model that considers the satellite's failure rate, repair rate and backup situation. On this basis, the second part of this chapter combines the measured data from the 1999–2015 GPS quarterly performance report released by the FAA and the BDS navigation message issued by IGS to obtain the single-star availability and constellation usability evaluation results of GPS and BDS. The results show that, except for the retired SVN14, SVN15, SVN16 and SVN31 GPS satellites, the availability of the remaining GPS satellites meets the GPS SPS PS (2008) availability standard. In the absence of satellite failure, the GPS SIS layer constellation availability can reach 0.999999963. Except for the C13 BDS satellite, the other MEO satellites meet the minimum availability standard of 0.91 for MEO satellites in BDS-OS-PS-1.0. The SIS availability of the C03 (GEO) and C08 (IGSO) satellites is poor due to factors such as switching satellites and system instability, and the remaining GEO and IGSO satellites meet their corresponding minimum availability standards of 0.98.

Author details

Ershen Wang*, He He and Chaoying Jia

*Address all correspondence to: wanges_2016@126.com

Shenyang Aerospace University, Shenyang, China

References

[1] Jin SG, Luo OF, Gleason S. Characterization of diurnal cycles in ZTD from a decade of global GPS observations. Journal of Geodesy. 2009;**83**(6):537-545. DOI: 10.1007/s00190-008-0264-3

[2] Jin SG, van Dam T, Wdowinski S. Observing and understanding the earth system variations from space geodesy. Journal of Geodynamics. 2013;**72**:1-10. DOI: 10.1016/j.jog.2013.08.001

[3] Jin SG, Qian XD, Kutoglu H. Snow depth variations estimated from GPS-Reflectometry: A case study in Alaska from L2P SNR data. Remote Sensing. 2016;**8**(1):63

[4] Hou HT, Xie F, Zhang WX. Availability analysis for constellation of GNSS based on Markov process. Systems Engineering & Electronics. 2014;**36**(4):685-690

[5] Zhao JX, Chen JP, Hu CB, Wang DX, Zhang ZX, Liu CX, et al. Method of navigation message broadcast performance analysis for GNSS. In: China Satellite Navigation Conference (CSNC) 2016 Proceedings. Lecture Notes in Electrical Engineering. Vol. 389. Springer; 2016. pp. 93-106

[6] Steffen T, Stefan E, Johann F, Michael M. First signal in space analysis of GLONASS K-1. In: The 24th International Technical Meeting of the Satellite Division of the Institute of Navigation. Portland, OR; 2011. pp. 3076-3082

[7] Jin SG, Feng GP, Gleason S. Remote sensing using GNSS signals: Current status and future directions. Advances in Space Research. 2011;**47**(10):1645-1653

[8] Jin SG, Jin R, Li D. Assessment of BeiDou differential code bias variations from multi-GNSS network observations. Annales Geophysicae. 2016b;**34**(2):259-269

[9] Zhao GY, Sun YF. The availability parameters system of satellite navigation system. In: 2014 Annual Reliability and Maintainability Symposium (RAMS). 2014. pp. 1-6

[10] U.S. Department of Defense. Global Positioning System Standard Positioning Service Signal Specification. United States; 1993

[11] U.S. Department of Defense. Global Positioning System Standard Positioning Service Signal Specification. United States; 1995

[12] U.S. Department of Defense. Global Positioning System Standard Positioning Service Performance Standard. United States; 2001

[13] U.S. Department of Defense. Global Positioning System Standard Positioning Service Performance Standard. United States; 2008

[14] Federal Aviation Administration, 2015. Global Positioning System (GPS) Standard Positioning Service (SPS) Performance Analysis Report #90

[15] John A, Joseph S. Development of new GPS performance standards. In: The Proceedings of the 24th International Technical Meeting of the ION Satellite. Salt Lake City, UT; 2011. pp. 26-33

[16] Walter T, Blanch J, Enge P. Evaluation of signal in space error bounds to support aviation integrity. Navigation. 2010;**11**(26):11-21

[17] Sun S, Wang ZP. Signal-in-space accuracy research of GPS/BDS in China region. In: China Satellite Navigation Conference(CSNC) 2016 Proceedings. Lecture Notes in Electrical Engineering. Vol. 389. Springer; 2016. pp. 235-245

[18] Ochieng WY, Sheridan KF, Sauer K, Han X. An assessment of the RAIM performance of a combined Galileo/GPS navigation system using the marginally detectable errors (MDE) algorithm. GPS Solution. 2001;**5**(3):42-51

[19] Li Z. Research on monitoring and assessment of satellite navigation system performance. PLA Information Engineering University; 2012 (in Chinese)

[20] China Satellite Navigation Office. BeiDou Navigation Satellite System Open Service Performance Standard (Version 1.0). 2013 (in Chinese)

[21] Wang E, Zhang Q, Tong G, et al. Monitoring and evaluation algorithm of GNSS signal in space availability. Advances in Space Research. 2016;**59**(3):786-793

[22] Wang ES, Hu ZM, Qu PP, et al. Evaluation algorithm based on Markov process for GPS per-slot and constellation availability. Journal of Aeronautics Astronautics & Aviation. 2017;**49**(2):139-148

[23] Zhou SS, Jiao J, Sun Q. The modeling and simulation of constellation availability based on satellite reliability. Applied Mechanics and Materials. 2014;**522**(524):1215-1219

[24] Wang ES, Zhang Q, Tong G, et al. Monitoring and evaluation algorithm of GNSS signal in space availability. Advances in Space Research. 2017;**59**(3):786-793

[25] Cao JH, Cheng K. An Introduction to Mathematics of Reliability. BeiJing: Higher Education Press; 2006. pp. 182-222

[26] Malefaki S, Limnios N, Dersin P. Reliability of maintained systems under a semi-Markov setting. Reliability Engineering and System Safety. 2014;**131**(3):282-290

[27] Clifford WK. GPS constellation state probabilities, Historical & Projected. In: The Proceedings of ION NTM-1999. San Diego, CA; 1999. pp. 265-270

[28] Zheng H, Ren LM. Availability analysis of satellite constellation. In: The 8th International Conference on Reliability, Maintainability and Safety, ICRMS 2009. 2009. pp. 245-248

[29] China Satellite Navigation Office. Development of BeiDou navigation satellite system. In: The 7th Meeting of International Committee on GNSS. Beijing, China; 2012

[30] China Satellite Navigation Office, 2013. BeiDou Navigation Satellite System Signal In Space Interface Control Document Open Service Signal (Version 2.0).

[31] Montenbruck O, Hauschild A, Steigenberger P, Hugentobler U, Teunissen P. Initial assessment of the COMPASS/BeiDou-2 regional navigation satellite system. GPS Solution. 2013; **17**(2):211-222

Section 3

Accuracy of GNSS Positioning Under Severe Environmental Conditions

Chapter 3

Robust GNSS Positioning in Urban Environment

Enik Shytermeja

Additional information is available at the end of the chapter

http://dx.doi.org/10.5772/intechopen.80412

Abstract

In the past years, global navigation satellite systems (GNSS) have gained the core position concerning the geolocalization applications and services in urban environments. The major issue of the GNSS-based urban application expansion is related to the positioning service quality assurance, expressed in terms of accuracy, integrity, availability, and continuity of the localization service. The dense urban environments, such as city centers, are challenging to the GNSS signal reception causing the frequent blockage of the line-of-sight (LOS) signals and the multipath phenomenon, referred to as the reception of the diffracted/reflected echoes of the transmitted signal. These effects severely affect the pseudorange and Doppler measurements, used by a GNSS receiver for the user's position computation, which will further induce the computation of an erroneous positioning solution by the navigation processor down to a positioning loss in the presence of limited satellite visibility and few provided measurements. Therefore, advanced signal processing techniques do represent viable solutions aiming at the mitigation of these undesired effects in order to foster the accuracy and availability of the localization solution. This chapter will address in details the GNSS vector tracking (VT) receiver's configuration able to cope with the urban environment-induced effects.

Keywords: GNSS, extended Kalman filter, vector tracking, multipath, NLOS, correlators

1. Introduction

Global navigation satellite systems (GNSS) are increasingly present in our life and represent a key player in the world economy mostly due to the expansion of location-based services. An important part of the GNSS applications is found for the automotive usage in urban environments that are characterized by difficult signal reception conditions. These services do exhibit by very stringent quality of service demands. In these harsh environments, the received signals are severely affected by the urban obstacles including buildings, road infrastructure, and foliage generating strong signals' fading and fast phase oscillations. Consequently, the generated pseudo-range and Doppler measurements are degraded. In the worst-case scenario, the direct signal can be totally blocked by the urban obstacles generating the GNSS signal blockage phenomena that introduce large biases on the pseudo-range measurements and cycle slips for the carrier phase observations.

Standard GNSS receivers, which track each satellite independently through the technique referred to as scalar tracking, fail to cope with these harsh urban conditions. Therefore, this work is particularly focused on the proposal and detailed design of the dual-constellation single-frequency vector tracking architecture for the automotive usage in urban environment. This architecture can improve the tracking of some attenuated or blocked signals due to the channel-aiding property based on the navigation solution estimation and thus assure a robust navigation solution estimation.

2. GNSS receiver structure

This section aims at providing a detailed description of the GNSS receiver structure with an emphasis on the GNSS signal processing stage from the GNSS signal reception up to the measurement generation process.

2.1. GNSS digital signal processing

The digital signal processing is the consecutive stage of the analog front end, taking as input of the sampled and discretized received signals from each satellite in view. Herein, the digitized signal is fed to multiple channel processing blocks, corresponding to each received satellite signal. The digital signal processing blocks conduct three main operations, the correlation, the acquisition, and the code/carrier tracking [1]. The scalar tracking process is achieved in a channelized structure for all the satellites in view. The objective of the tracking process is to refine the coarse estimations of the code delay and Doppler frequency provided by the acquisition block and to precisely follow the signal properties changing over time [2]. The GNSS scalar tracking architecture is illustrated in **Figure 1**.

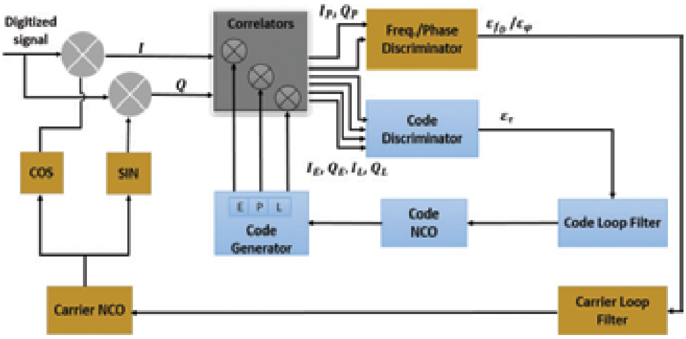

Figure 1. The conventional GNSS tracking architecture.

The scalar tracking process, employed for each tracked satellite, comprised the following main modules:

- *Code tracking*: in charge of estimating the code delay offset (ε_τ) between the incoming signal's code and the locally generated replica based on the closed feedback loop referred to as the delay lock loop (DLL). In this process, at least three delayed code replicas, known as the early, prompt, and late replica, are generated according to the correlation process with the incoming signal.
- *Carrier tracking*: responsible of estimating the residual Doppler shift $\left(\varepsilon_{f_D}\right)$ and the carrier phase offset $\left(\varepsilon_\varphi\right)$. The carrier tracking module that provides the estimation of the Doppler shift $\left(\varepsilon_{f_D}\right)$ is called as frequency lock loop (FLL), while the carrier phase error $\left(\varepsilon_\varphi\right)$ compensation is conducted by the phase lock loops (PLL) [2]. It is important to highlight the fact that for certain applications with important user's dynamics, an FLL-aided PLL may be also employed.

The scalar tracking architecture, whose high-level representation is provided in **Figure 1**, includes the following main processing blocks:

- *Correlators*: accumulating the combination of the sampled signal with the code and carrier replicas through mixing the in-phase and quadrature signal branches with the three delayed (early, prompt, and late) code-spreading sequences from the GNSS code generator block
- *Code/carrier discriminators*: in charge of estimating the code delay and carrier frequency/ phase errors based on the three correlator output pairs
- *Low-pass filters*: filtering the discriminators' outputs for noise reduction at the entry of the code/carrier local oscillators
- *Numerical control oscillator (NCO)*: operating in a feedback loop manner and providing the required correction to the code and carrier generators based on the filtered discriminator output, which is further used to generate the local replicas for the successive measurement epoch

The association of the low-pass filters and the NCOs provides the equivalent loop filter, whose response to the user's dynamics is strictly related to two parameters such as the filter's loop order and the equivalent noise bandwidth. In details, a higher noise bandwidth implies faster loop response time (and thus better response to high user's dynamics) but with the drawback of dealing with noisier results due to the shorter integration time. Considering the filter's loop order, the higher the loop filter, the better the filter capability to follow the high-order user's dynamics is [3]. Keen readers may find detailed description of the loop filters in [3–5].

The scalar tracking is continuously run for each satellite-user channel in order to precisely estimate the code delay and carrier frequency/phase evolution in time [2]. In the GNSS receiver, the code delay and carrier frequency/phase lock loops are jointly used.

2.1.1. GNSS code delay tracking

The code delay tracking process is directly performed after the acquisition stage, responsible among other tasks of the detection of the incoming signal. The code delay tracking process assures the alignment between the incoming signal's code and the local replica's code by refining the code delay error measurement from the discriminator block that further steers the code NCO [5]. The code tracking is performed by means of a DLL that is a feedback loop capable of steering the local PRN code delay based on the estimation of the code delay error ε_τ [6]. This code delay error measurement is later used to compute the pseudo-range observation.

The correlation between each local replica with the in-phase and quadrature signal samples generates one correlator pair. Finally, three correlator pairs are obtained at the end of this operation, expressed by

$$\begin{aligned}
IE_k &= \frac{A}{2}\cdot d_k\cdot R_c\left(\varepsilon_{\tau,k}+\frac{k_c\cdot T_c}{2}\right)\cdot cos\left(\varepsilon_{\varphi,k}\right)\cdot sinc\left(\pi\cdot\varepsilon_{f_{D,k}}\cdot t\right)+n_{IE,k}\\
IP_k &= \frac{A}{2}\cdot d_k\cdot R_c(\varepsilon_{\tau,k})\cdot cos\left(\varepsilon_{\varphi,k}\right)\cdot sinc\left(\pi\cdot\varepsilon_{f_{D,k}}\cdot t\right)+n_{IP,k}\\
IL_k &= \frac{A}{2}\cdot d_k\cdot R_c\left(\varepsilon_{\tau,k}-\frac{k_c\cdot T_c}{2}\right)\cdot cos\left(\varepsilon_{\varphi,k}\right)\cdot sinc\left(\pi\cdot\varepsilon_{f_{D,k}}\cdot t\right)+n_{IL,k}\\
QE_k &= \frac{A}{2}\cdot d_k\cdot R_c\left(\varepsilon_{\tau,k}+\frac{k_c\cdot T_c}{2}\right)\cdot sin\left(\varepsilon_{\varphi,k}\right)\cdot sinc\left(\pi\cdot\varepsilon_{f_{D,k}}\cdot t\right)+n_{QE,k}\\
QP_k &= \frac{A}{2}\cdot d_k\cdot R_c(\varepsilon_{\tau,k})\cdot sin\left(\varepsilon_{\varphi,k}\right)\cdot sinc\left(\pi\cdot\varepsilon_{f_{D,k}}\cdot t\right)+n_{QP,k}\\
QL_k &= \frac{A}{2}\cdot d_k\cdot R_c\left(\varepsilon_{\tau,k}-\frac{k_c\cdot T_c}{2}\right)\cdot sin\left(\varepsilon_{\varphi,k}\right)\cdot sinc\left(\pi\cdot\varepsilon_{f_{D,k}}\cdot t\right)+n_{QL,k}
\end{aligned} \tag{1}$$

where

- The triplet $\left(\varepsilon_{\tau,k},\varepsilon_{\varphi,k},\varepsilon_{f_{D,k}}\right)$ represents the code delay, carrier phase, and frequency estimation errors at the current epoch k.
- $k_c\cdot T_c$ refers to the early-late code chip spacing with k_c and T_c representing the fraction of chip spacing and the code chip period, respectively.
- n_{xy} denotes the noise term at the correlator output (where x stands for the in-phase (I) or quadrature (Q) and y for the early (E), prompt (P), or late (L) code delays), which is correlated and Gaussian distributed with zero mean and variance $\sigma^2_{n_{xy}}$.

The most common discriminators employed in GNSS receivers are the noncoherent early-minus-late power (EMLP) and the dot product (DP) discriminators due to their tracking robustness since insensitive toward the carrier phase information. These two discriminators are defined by

$$\begin{aligned}
D_{EMLP}(\varepsilon_{\tau,k}) &= \left(IE_k^2+QE_k^2\right)-\left(IL_k^2+QL_k^2\right)\\
D_{DP}(\varepsilon_{\tau,k}) &= (IE_K-IL_K)\cdot IP_k+(QE_K-QL_K)\cdot QP_k
\end{aligned} \tag{2}$$

The chip spacing is a crucial parameter for the discriminator function and thus must be selected so that the early and late correlator outputs are always evaluated at the correlation function main peak. Therefore, the EMLP and DP discriminators require a correlator spacing set less than 1 chip and 0.5 chip for the GPS L1 binary phase-shift keying (BPSK) and Galileo binary offset carrier (BOC) signals, respectively [3]. In order to remove the amplitude sensitivity of the code discriminators, normalization factors shall be applied to have a direct access to the code tracking error according to [7, 8].

2.1.2. GNSS carrier phase tracking

The carrier phase tracking is achieved by the phase lock loop (PLL) that is responsible of keeping the carrier phase alignment between the incoming signal and the locally generated replica. The main goals of the phase tracking loop are:

- The computation of a phase reference for the detection of the GNSS modulated data signal
- The provision of precise Doppler measurements by using the phase rate information

To fulfill these objectives, the PLL uses a carrier phase discriminator to estimate the resultant phase estimation error $\left(\varepsilon_{\varphi}(k)\right)$ between the incoming signal phase and the replica phase, according to the in-phase and quadrature prompt correlator output pairs (IP, QP). Afterward, the PLL filter filters out the noise, and afterward, the carrier NCO transforms the estimated phase error into a frequency offset that modifies the NCO nominal frequency for the successive epoch [6].

The main phase discriminators used for the data channels are the following [4]:

- Dot product (DP) or the generic Costas discriminator

$$D_{DP}\left(\varepsilon_{\varphi,k}\right) = QP_k \cdot IP_k \tag{3}$$

- The extended arctangent (Atan2) phase discriminator [9]

$$D_{Atan2}\left(\varepsilon_{\varphi,k}\right) = \mathrm{atan2}\left(\frac{QP_k}{IP_k}\right) \tag{4}$$

3. Vector tracking architecture

3.1. Urban environment-induced effects

The urban environment causes important threats to the GNSS signal reception and its posteriori processing, severely deteriorating the navigation solution accuracy and availability. The problems of the urban environment in the navigation domain can be summarized as follows:

- *Multipath*: denoted as the joint reception of both the direct LOS signal and the reflected or diffracted GNSS LOS echoes from the urban obstacles
- *Attenuation or blockage of the GNSS LOS signal*: arising due to the partial or total obstruction of the GNSS LOS from the urban environment characteristics

- *Interference:* resulting from the presence of wide signal sources transmitting in the adjacent GNSS frequency bands

The resulting consequences of these urban environment error sources from the GNSS receiver's point of view are the following [10]:

- *Distortion of the correlation function*: computed between the received multipath-contaminated signal and the NCO-generated replica. The tracking of the multipath-affected signals leads to a deterioration of code delay and carrier frequency/phase estimation accuracy down to the loss of lock of the tracking loops. As a result, the estimated pseudo-ranges and pseudo-range rate measurements from the code and carrier tracking loops, respectively, which are fed to the navigation filter are significantly corrupted.
- *Only non-LOS (NLOS) signal reception*: resulting from the total obstruction of the direct LOS GNSS signals and thus inducing large biases on the pseudo-range and Doppler measurements if only NLOS signals are tracked.

Finally, the resulting degraded measurements cause the navigation processor to calculate an inaccurate position solution or even to be unable to compute one in the case of few available measurements.

3.2. Vector tracking motivation

Vector tracking algorithms represent advanced GNSS signal processing methods, having the ability to function at lower carrier-to-noise power (C/N_0) ratios and in higher user's dynamics than traditional GNSS receivers [11]. Contrary to the conventional or scalar tracking architecture, where each visible satellite channel is being independently tracked, vector tracking performs a joint signal tracking of all the available satellites. It exploits the knowledge of the estimated receiver's position and velocity to control the tracking loops' feedback [6]. The comparison between the scalar tracking and vector tracking architectures is illustrated in **Figure 2**.

Concerning the vector tracking architecture, depicted in **Figure 2(b)**, the code and carrier tracking loops of all the visible satellites are connected via the navigation solution computed by the navigation filter. The individual code/carrier loop filters and NCOs, illustrated by the dashed red line in the left figure, are abolished and substituted by the vectorized code/carrier update block depicted in blue.

3.3. Proposed vectorized GNSS receiver architecture

Aiming at a robust GNSS signal tracking and navigation technique in urban environment, a dual-constellation GPS + Galileo single-frequency L1/E1 vector delay/frequency-locked loop (VDFLL) architecture is proposed and implemented for the automotive usage, whose architecture is illustrated in **Figure 3**.

In fact, the use of dual-constellation measurements significantly improves the availability of a navigation solution in urban canyons. Moreover, the implementation of the VDFLL tracking architecture, where the navigation filter is responsible of estimating both the code delay and the Doppler frequency change of each received signal, enhances the vehicle dynamic tracking capability of the GNSS receiver [6]. As it can be clearly observed in **Figure 3**, the central navigation filter accepts the code $\left(\varepsilon_{\tau}^{(i)}\right)$ and carrier $\left(\varepsilon_{f_D}^{(i)}\right)$ discriminator outputs for each GPS $(i = 1 \div N1)$ and Galileo $(i = 1 \div N2)$ tracked channel as its input vector. Furthermore, the code and carrier NCO update process is achieved by projecting the predicted navigation solution into the pseudo-range and pseudo-range rate domains.

The VDFLL navigation block employs a Kalman filter (KF) that is a Bayesian estimation technique, which incorporates the measurements from the past epochs to obtain a more accurate navigation solution. In this work, the selection criteria of the extended Kalman filter

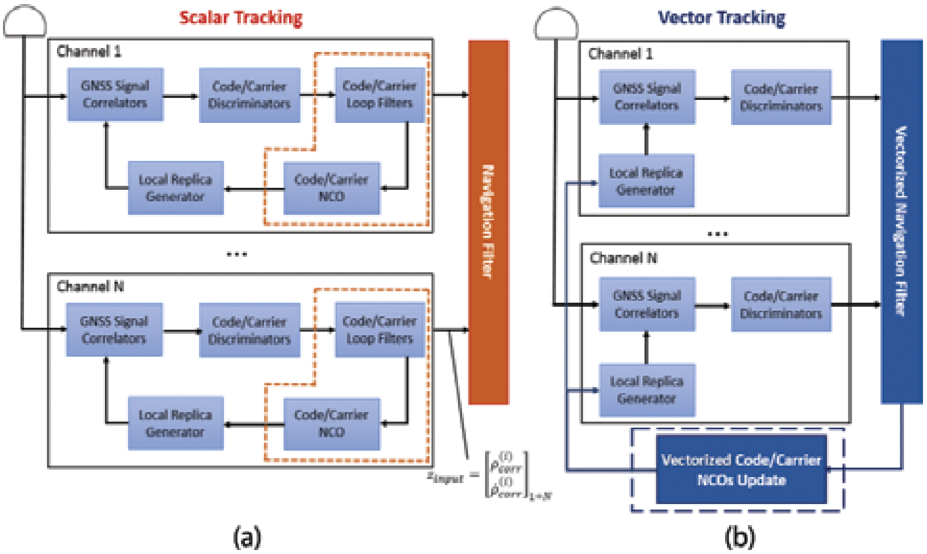

Figure 2. The high-level comparison of (a) conventional or scalar tracking and (b) vector tracking architectures.

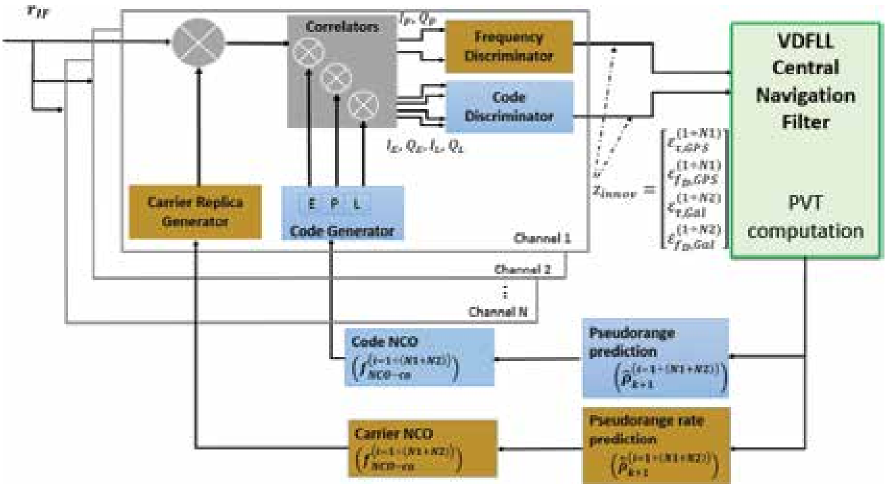

Figure 3. The noncoherent L1/E1 VDFLL architecture.

(EKF) algorithm are related to its capability to resolve the nonlinearity issues for the GNSS navigation system.

The EKF estimation process is composed of two main stages:

- *State prediction*: performing the time propagation between two consecutive epochs $(k-1)$ to the current one k of the state vector $X_{k|k-1}$ and its covariance matrix $P_{k|k-1}$
- *Measurement correction*: refining the a priori state vector and covariance matrix estimations $\left(X_{k|k-1}, P_{k|k-1}\right)$ by feeding the current epoch measurements $\left(z_{input}\right)$ into the filter and thus obtaining the improved *a posteriori* estimates $\left(X_{k|k}, P_{k|k}\right)$

3.3.1. VDFLL EKF state space description

The continuous-time EKF state model is given by

$$\frac{d}{dt}X(t) = F(t)\cdot X(t) + B(t)\cdot w(t)$$

$$\frac{d}{dt}\begin{bmatrix} x \\ \dot{x} \\ y \\ \dot{y} \\ z \\ \dot{z} \\ b_{Rx} \\ \dot{b}_{Rx} \end{bmatrix}_{8\times1} = \begin{bmatrix} A_{2\times2} & 0_{2\times2} & 0_{2\times2} & 0_{2\times2} \\ 0_{2\times2} & A_{2\times2} & 0_{2\times2} & 0_{2\times2} \\ 0_{2\times2} & 0_{2\times2} & A_{2\times2} & 0_{2\times2} \\ 0_{2\times2} & 0_{2\times2} & 0_{2\times2} & A_{2\times2} \end{bmatrix} \cdot \begin{bmatrix} x \\ \dot{x} \\ y \\ \dot{y} \\ z \\ \dot{z} \\ b_{Rx} \\ \dot{b}_{Rx} \end{bmatrix}_{8\times1} + \begin{bmatrix} 0 & 0 & 0 & 0 & 0 \\ 1 & 0 & 0 & 0 & 0 \\ 0 & 0 & 0 & 0 & 0 \\ 0 & 1 & 0 & 0 & 0 \\ 0 & 0 & 0 & 0 & 0 \\ 0 & 0 & 1 & 0 & 0 \\ 0 & 0 & 0 & 1 & 0 \\ 0 & 0 & 0 & 0 & 1 \end{bmatrix}_{8\times5} \cdot \left[w_{\dot{x}}\ w_{\dot{y}} w_{\dot{z}} w_b w_d \right] \tag{5}$$

where

- X is the state vector with the following entries to be estimated such as the user's position $[x\ y\ z]$, velocity $[\dot{x}\dot{y}\dot{z}]$, and user's clock bias and drift terms $\left[b_{Rx}\dot{b}_{Rx}\right]$ expressed in unit of $[m]$ and $\left[\frac{m}{s}\right]$, respectively.
- F denotes the state transition matrix characterizing the user's motion and clock dynamics.
- B represents the colored noise transition matrix.
- w is the process noise vector reflecting the user's dynamics (position and velocity) and receiver's oscillator (clock bias and drift) uncertainties affecting the system model
- $A_{2\times2} = \begin{bmatrix} 0 & 1 \\ 0 & 0 \end{bmatrix}$ represents the position/velocity and clock biases/drift state transition sub-matrices.

The main tuning factors of the process noise vector w and its associated covariance matrix Q can be summarized into two main categories according to their nature:

- *User's dynamics*: expressing the vehicle's dynamic uncertainties concerning the velocity error variance terms along the three ECEF axes $\left(\sigma^2_{\dot{x}}, \sigma^2_{\dot{y}}, \sigma^2_{\dot{y}}\right)$ that are further projected in the position domain through the state transition sub-matrix $A_{2\times2}$
- *Receiver's oscillator noise*: expressed in terms of the oscillator's phase and frequency noise spectral densities affecting the receiver's clock σ^2_b and drift σ^2_d biases

Passing to the discrete time domain, the system or dynamic model of the VDFLL navigation filter can be detailed as follows:

$$X_k = \ \Phi \cdot X_{k-1} + w_k \tag{6}$$

where X_k is the state vector forward projection from the $k-1^{th}$ to the k^{th} time epoch and Φ represents the dynamics of the user platform and clock, expressed as follows

$$\Phi = I + F \cdot \Delta T, \tag{7}$$

where $\Delta T = t_{k-1} - t_k$ is the time step between two successive epochs.

Substituting Eq. (7) into the continuous state transition matrix of Eq. (5), the final discrete state transition matrix is provided by

$$\Phi = \begin{bmatrix} A_{d,2\times2} & 0_{2\times2} & 0_{2\times2} & 0_{2\times2} \\ 0_{2\times2} & A_{d,2\times2} & 0_{2\times2} & 0_{2\times2} \\ 0_{2\times2} & 0_{2\times2} & A_{d,2\times2} & 0_{2\times2} \\ 0_{2\times2} & 0_{2\times2} & 0_{2\times2} & A_{d,2\times2} \end{bmatrix} \tag{8}$$

where $A_{d,2\times2} = \begin{bmatrix} 1 & \Delta T \\ 0 & 1 \end{bmatrix}$.

The process noise covariance matrix $Q_k = diag\left[Q_{x,k}, Q_{y,k}, Q_{z,k}, Q_{clk,k}\right]$ in the discrete domain per each entry can be expressed as

$$\begin{aligned} Q_k &= E\left[w_k \cdot w_k^T\right] \\ &= \int_{t_{k-1}}^{t_k} \Phi(t_k, \tau) \cdot Q(\tau) \cdot \Phi^T(t_k, \tau) \cdot d\tau \end{aligned} \tag{9}$$

Therefore, the process noise discretization for the position and velocity states along the three reference axes is computed as

$$\begin{aligned} Q_{x|y|z,k} &= \int_{t_{k-1}}^{t_k} A_{d,2\times2}(t_k,\tau) \cdot Q_{2\times2}(\tau) \cdot A_{d,2\times2}^T(t_k,\tau) \cdot d\tau \\ &= \int_{t_{k-1}}^{t_k} \begin{bmatrix} 1 & \Delta T \\ 0 & 1 \end{bmatrix} \cdot \begin{bmatrix} 0 & 0 \\ 0 & \sigma^2_{\dot{x}|\dot{y}|\dot{z}} \end{bmatrix} \cdot \begin{bmatrix} 1 & 0 \\ \Delta T & 1 \end{bmatrix} \cdot d\tau \\ &= \sigma^2_{\dot{x}|\dot{y}|\dot{z}} \cdot \begin{bmatrix} \Delta T^3/3 & \Delta T^2/2 \\ \Delta T^2/2 & \Delta T \end{bmatrix} \end{aligned} \tag{10}$$

where $\left(\sigma^2_{\dot{x}}, \sigma^2_{\dot{y}}, \sigma^2_{\dot{z}}\right)$ are the velocity noise error variances along the three navigation axes.

Applying the discretization process of Eq. (9) to the user's clock covariance states, the following relation is obtained:

$$\begin{aligned} Q_{clk,k} &= \int_{t_{k-1}}^{t_k} A_{d,2\times2}(t_k,\tau) \cdot Q_{clk,2\times2}(\tau) \cdot A_{d,2\times2}^T(t_k,\tau) \cdot d\tau \\ &= \int_{t_{k-1}}^{t_k} \begin{bmatrix} 1 & \Delta T \\ 0 & 1 \end{bmatrix} \cdot \begin{bmatrix} \sigma_b^2 & 0 \\ 0 & \sigma_d^2 \end{bmatrix} \cdot \begin{bmatrix} 1 & 0 \\ \Delta T & 1 \end{bmatrix} \cdot d\tau \\ &= \begin{bmatrix} \sigma_b^2 \cdot \Delta T + \sigma_d^2 \cdot \Delta T^3/3 & \sigma_d^2 \cdot \Delta T^2/2 \\ \sigma_d^2 \cdot \Delta T^2/2 & \sigma_d^2 \cdot \Delta T \end{bmatrix} \end{aligned} \tag{11}$$

The discrete receiver's clock process noise covariance matrix is modeled based on the Allan variance parameters [12].

3.3.2. VDFLL EKF observation model

The nonlinear relation between the state and measurement vector in an EKF is provided by

$$z_k = h(X_k) + v_k \tag{12}$$

where

- h is the *nonlinear* function relating the measurement z_k to the state X_k.
- v_k is *the measurement noise vector* that is modeled as a zero-mean uncorrelated Gaussian noise process and independent to the process noise w_k.

The measurement vector z_k comprises pseudo-ranges $\rho^{(i)}$ and Doppler measurements $\dot{\rho}^{(i)}$ and output from the code/carrier tracking process for the $i = 1 \div N$ GPS L1/Galileo E1 tracking channels [12]:

$$z_k = \left[\left(\rho^{(1)}\rho^{(2)} \quad \cdots\rho^{(N)}\right) \vdots \left(\dot{\rho}^{(1)}\dot{\rho}^{(2)}\cdots\dot{\rho}^{(N)}\right)(k)\right]_{2N\times 1} \tag{13}$$

The GNSS pseudo-range measurements of a given satellite i (from the GPS $(N1)$ and Galileo $(N2)$ satellites in view) at epoch k are rewritten as

$$\rho^{(i)}(k) = \begin{cases} |r_i(k) - r_u(k)| + X_k(7) + \varepsilon^{(i)}_{n,GPS}(k), & 0 < i \le N1 \\ |r_i(k) - r_u(k)| + X_k(7) + \varepsilon^{(i)}_{n,Gal}(k), & N1 < i \le N \end{cases} \tag{14}$$

where

- $|r_i(k) - r_u(k)| = \sqrt[2]{\left(x_s^{(i)}(k) - X_k(1)\right)^2 + \left(y_s^{(i)}(k) - X_k(3)\right)^2 + \left(z_s^{(i)}(k) - X_k(5)\right)^2}$ is the actual satellite-to-user Euclidian distance at the current epoch k where the triplets $\left(x_s^{(i)}, y_s^{(i)}, z_s^{(i)}\right)(k)$ and $(X_k(1), X_k(3), X_k(5))$ represent the i^{th} satellite and user's coordinates in the ECEF reference frame, respectively.
- $X_k(7)$ represents the receiver's clock bias term w.r.t the GPS time.
- $\varepsilon^{(i)}_{n,GPS/Gal}(k)$ represents the error due to the receiver's thermal noise, assumed to be white, centered Gaussian distributed.

Meanwhile, the remaining N-entries of the measurement vector z_k, constituted by the Doppler measurements from both the GPS and Galileo satellites, are related to the state vector through the observation function $\left(h_2^{(i)}\right)$ [6]:

$$\begin{aligned} h_2^{(i)}(X_k) = {} & \left(\dot{x}_s^{(i)}(k) - X_k(2)\right)\cdot a_x^{(i)}(k) + \left(\dot{y}_s^{(i)}(k) - X_k(4)\right)\cdot a_y^{(i)}(k) \\ & + \left(\dot{z}_s^{(i)}(k) - X_k(6)\right)\cdot a_z^{(i)} + X_k(8) + \dot{\varepsilon}^{(i)}_{n,GPS/Gal}(k) \end{aligned} \tag{15}$$

where

- $\left(a_x^{(i)}, a_y^{(i)}, a_z^{(i)}\right)(k)$ denotes the LOS projections along the three navigation axes.
- $X_k(8)$ is the receiver's clock drift state common for both the GPS and Galileo Doppler measurements.

- $\dot{\varepsilon}^{(i)}_{n,GPS/Gal}(k)$ denotes the receiver's thermal noise effect on the GPS and Galileo pseudo-range rate measurements.

The measurement noise vector v_k is modeled as a zero-mean uncorrelated Gaussian noise process with the measurement noise covariance matrix R_k that has the following entries in the main diagonal:

$$R_{jj} = \begin{cases} \sigma^2_{Code\_Discri,j} & for \quad j = 1 \cdots N \\ \sigma^2_{Carr-Discri,j} & for \quad j = 1 \cdots N \end{cases} \tag{16}$$

where the first entry refers to the pseudo-range error variance terms for the tracked GPS and Galileo satellites, while the second one is a common term for the pseudo-range rate error variance for all tracked satellites [12].

4. Description of the test setup

Within the scope of this research, a realistic dual-constellation dual-frequency GNSS signal emulator, capable of simulating the GNSS signal reception at the correlator output level and including the navigation module, has been developed. The developed signal emulator is a powerful tool for flexible and reliable GNSS receiver testing, for which all the processing blocks from the GNSS signals' correlation function, passing through the channels' tracking module and up to the different navigation algorithms, are all designed in a modular manner [12].

Two different GNSS receiver architectures are herein analyzed with the scope of performance comparison:

- The proposed L1/E1 VDFLL EKF architecture working at $\Delta T = 20\ ms$ integration time and thus providing 50 Hz code and carrier frequency updates
- The classic scalar tracking architecture employing a third-order loop PLL and a DLL, with an EKF positioning module for the navigation solution computation operating at the same rate as for the VDFLL EKF case (50 Hz)

4.1. Test scenario

The urban navigation test is herein performed on a car trajectory in Toulouse city center based on the collected data from the real test campaign in Toulouse urban area, by employing a NovAtel's ProPak receiver mounted on the car. The recorded trajectory of 600 s duration is presented in **Figure 4**.

The simulated signal reception conditions are that of a complete urban multipath model included to the receiver processing blocks with a maximum of 13 simultaneously tracked GPS L1 and Galileo E1 channels during the whole trajectory.

The receiver tracking parameters employed in the test scenario, defining the scalar (ST) and the vector tracking (VT) algorithms, are summarized in **Table 1**.

Figure 4. The reference car trajectory.

The navigation performance assessment of the proposed vectorized architecture with respect to the classic receiver configuration is performed in degraded signal reception conditions.

4.2. Urban multipath model

In this work, a widely used urban propagation channel model has been used to generate a representative of urban environment signal's reception conditions. This model, known as the DLR land mobile multipath channel model, was developed thanks to an extensive measurement campaign conducted by DLR in Munich urban and suburban areas in 2002. This model is

Parameters	**ST**	**VT**
L1/E1 code delay tracking		
DLL order	1st	Not used
DLL configuration	Carrier-aided DLL	Not used
GPS L1 chip spacing (k_{C-L1})(chip)	0.5	
GAL E1 chip spacing (k_{C-E1})(chip)	0.2	
Discriminator	Early-minus-late power (EMLP)	
DLL update period (s)	0.02	Position update rate
DLL noise bandwidth (B_{DLL-n}) (Hz)	1	Not used
Carrier phase/frequency tracking		
Carrier estimation	Phase	Frequency
PLL order	3	Not used
PLL update period (s)	0.02	Velocity update rate
PLL noise bandwidth (B_{PLL-n}) (Hz)	10	Not used
Discriminator type	Atan2	Cross product (CP)

Table 1. Tracking loop parameters.

a wideband propagation channel model where each LOS and multipath echo are individually considered [13].

Moreover, the DLR model is a hybrid statistic/deterministic mathematical propagation channel model. The statistical part refers to the generation of a random urban scenario from a given set of channel-defining parameters, as depicted in **Figure 5**. Afterward, the LOS and NLOS echo information, provided as the DLR model output, is fed in the tracking stage at the correlator output level per tracked satellite.

4.3. Performance comparison results

The position error comparison between the scalar tracking receiver and the VDFLL algorithm is presented in **Figure 6**, presenting the EKF estimation errors along the entire trajectory in the navigation frame expressed in the along- and cross-track coordinates, in blue the VDFLL and in red the KF with scalar tracking. Moreover, the blue- and red-dotted curves denote the (95%) or two σ covariance bounds, where σ is the estimation error standard deviation estimated by the Kalman filters for the two architectures, respectively.

The position error plots in the vehicle frame (along- and cross-track coordinates), illustrated in **Figure 6(a)** and **(b)**, demonstrate a clear superiority of the VDFLL algorithm, observed in terms of the low-position error variations along the trajectory that is an evident indicator of the VDFLL capability in coping with the multipath conditions. Larger position errors are observed for both architectures in the cross-track coordinate in **Figure 6(b)** that is related to the higher multipath-induced bias on the lateral projection. A significant position bias of approximately 30 *m* is seen for the scalar tracking receiver (in red) in the cross-track coordinate from the 70th to the 100th epoch, which coincides with strong satellite outage event and thus limited satellite

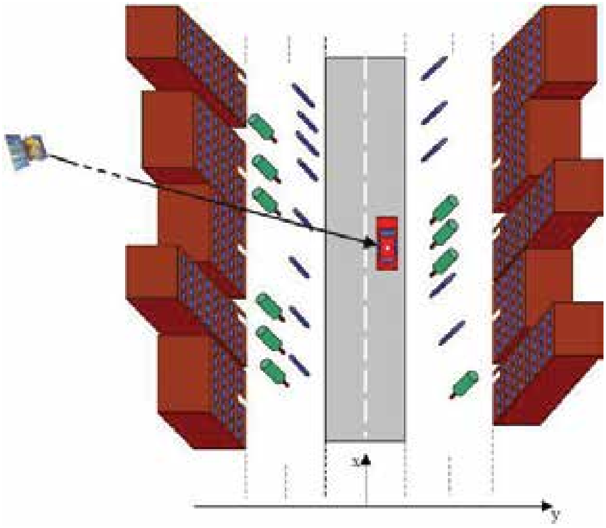

Figure 5. Artificial urban scenario generated by the DLR urban propagation channel model [13].

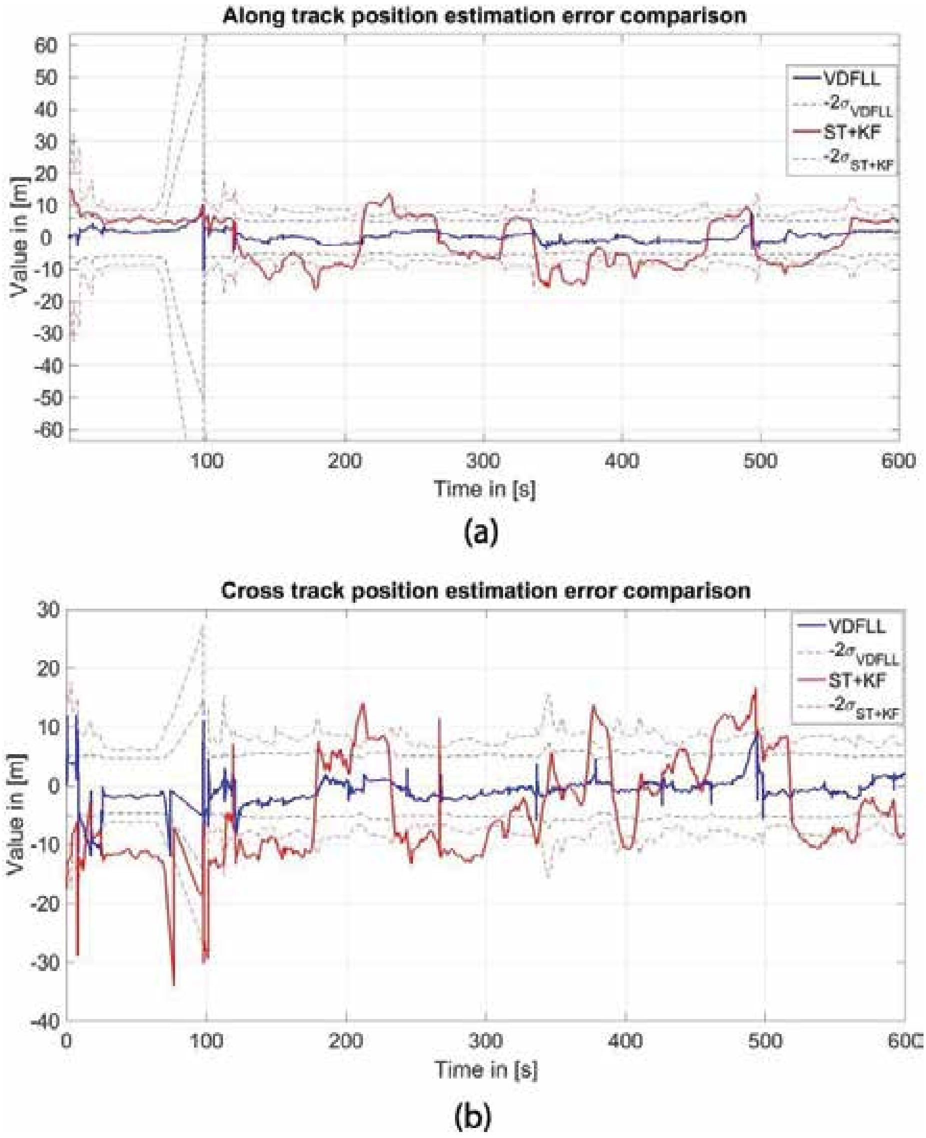

Figure 6. Position error comparison between the scalar tracking receiver (in red) and the VDFLL algorithm (in blue) for the (a) along-track error [m] and (b) cross-track error [m].

measurements. Furthermore, the ST + EKF covariance bounds are significantly increased during this period due to the higher position estimation uncertainty since only four "good" measurements from the four locked LOS satellites are used for the navigation solution computation. On the contrary, the proposed VDFLL algorithm assures a positioning stability and much tighter confidence bounds related to the interchannel-aiding capability exhibited by the VDFLL EKF filter. Finally, it can be seen that the vector architecture better assesses the confidence on the computed position.

5. Conclusions

The chapter was written in the context of the GNSS use in urban environment that is particularly challenging to the GNSS signal reception due to multipath and direct signal blockages, which significantly affect the signal processing and further degrade the position accuracy and availability. For this matter, this work was focused on the design of a dual-constellation GPS/Galileo and single-frequency L1/E1 band vector tracking architecture for automotive usage in urban environment. This architecture ensures a better receiver's dynamic estimation due to the joint code delay and Doppler carrier frequency tracking for all the satellites in view performed by the common navigation EKF filter. The detailed flowchart of the proposed vector tracking algorithm and the relation between the state vector and observation model were also exposed.

The generation of the urban environment multipath conditions was detailed in the second part of Section 4. In this work, the wideband propagation model referred to as the DLR land mobile multipath channel model was employed. Herein, the urban environment conditions were generated separately for each GPS- and Galileo-tracked satellite by feeding their elevation/azimuth angles and the reference car trajectory to the DLR urban channel. The generated channel model samples were stored and directly fed to the signal emulator at the correlator level.

Furthermore, the dynamic car trajectory along with the test parameters related to the scalar (ST) and vector tracking (VT) loop design was introduced. The emphasis of this work was dedicated to the performance analysis of the two architectures under study in the navigation level, expressed by the position estimation errors in the vehicle navigation frame. The VDFLL superiority was observed in the navigation domain, especially when referring to the position estimation accuracies. Nearly twice lower position estimation error variations were observed for the VDFLL architecture w.r.t the scalar receiver configuration. Furthermore, the VDFLL robustness and reactivity were noted especially during the satellite outage intervals that induce a reduced number of measurements fed to the navigation processor. During these intervals, stable and accurate navigation solution estimations are assured by the VDFLL filter thanks to the code/carrier NCO updates steered from the navigation solution estimations.

Acknowledgements

This work was financially supported by the EU FP7 Marie Curie Initial Training Network MULTI-POS (multi-technology positioning professionals) under grant no. 316528 and with the funding provided from Altran Research.

Acronyms and abbreviations

ADC	analog-to-digital converter
AGC	automated gate control

DLL	delay lock loop
DP	dot product
E	early
EMLP	early-minus-late power
EKF	extended Kalman filter
FLL	frequency lock loop
GNSS	global navigation satellite systems
I	in phase
IF	intermediate frequency
KF	Kalman filter
L	late
LNA	low-noise amplifier
LS	least squares
NCO	numerical control oscillator
P	prompt
PLL	phase lock loop
PVT	position velocity and time
Q	quadrature phase
SiS	signal in space
ST	scalar tracking
VT	vector tracking
VDFLL	vector delay/frequency-locked loop
WLS	weighted least squares

Author details

Enik Shytermeja

Address all correspondence to: enik.shytermeja@altran.com

Altran Technologies, France

References

[1] Dovis F, Mulassano P. Introduction to Global Navigation Satellite Systems. Politecnico di Torino; 2009

[2] Borre K, Akos DM, Bertelsen N, Rinder P, Jensen SH. A Software-Defined GPS and Galileo Receiver: A Single-Frequency Approach. Springer Science & Business Media; Birkhäuser Basel, eBook ISBN 978-0-8176-4540-3; 2007

[3] Kaplan E, Hegarty C. Understanding GPS: Principles and Applications. Artech House Boston; ISBN: 9781580538947; 2005

[4] Parkinson B. Introduction and heritage of NAVSTAR, the global positioning system. Global Positioning System: Theory and Applications. 1996;**3**:3-28

[5] Betz JW. Effect of linear time-invariant distortions on RNSS code tracking accuracy. In: ION GPS 2002: 15th International Technical Meeting of the Satellite Division of The Institute of Navigation. 2002

[6] Shytermeja Enik. Design and performance of a GNSS single-frequency multi-constellation vector tracking architecture for urban environments [PhD dissertation]. INPT; 2017

[7] Dierendonck VA, Fenton P, Ford T. Theory and performance of narrow correlator spacing in a GPS receiver. Navigation. 1992;**39**(3):265-283

[8] Julien O. Design of Galileo L1F receiver tracking loops. University of Calgary, Department of Geomatics Engineering; 2005

[9] Macabiau C, Ries L, Bastide F, Issler JL. GPS L5 receiver implementation Issues. In: ION GPS/GNSS 2003, 16th International Technical Meeting of the Satellite Division of the Institute of Navigation. 2003. p. 153

[10] Shytermeja E, Garcia-Pena A, Julien O. Proposed architecture for integrity monitoring of a GNSS/MEMS system with a fisheye camera in urban environment. In: Localization and GNSS (ICL-GNSS), 2014 International Conference on. IEEE; 2014. pp. 1-6

[11] Petovello MG, Lachapelle G. Comparison of vector-based software receiver implementations with application to ultra-tight GPS/INS integration. In: Proceedings of ION GNSS. Vol. 6. 2006

[12] Shytermeja E, Peña AJ, Julien O. Performance evaluation of VDFLL architecture for a dual constellation L1/E1 GNSS receiver in challenging environments. In: ION GNSS+ 2016, 29th International Technical Meeting of the Satellite Division of the Institute of Navigation. Institute of Navigation; 2016

[13] DLR, Technical note on the implementation of the land mobile satellite channel model—Software usage; 2007

Chapter 4

GPS Scintillations and Total Electron Content Climatology in the Southern American Sector

Emília Correia,
Marcio Tadeu de Assis Honorato Muella,
Lucilla Alfonsi, Fabricio dos Santos Prol and
Paulo de Oliveira Camargo

Additional information is available at the end of the chapter

http://dx.doi.org/10.5772/intechopen.79218

Abstract

The radio communication and navigation systems can be strongly affected by the ionospheric conditions, which are controlled by solar phenomena associated with radiation variations and solar wind disturbances. These phenomena can generate ionospheric large-scale plasma redistribution and irregularities with scale sizes varying from centimeters to hundred kilometers. These ionospheric irregularities can produce rapid fluctuations in the amplitude and phase of global navigation satellite system (GNSS) signals, degrading the accuracy of GNSS measurements. Here we give a short review of the ionospheric variations associated with solar phenomena, and the actual state of art in the investigations of long-term (seasonal and solar cycle scales) TEC variations and climatology of scintillations, with focus on the southern American sector. It also presented a new TEC calibration procedure when applied to single-frequency PPP.

Keywords: ionospheric irregularities, scintillation, total electron content, climatology, South America, single-frequency PPP

1. Introduction

Nowadays, the global navigation satellite systems (GNSSs) are widely used in many human activities, particularly for geodetic positioning and navigation, as well for atmospheric monitoring in scientific research. The GNSS systems have been used to obtain the ionospheric total electron content (TEC) often in near real-time and in global scale because the networks ground-based receivers cover large geographic areas. In the last decades, TEC information has given a great advance in the understanding of the ionospheric structuring and improving our forecasting capacity, which has revolutionized the ionospheric studies. Particularly, the behavior of the ionosphere during geomagnetic disturbed periods has been extensively investigated, showing that F-region response to geomagnetic storms is very complex in space and time, but a general morphology and physical processes have been defined (e.g., [1–13]; and references therein).

The ionospheric knowledge has been used to improve the GNSS positional accuracy, which can be strongly degraded under severe atmospheric disturbances because they can suddenly change the satellite geometry that is essential for geodetic position, in particular for kinematic precise point position (PPP), and are a limiting factor to achieve centimeter accuracy (e.g., [14–16]). The main atmospheric disturbances that affect the GNSS quality signals are the ionospheric steep density gradients, signatures of irregularities of the electron density distribution. Special attention has been given to the ionospheric irregularities investigation, which can vary on a wide range of scale sizes, from centimeters to hundreds of kilometers. The formation and the temporal/spatial evolution of these irregularities affect the propagation of radio signals, causing cycle slips and loss of lock on GNSS receivers and degrading the performance of radio communication and navigation systems [17, 18]. At L-band, amplitude scintillations are due to irregularities with a scale size from hundreds of meters down to tens of meters (according to Fresnel's filtering mechanism), while phase scintillations are caused by structures from a few hundred meters to several kilometers (see, e.g., [18]). In addition, in your way down to the ground, the radio signals could interfere with itself due small changes in their way along the scattered ray paths, resulting in a sort of "space multipath" [19]. The overall of these atmospheric influences can produce rapid fluctuations in the amplitude and phase of GNSS signals, which are known as ionospheric scintillations.

The investigation of scintillations has shown that their activity is stronger at latitudes within the equatorial ionization anomaly (EIA), particularly during post-sunset hours when plasma bubbles are formed in the equatorial F-region driven by the Rayleigh-Taylor instability [20, 21]. Recently, the formation of ionospheric irregularities and plasma bubbles at equatorial region also have shown that they can be driven by gravity waves [22, 23]. The scintillations have been extensively studied at different longitudinal sectors and latitudes, showing a strong dependence on magnetic local time, season, magnetic activity, solar cycle, and geographic location (e.g., [6, 8–13, 19, 24–36]; and references therein).

This chapter provides the characterization of ionospheric scintillations observed with GNSS networks in the South American sector (e.g., [34, 35, 37–40]). The chapter is organized as follows: Section 2 presents the ionospheric variability, Section 3 presents the ionospheric scintillation indices and climatology in South American sector, Section 4 presents the impact of scintillations in a new method for high accurate single frequency precise point positioning (PPP), and finally a discussion section.

2. Ionospheric variability

The solar heating throughout the atmosphere causes large-scale variations associated with diurnal and semidiurnal tides in the thermosphere [41], while the extreme ultraviolet radiation

(EUV) forms the ionosphere. The physical processes in the thermosphere are primarily driven by solar and magnetic disturbances [42], which influence the ionospheric production and recombination, as well transport and frictional heating. The ionospheric conditions have been studied for decades, and particularly there is a good understanding of F-region conditions associated with seasonal, solar cycle, and level of magnetic activity variations. Despite that the predictive capability of its condition is still very poor because the variations appear over a wide range of timescales going from minutes to several days and also depend on the magnetic local time and geographic location. Even during quiet times, that is, under undisturbed geomagnetic conditions, significant ionospheric variability is observed. The low latitude ionosphere is controlled by electrodynamic plasma ($\mathbf{E} \times \mathbf{B}$) drifts driven by thermospheric neutral winds (e.g., [43–45]). The zonal electric fields drive strong daytime E-region eastward currents in the equatorial region, which form two narrow latitudinal bands centered at the dip equator that are called equatorial electrojet (e.g., [46]). The zonal electric fields drive equatorial E and F region vertical plasma drifts (e.g., [47]) that lift the ionospheric plasma at the dip equator, which goes down following the magnetic field lines leading density enhancements located at ~±10–20° from the magnetic equator. The overall process, the plasma lifting followed by their diffusion along the geomagnetic field lines and the formation of the two density maxima away from the equator, is called "fountain effect," and the denser regions are called the crests of the equatorial ionospheric (or ionization) anomaly (EIA) [48]. The thermospheric winds are highly variable because they are driven by changes in the global tidal forcing, and effects of irregular winds, planetary and gravity waves. The planetary waves and tides have been identified as relevant factors affecting the electrodynamics of the lower thermosphere (e.g., [49–55]).

The ionospheric F-region often becomes turbulent and develops electron density irregularities during post-sunset hours [56]. During the day, the electrical field is eastward and it reverses to the west after sunset, but during sunset an enhanced eastward electric field develops, the so-called pre-reversal enhancement (PRE) [44, 57, 58]. The PRE drives an upward vertical plasma drift at magnetic equatorial region, and the bottom of the F-region becomes unstable to the Rayleigh-Taylor instability [59], developing large-scale plasma depletions (plasma bubbles). These bubbles ascend upwards over the magnetic equator, causing a redistribution of ionization similar to the fountain effect. The latitudinal extension of the plasma bubbles is defined by the upper height limit they reach in their rise up above the magnetic equator [60] and can intersect the crests of the EIA, where the steeper density gradients on the edges of the plasma bubbles favor the generation of smaller scale irregularities [56, 61, 62]. The plasma bubbles practically disappear after local midnight and are most intense during the equinoctial months and during the solar maximum years [63, 64]. These conditions favor the scintillations to occur most frequent and severe around the EIA crests, in particular after sunset due to the generation of irregularities caused by the intersection of the plasma bubbles with the regions of larger background electron density.

The ionosphere can be strongly disturbed during geomagnetic storm-time periods. These storms are terrestrial magnetospheric perturbations caused by the impact of interplanetary coronal mass ejections (ICMEs), and corotating interaction regions associated with high-speed streams (HSS), which are the most geo-effective solar wind phenomena. The coupling process involving the solar wind, the interplanetary magnetic field (IMF) and the magnetosphere strongly affects the high latitude ionospheric electrodynamics. The magnetosphere compression during geomagnetic storms induces intense electric fields and increases its convection. During these processes, the interplanetary electric field (IEF) is mapped along the magnetic field lines to the high latitude ionosphere, but can also propagate across them and promptly appears in the low latitude ionosphere, when it is called of prompt penetration electric field (PPEF). The effect of PPEF at the equatorial ionosphere has been observed during the first hours of the main phase of geomagnetic storms, suggesting a long-duration penetration of interplanetary electric field to the low-latitude ionosphere without shielding (e.g., [5, 65–68]). The equatorial ionosphere under the effect of the PPEFs is convected upward in the dayside and downward in the night side [66]. The PPEFs are stronger than the fields associated with the normal fountain effect resulting in a higher elevation of the equatorial plasma [5], and consequently the crests of the EIA departs more from magnetic equator and can reach middle latitudes (~±20–30°). At high latitudes, the precipitation of energetic particles enhances ionospheric conductivities and generates intense electrical currents in the auroral zone [3]. The dissipation of these currents by the Joule effect heats the local plasma that expands, changing the lower thermospheric composition and driving large-scale neutral winds [3, 4, 42]. Thus, major geomagnetic storms results in a large-scale ionospheric thermal plasma redistribution involving all latitudes from the equatorial through the polar region. Particularly F2-region shows very complicated spatial and temporal behavior (e.g., [9]), but a general morphology and physical processes have been established (e.g., [1–4, 7, 9]). F2-region variations during geomagnetic disturbed periods are called ionospheric storms and are detected as an increase (positive) or depletion (negative) of electron density associated with electrodynamics processes or neutral composition changes (e.g., [4]), respectively. Their morphology is a function of the amount of energy inputted in the high latitude during the main phase of geomagnetic storm [69], as well of the station latitude and longitude, local time of storm onset, storm time and season.

3. Ionospheric scintillations

3.1. Scintillation indices

Scintillations are rapid fluctuations in the amplitude and phase of GNSS signals produced by the ionospheric irregularities, which are responsible by the refraction and diffraction of trans-ionospheric signals [20, 70].

The ionospheric scintillations are evaluated from 60 s amplitude (S4) and phase scintillation (Phi60) indices, which give information about intermediate (around hundreds of meters) and large (above hundreds of meters)-scale size irregularities, respectively. The scintillation indices are obtained by using GNSS dual-frequency receivers recording data at a high data sampling rate of 50 Hz, which also compute the total electron content values.

The S4 index can be interpreted as the standard deviation of the received power (C/NO) normalized by its mean value and the Phi60 index is the standard deviation (in radians) of the carrier phase computed over 60 s time interval. The indices are obtained as Eqs. (1) and (2) [71].

$$S4 = \sqrt{\frac{<I^2> - <I>^2}{<I>^2}}, \tag{1}$$

$$Phi60 = \sqrt{<\varnothing^2> - <\varnothing>^2}, \tag{2}$$

Class	Index value
Weak	$0.1 < S4 < 0.25$ or $0.1 < Phi60 < 0.25$
Moderate	$0.25 < S4 < 0.7$ or $0.25 < Phi60 < 0.7$
Strong	$S4 > 0.7$ or $Phi60 > 0.7$

Table 1. Classification of the ionospheric scintillation severity.

where <> denotes 60 s average, I is the signal intensity and ∅ the signal phase at GPS L1 frequency (1.575 GHz) sampled at 20 ms (50 Hz).

The S4 and Phi60 indices are used to classify ionospheric scintillation severity, which can be separated in three categories: strong, moderate and weak scintillations, for example, as shown in **Table 1**.

3.2. Ionospheric scintillation climatology in south American sector

The morphology of the Earth magnetic field favors the occurrence of strong scintillations at high latitudes, and intense at equatorial region between about 20°N and 20°S magnetic latitudes [20, 72]. Particularly in the South American sector, the F-region irregularities present peculiarities due to the large longitudinal variation in the magnetic declination angle [38, 73, 74], as well by the influence of the South American Magnetic Anomaly (SAMA). The SAMA is the region on the Earth where the magnetic field has the lowest intensity values, allowing enhancement of energetic particle precipitation into the atmosphere [75]. The enhanced ionization in the SAMA region produced by the particle precipitation is a regular feature, which modifies the quiet ionospheric physical conditions increasing the F-layer vertical drift over the eastern sector as compared to the western sector of South America, which can be drastically modified during magnetospheric disturbances (e.g., [75]; and references therein).

The investigation in the South America sector has been improved in the last decades after using GNSS receivers networks dedicated to monitor ionospheric scintillations. Today, there are three GNSS networks, the GPS Low-Latitude Ionospheric Sensor Network (LISN) that is operating since November 2011 with an array of 45 receivers [76], 15 of them over the Brazilian territory, where they are complimented with one array of 12 GPS Ionospheric Scintillation Monitoring Receivers (ISMR) of the GPS Scintillation Monitors network (SCINTMON) [38] and other with 10 ISMR of the Concept for Ionospheric Scintillation Mitigation for Professional GNSS in Latin America and Countering GNSS high Accuracy applications Limitations due to Ionospheric disturbances in Brazil (CIGALA/CALIBRA) project [77]. At high latitude, these networks are complimented with GPS ionospheric scintillation and total electron content (TEC) monitor receivers (GISTM) that covers a large area from sub-equatorial Latin America to the South Pole [71].

3.2.1. Quiet geomagnetic conditions

Ionospheric irregularities commonly appear in the regions of enhanced or depleted electron density. These regions are associated with the crests of the EIA anomaly located at latitudes ~15–20° from the magnetic equator, where strong scintillations have been observed particularly during sunset hours. Before GNSS era, Aarons [20] using ionosondes and VHF systems showed the scintillation intensities, produced by smaller scale ionospheric irregularities, were stronger in the EIA crests after sunset hours under the influence of plasma bubbles. A comprehensive study of the occurrence of irregularities over the south EIA crest in Brazil during two decades was reported by Sobral et al. [21], which shows the plasma bubbles occurrence has a broad maximum around summer months (from September to April), with a significant increase from low to high solar activity levels during the equinoctial months of March-April and September-October. De Paula et al. [38], using GPS L1-band receivers in the Brazilian territory, reported the characteristics of small-scale irregularities that produced strong scintillations in the post-sunset equatorial ionosphere from 1997 to 2002, the ascending phase of the solar cycle 23. They reported that the ionospheric irregularities are stronger in the southern crest of the EIA, and present a seasonal variation occurring predominantly from September to March during magnetic quiet periods, being more intense during December (local summer). They also show a large longitudinal variation in the South American sector showing that the irregularities are most intense in the EIA crest in Brazilian sector than over Argentinean sector, which is attributed to the large longitudinal variation of magnetic declination in this sector. During quiet magnetic periods, the irregularities occur in the sunset-midnight local time sector while during magnetic storms their occurrence can extend to the midnight-sunrise sector. Akala et al. [39] using a chain of GPS receivers along the western longitude sector of South America, during different levels of solar activity, also shows the scintillations occur predominantly at post-sunset hours and decay before or around local midnight, with stronger activity and longer durations in the months of March and January, which means in the March Equinox and December solstice; and in particular the station near northern crest of the EIA recorded the highest occurrences of scintillation especially during periods of high solar activity.

Spogli et al. [24], using GISTM receivers located between South America, South Atlantic Ocean and Antarctica, defined crucial areas in the ionosphere where the probability of scintillation occurrences is higher. These areas were called ionospheric scintillation "hot-spots" and were defined using a climatological representation given by the Ground Based Scintillation Climatology (GBSC) technique [19]. They showed that there are two main hot-spots over South America, first one associated with the post-sunset (POST) hours at low latitudes located in the magnetic latitude (MLAT) range 15–25°S and magnetic local time (MLT) between 20 and 24 h, and another one associated with particle precipitation region (SAMA) nearby SAMA region located in the MLAT range 22–24°S and MLT between 0 and 24 h. At high latitudes, they identified three scintillation hot spots, one associated with particle precipitation region in the polar cusp (CUSP, MLAT: 74–82°S and MLT: 10–14 h), other associated with place where the irregularities are induced by reconnection from the magnetotail (MLAT: 68–82°S, MLT: 20–4 h), and other one associated with polar cap patches (PATC, MLAT: 82–90°S, MLT: 0–24 h). The POST hot spot shows scintillation intensifications in March and November, in agreement with the intensification of pre-reversal at equinoxes (e.g., [78]). The hot-spot intensification is stronger in November probably due to the superposition effects associated with the spring equinox and the local summer. The SAMA hot spot also shows one stronger enhancement in November similarly the observed at POST hot spot. They also confirm that in the Brazilian longitudes, the irregularities are more intense in the September (spring) equinox and summer months [38]. At high latitude the two main hot spots identified as CUSP and PATC show enhancements at equinoxes that are attributed to direct particle precipitation.

Muella et al. [34] investigated the scintillation occurrence from 2002 to 2006, during the descending phase of the 23rd solar cycle, at two sites located in the inner regions of the northern and southern crests of the equatorial ionization anomaly in the Brazilian sector. They showed that the scintillation occurrences during sunset hours present a north-south asymmetry, being ~10% higher over the southern EIA crest than over northern one during solar maximum. This asymmetry was considered to be a possible influence of the SAMA on the scintillation activity. The scintillation occurrence also showed a broad minimum in June and maximum in December over both crests. On a recent investigation of scintillation occurrence at Cachoeira Paulista near the south EIA crest, covering almost the two last solar cycles (1998–2014), Muella et al. [37] showed that the maximum occurrence of scintillations observed during the peak of 23rd solar cycle was 20% higher than that one observed for the 24th, which was the weakest cycle in the last century. This behavior can be attributed to the scintillation intensity dependence on the electron density gradients and the thickness of irregularity layer, which are driven by the intensity of the solar extreme ultraviolet radiation (EUV). In addition, the fewer occurrences of scintillation in the maximum of the 24th solar cycle at Cachoeira Paulista could also be associated with the secular variation in the dip latitude, which changed ~3° in south direction from 1997 to 2014.These results on the long-term trend analysis and climatology of scintillations at the EIA region are shown in **Figure 1**. The colored contours in the upper panel of **Figure 1** show the nocturnal occurrence statistics of scintillation from 1998 to 2014 for $S_4 > 0.2$ as function of universal time (UT = LT + 3 h) and the mean F10.7 cm solar flux index. For the type of the GPS receiver used to measure scintillations, the threshold of $S_4 > 0.2$ can be considered above the level of multipath and noise effects, which may produce very weak scintillations ($S_4 < 0.2$). The middle panel shows the occurrence for the strongest levels of scintillations (threshold of $S_4 > 0.5$), whereas the color scale bar indicates the percentage of occurrence used in the plots of scintillation statistics. The monthly mean variation of the F10.7 cm solar flux is shown in the lower panel and depicts its changes from the ascending phase of solar cycle 23rd to the maximum of solar cycle 24th. **Figure 1** reveals that the patches of larger occurrence of scintillations are observed from 23:00 to 04:00 UT between the months of September and March and mainly around the solar maximum years.

The climatology of the onset time of ionospheric scintillations near the southern crest of EIA over Brazilian territory, covering a period between solar cycles 23 and 24, showed that their start time is about 40 min earlier in the months of November and December when compared to January and February, suggesting an association with the ionospheric pre-reversal vertical drift (PRVD) magnitude and time [79].

An investigation of the equatorial scintillations over São Luis (2.33°S, 44.21°W, dip latitude 1.3°S) was done by Muella et al. [35] during different solar activity levels of the 23rd solar cycle (1999–2006). The study showed the scintillations occurred more frequently during the years of high solar activity, but strong scintillation variability was also observed during the descending phase of the solar cycle. The scintillations occurred predominantly during pre-midnight hours with a broad maximum in the summer. They observed a weak level of scintillations all

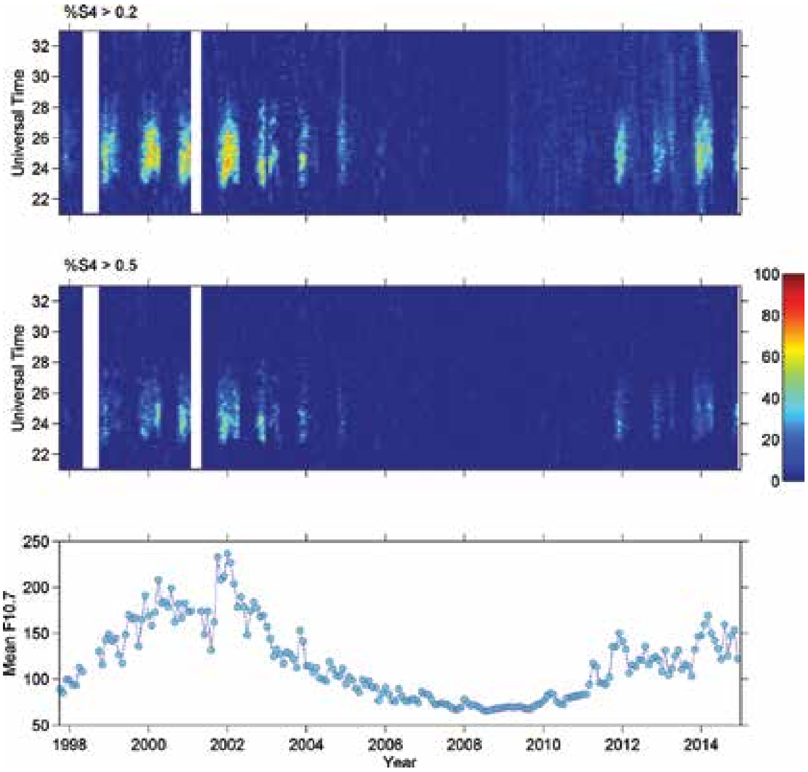

Figure 1. Occurrence climatology of the GPS L1-frequency scintillation (1998–2014) at Cachoeira Paulista for two threshold levels of the S_4 amplitude scintillation index as function of universal time (UT = LT + 3 h) and the mean solar radio flux in 10.7 cm (F10.7 index). The upper and middle panels denote the nocturnal occurrence climatology for the levels of $S_4 > 0.2$ and $S_4 > 0.5$, respectively. The colored bar indicates the percentage of scintillation occurrence used in the plots. The monthly mean variation of the F10.7 cm solar flux is shown in the bottom panel to depict the changes in the solar cycles. [after Muella et al. [37]. Reproduced with permission of the Copernicus publications on behalf of the European geoscience union].

over the year, however, during the winter months near the years of solar maximum, some stronger levels of scintillations were observed at comparable rate with the weak scintillations.

The ionospheric scintillations are driven by zonal drift of the irregularities, so the investigation of the spatial and temporal variations of the irregularities have been done in the last decades. The study of the zonal drift driven scintillations in the South American sector has shown that: a latitudinal gradient in the irregularity zonal velocities is associated with the vertical shear of the zonal drift in the topside equatorial ionosphere [80]; at two magnetic conjugate sites over Brazilian territory, the magnitude of the zonal velocities in the site inside the SAMA region was ~12% larger than in the conjugate one [81]; during nighttime, there is a strong correlation between neutral winds and scintillation drifts near magnetic equator [82]; the irregularity of the zonal drifts shows a negative gradient with increasing geomagnetic latitude [83]; and that the magnitude of the zonal velocities might be reduced at the inner regions of the EIA due to the latitudinal variation in the ion drag force [35]. The nighttime zonal drift velocities of the ionospheric irregularities increase in association with increasing EUV solar radiation [37, 84, 85], which can be produced by the fact that in years of higher solar activity, the thermospheric zonal wind velocities are higher enhancing the solar thermal tide [86].

3.2.2. Disturbed geomagnetic conditions

The ionospheric electrodynamics conditions depend on magnetosphere-ionosphere-thermosphere system, which can be strongly disturbed during geomagnetic storms. During geomagnetic storms, the magnetosphere is compressed inducing intense electric fields and increasing the magnetospheric convection. The strongest geomagnetic storms are mainly produced by the impact of solar wind disturbances associated with geoeffective solar coronal mass ejections (CMEs) and coronal hole solar high speed streams (HSS) on the magnetosphere, which results in a highly inhomogeneous ionosphere, producing steep electron density gradients and irregularities. The ionospheric electron density distribution changes as a function of the solar wind input energy in the high latitude upper atmosphere, which occurs during the main phase of the geomagnetic storms [69].

The spatial and temporal variations of F2-region during geomagnetic storms are called ionospheric storms, and their morphology depends on the site location, local time of geomagnetic storm onset, storm time and season. Despite the very complex ionospheric behavior during disturbed periods, there is a general understanding about its morphology and physical processes (e.g., [1–4, 7, 9]). The negative phase of ionospheric storm is attributed to changes in the thermosphere at middle and high latitudes due to the heating in the auroral zone, mainly by Joule dissipation [87], occurring at all seasons but in winter. In contrast, the positive phase occurs at middle and low latitudes mainly in winter season and involves more complex physical processes associated with uplifting due vertical drift, plasma fluxes from the plasma sphere, and downwelling produced by storm-induced thermosphere circulation at low latitudes (e.g., [3, 7, 9]). The vertical drift during daytime is controlled by equatorward winds at middle latitudes during the winter, and at equatorial region is driven by the EIA anomaly in association with prompt penetration electric field effect (PPEF) [5], resulting in an enhancement of the electron concentration because the photoionization is still operating (e.g., [3, 88]).

At middle latitudes, TEC enhancements are observed during the main phase of geomagnetic storms in the dusk sector, which are called storm-enhanced density (SED), and have been associated with large-scale redistribution of ionospheric plasma, covering a large extension from equatorial to polar region [89]. This phenomenon has been observed during the first hours of the main phase storm when the fountain effect at the equatorial region is reinforced by the PPEF, moving EIA crests from low to middle latitudes. The middle latitude EIA crest at dusk sector, under electrodynamic processes, has its plasma redistributed in longitude and latitude generating plumes of SED [90], which can be transported into dayside cusp where enter the polar cap and form the called tongue of ionization (TOI; [8, 10–13, 24, 89]; and references there in) at polar region. The ionospheric plasma redistribution during geomagnetic storms is a function of their intensity, magnetic local time, storm time, latitude and season.

The ionospheric regions affected by impact of geomagnetic storms show a strong intensification of scintillation occurrence. At high and middle latitudes, these regions are the night side auroral oval due to the particle precipitation events [12, 91, 92], the cusp on the dayside in association with SED, and the polar cap in association with TOI, while at equatorial latitudes the scintillations are associated with regions under the influence of the EIA anomaly. Similarly, the ionospheric storms, the occurrence of scintillations during geomagnetic disturbed periods also are function of magnetic local time, season, magnetic activity, solar cycle, and geographic location [12, 13, 19, 25, 26]. The ionospheric irregularities can be inhibited during magnetic storms with main phase occurring during daylight hours, but can be intensified during any season when main phase storm coincides with the hours of the pre-reversal electric field is maximum (e.g., [75]). De Paula et al. [38] from an investigation of small scale irregularities (~400 m) at equatorial and low latitudes over Brazilian territory obtained that during geomagnetic storms they can occur at any epoch of the year, present largest intensities in the south EIA crest, could extend from sunset-midnight to midnight-sunrise sector during some storms, are enhanced during PPEF occurring during post sunset hours, and can be suppressed during daytime main phase storm under the disturbance dynamo effect. In association with geomagnetic storms, the large-scale irregularities (few km) have shown a seasonal variability [93]. On the other hand, an investigation of the F-region under the impact of the geomagnetic storm occurred on June 2013, from equatorial to middle latitudes in both hemispheres over American sector, showed that the ionospheric irregularities were observed confined in the equatorial region before and during the storm, which shows this storm did not affect the generation or suppression of irregularities [94].

An investigation of the 26–27 September 2011 moderately intense geomagnetic storm impact in the ionosphere at middle and high latitudes in the South American sector showed that during its dayside main phase two SEDs were observed at middle latitudes [13]. These SEDs were attributed to a combination of processes, including the PPEF effect from low latitudes during a couple of hours just after the storm onset, and dominated by the disturbance dynamo effect from high latitudes during its evolution. The plumes of these SEDs were located near the dayside cusp and result in TOI formations observed in nightside polar cap region. In association with the middle latitude SEDs and polar cap TOIs were observed strong ionospheric scintillations.

4. The impact of ionospheric scintillations in a new single-frequency PPP method

New analysis about the GNSS positioning was performed by Prol et al. [95] in order to evaluate the ionospheric delay retrieved by a new method for TEC calibration when this method was applied to correct the single-frequency PPP. The results revealed the possibility of performing the single-frequency PPP corrected by a TEC calibration and obtaining a similar accuracy to the double-frequency PPP. It suggested that almost all of the first-order ionospheric effect was eliminated by the TEC calibration method. Additionally, the single-frequency PPP corrected by the new method was very sensitive to the impact of the ionospheric scintillations. In fact, the proposed single-frequency PPP appeared to be even more sensitive to ionospheric scintillation in comparison with the single-frequency PPP corrected by traditional ionospheric models and the double-frequency PPP. In order to present the impact of the ionospheric scintillations in the proposed single-frequency PPP, this section describes the developed method for TEC calibration and some experiments and results.

TEC can be expressed as the integral of the electron density n_e along the path between the GNSS satellite (s) and the receiving antenna (r), in a column whose cross sectional is equivalent to 1 m^2. It can be written as:

$$TEC = \int_{\mathrm{r}}^{s} n_e \, ds, \tag{3}$$

being the ionospheric delay given by the following relation with TEC:

$$I = \frac{40,3}{f^2} TEC, \tag{4}$$

where I represents the ionospheric delay and f the signal frequency.

The ionospheric delay is related to the GNSS observations by the following equation for the code:

$$P_L = \rho + c(d\,t_r - d\,t^s) + I_L + T + d\,m_L + \epsilon_P, \tag{5}$$

and the following equation for the carrier phase:

$$\lambda_L \phi_L = \rho + c(d\,t_r - d\,t^s) - I_L + T + d\,m_L + \lambda_L N_L + \epsilon_\phi, \tag{6}$$

where the frequency-dependent terms are referred by L, ρ is the geometric distance, c is the speed of the light in vacuum, $d\,t_r$ and $d\,t^s$ are the receiver and satellite clock errors, T refers to the tropospheric delay, dm is the multipath, N_L is an ambiguity term, λ is the wavelength and ϵ represents the noise in code (P) and phase (ϕ).

The method to estimate TEC (Eq. (3)) using GNSS observations (Eqs. (5) and (6)), is performed in three steps. In the first step, a phase leveling estimation based on the code information provides the ambiguity terms. In this regard, the difference between ambiguities (ΔN) of two GPS frequencies (L1 and L2) in a unique arc of data is calculated through:

$$\Delta N = (\lambda_1 N_1 - \lambda_2 N_2) = \frac{1}{n_{obs}} \sum_{j=1}^{n_{obs}} \left[(P_{2j} - P_{1j}) - (\lambda_1 \phi_{1j} - \lambda_2 \phi_{2j}) \right], \tag{7}$$

where only arcs with a minimum of 5 min of continuous data are used. Once the ΔN term is obtained for all arcs of a specific day, the receiver DCB (Differential Code Bias - $\Delta\,b_r$) is obtained by the daily weighted mean of the phase difference ($\lambda_1 \phi_{1j} - \lambda_2 \phi_{2j}$), the initial TEC, the leveling ambiguity and the satellite DCB ($\Delta\,b_s$). The receiver DCB is derived by the following weighted mean:

$$c\Delta\,b_r = \frac{1}{\sum_{i=1}^{n_{arc}} \sum_{j=1}^{n_{obs}} w_{ij}} \sum_{i=1}^{n_{arc}} \sum_{j=1}^{n_{obs}} w_{ij} \left[(\lambda_1 \phi_{1j} - \lambda_2 \phi_{2j}) - \frac{TE\,C_{ij}^{gim}}{F} - \Delta N - \Delta\,b_{si} \right], \tag{8}$$

with

$$F = \frac{f_1^2 f_2^2}{40.3(f_1^2 - f_2^2)} \text{ and } w_{ij} = \frac{1}{(\sigma TE\,C_{ij}^{gim}/F)^2}, \tag{9}$$

being σTEC_{ij}^{gim} the standard deviation of the initial TEC, which is derived from the Global Ionospheric Maps (GIMs) of the International GNSS Service (IGS) and their root-mean-square (RMS) maps. In addition, the satellite DCB Δb_{si} is obtained from GIMs. Therefore, as the satellite DCB and the initial TEC are obtained from GIMs, it is expected that the estimated receiver DCB is related to the DCB referential frame defined by IGS.

Once the ambiguity leveling (first step) and the receiver DCB estimation (second step) are done, the third step consists in the TEC estimation. TEC is directly calculated along the path of the GNSS signal with the following equation:

$$TEC = F\left[\left(\lambda_1 \phi_1 - \lambda_2 \phi_2\right) - \Delta N - c\left(\Delta b_s + \Delta b_r\right)\right], \tag{10}$$

where the TEC is derived for each GNSS observation, that is, TEC is estimated with the same time resolution as the phase and code collection rate.

Two close GNSS stations located at Rio de Janeiro in Brazil have been selected to make the experiments. The TEC estimation procedure was performed in the station RIOD (lat. Mag. 36.47° S), and the ionospheric delay correction was applied in the station ONRJ, which is located 12 km away. Using the configuration of short distances apart, it is possible to mitigate the problems of spatial gradients of the ionosphere. In addition, the receivers and antennas are from different brands in order to avoid possible correlations between clock and ambiguities of the stations. In this way, it has been as much as possible to isolate the degradation of the ionospheric scintillations in the PPP results.

Prol et al. [95] evaluated the analysis of the performance of the new TEC calibration procedure when applied to PPP for 120 days with six distinct configurations of base and rover stations, and the TEC performance is assessed by applying the estimated TEC from the base station to correct the ionospheric delay in a nearby rover receiver. Just to show the potentiality of the new procedure, here are shown the results of the analysis for two specific days with and without ionospheric scintillations.

Figure 2 shows an example of the calibrated TEC in RIOD during epochs with and without evidences of ionospheric scintillations. Each colored line represents the slant TEC calculated for a distinct satellite, that is, one colored line refers to the slant TEC of one GPS satellite. The Day Of Year (DOY) 005 of 2013 is shown in the top panel, which refers to the summer solstice in the south crest of EIA. On the other hand, DOY 191 of 2013 is referred to the winter. As it can be seen, the maximum of TEC in the summer solstice reaches around 150 TECU in the slant direction during the daytime. The magnitude of the TEC in daytime is reduced in the winter for up to 100 TECU, mainly due to the reduced intensity of the solar irradiation. However, TEC variability in the daytime is similar. In contrast, the nighttime between 22 and 04 LT presents a significant difference in terms of the TEC variability. The maximum TEC in the nighttime is reduced from 60 TECU in the solstice up to 30 TECU in the winter. Additionally, the high TEC variability evidenced between 22 and 04 LT is associated to the plasma depletions propagating trough the Brazilian region. In fact, the high magnitude of the TEC observations in comparison with the TEC variability makes the impact of the ionospheric

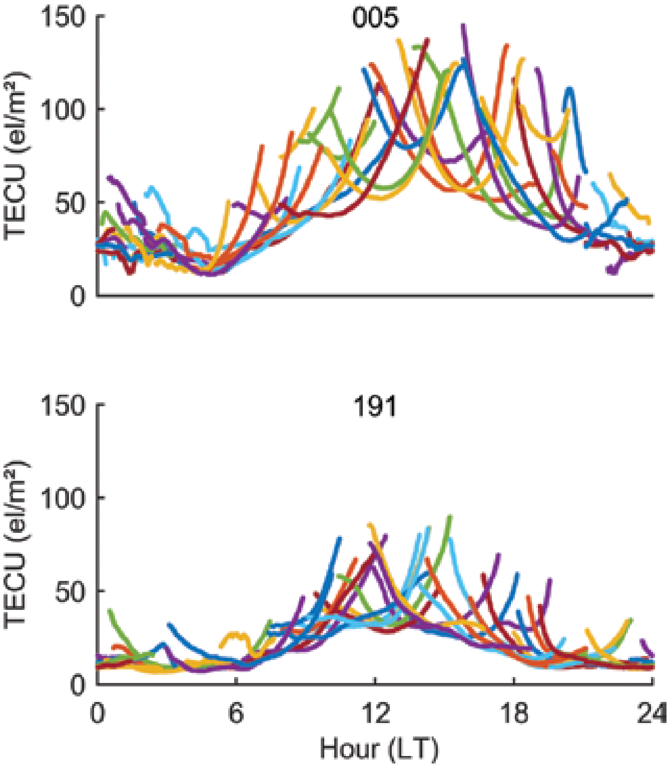

Figure 2. TEC estimation with the proposed procedure at RIOD station on 2013 for DOY 005 during the summer (top panel) and DOY 191 during the winter (bottom panel). Each colored line represents the slant TEC calculated for a distinct GPS satellite.

scintillation not so clearing TEC. However, the impact of the ionospheric scintillations is much more easily seen when looking to the single-frequency PPP performance.

RTKLIB is adapted for the use of the calibrated TEC during the single-frequency PPP. Among the PPP configurations, it is used the kinematic mode, a combined solution obtained by forward and backward filters, a cut-off angle of 10°, Earth tides corrections, the estimation of tropospheric delay during PPP, IGS precise ephemerides, satellite clock corrections with a 30 s rate (clk_30s), global positioning system constellation, correction of the phase center variation of the antenna, phase wind up corrections, no strategy for ambiguity solution and corrections of the differential instrumental bias between the civil and precise codes (C1-P1) when P1 was not available. In general, three modes of PPP are analyzed: (1) using the ion-free observation (PPP/if); (2) using L1 and the ionospheric delay from GIMs from UQRG (UPC Quarter an hour Rapid GIM), identified as PPP/uqrg; and (3) using L1 and the calibrated TEC through the proposed method (PPP/tec). Indeed, the PPP/if solutions are obtained using the ion-free observation of the carrier phase, which means that a linear combination is carried out with the L1 and L2 frequencies to eliminate the first-order effect in the ionospheric delay. In the case of PPP/uqrg, the observation used in the PPP Kalman Filter is related to the L1 frequency but corrected from the ionospheric delay derived from UQRG GIMs. The PPP/tec is similar to PPP/uqrg, but the ionospheric delay is derived directly from Eq. (10). The reference coordinates of ONRJ has been obtained from the Sistema de Referencia Geocéntrico para las Américas (SIRGAS) final solutions at epoch 2013, where a time update was performed to make the coordinates consistent with the PPP solutions.

Figure 3 shows the performance of PPP/if, PPP/tec and PPP/uqrg in terms of the three-dimensional (3D) error of the estimated coordinates. Each point represents the error of the PPP solution calculated in each processing epoch in kinematic mode. Since it was used a combined filter of forward and backward solution, there is no need for time convergence in the solution. Consequently, the remaining errors are related to the terms not efficiently mitigated and, as can be seen, the PPP/tec (blue points) was obtained with a high accuracy in many hours, except to the hours when is typically observed ionospheric scintillations.

In general, the proposed method allowed having the single-frequency PPP with a similar accuracy than the double-frequency PPP. The root mean square error (RMSE) obtained for PPP/if in DOY 191 was 0.04 m with a standard of 0.04 m, the RMSE of PPP/tec was 0.09 m with a standard deviation of 0.04 m and the RMSE of PPP/uqrg was 0.47 m with a standard deviation of 0.65 m. In the case of DOY 005, the RMSE of PPP/if was 0.04 m with a standard of 0.04 m, the RMSE of PPP/tec

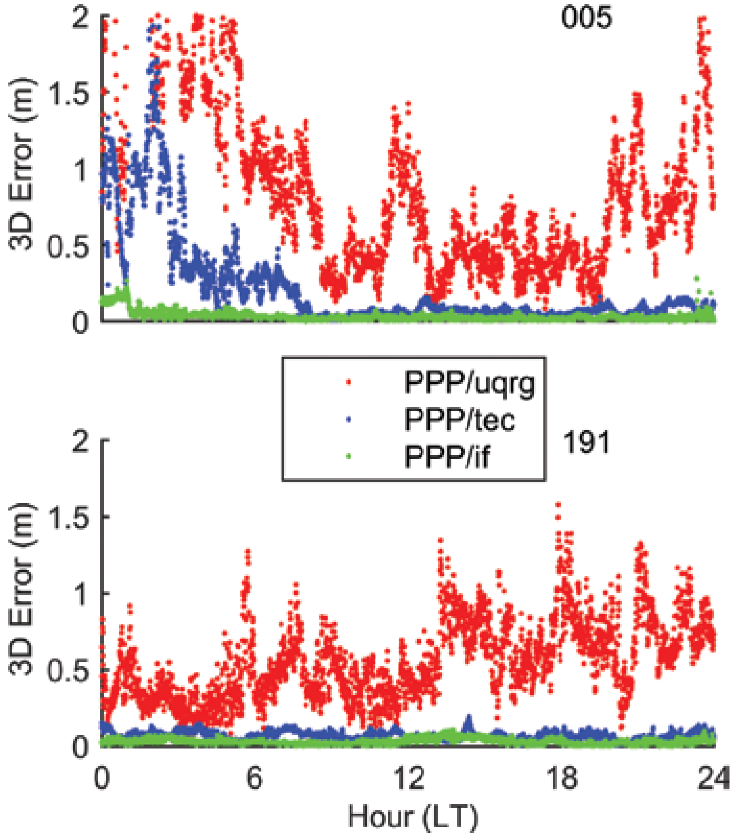

Figure 3. 3D error of PPP at ONRJ station on 2013 for DOY 005 during summer (top panel) and DOY 191 during winter (bottom panel).

was 0.19 m with a standard deviation of 0.05 m and the RMSE of PPP/uqrg was 0.70 m with a standard deviation of 0.66 m. By itself, this is an outstanding result, since many researchers have already used single-frequency receivers and ionospheric corrections to obtain, in general, an absolute accuracy of 0.5 m in the horizontal and 1 m in vertical for the kinematic PPP [96–98]. Now, we are showing the possibility of obtaining the single-frequency PPP accuracy similar to that from dual-frequency PPP. The horizontal accuracy in the experiment for PPP/tec was 0.12 m in DOY 005 and 0.05 m in DOY 191 and the vertical accuracy was 0.15 m in DOY 005 and 0.07 m in DOY 191. These accuracies are compatible to the double-frequency solutions. Therefore, the unique consideration for a high accuracy in single-frequency PPP is that TEC needs to be sufficient precise, which was not realistic in some epochs of DOY 005 due to the ionospheric scintillations.

A noticeable degradation of the PPP solution occurs between 00 and 04 hours LT in the summer solstice due to the high TEC variability. This PPP degradation is related to the ionospheric irregularities that impact GPS observations more effectively. At such instances, the uplifted ionosphere due to the pre-reversal drift produces high vertical gradients. It is believed that these gradients set the preconditions for plasma instability, controlling the generation of ionospheric irregularities. Therefore, the change of the GPS signal phase and amplitude imposed by ionospheric irregularities degrades the PPP solution. It is interesting to note that the PPP/if is sensitive, but not too much, to the ionospheric scintillations. In case of PPP/uqrg, it is hard to see the impact because of the high standard deviation in the PPP solution at other epochs. However, the impact of the scintillations is very evident in PPP/tec. This mainly happens because the estimated TEC was set to be very precise during the PPP, so that TEC was included with small values for standard deviation in the PPP Kalman filter. At epochs where only the first-order ionospheric delay is supposed to affect the GPS observations, the PPP/tec solution is very accurate. At epochs where the high-orders terms of the ionosphere delay impact the GPS signal, the PPP degradation becomes evident.

5. Conclusions

The ionospheric conditions are affected by electrodynamic processes that are driven by solar phenomena. During quiet geomagnetic periods, the effects are clearly associated with the seasonal variation of the solar illumination and with the 11-year solar radiation variation. These conditions can be strongly disturbed under the impact of CMEs (coronal mass ejections) and HSS (high-speed streams) in the magnetosphere producing the geomagnetic storms, which result in steeper electron density gradients and stronger irregularities. These irregularities are responsible for fluctuations in the amplitude and phase of GNSS signals, which can degrade the accuracy of the measurements. Therefore, the climatology of these irregularities is very important to define its spatial distribution and time of occurrence.

The investigation of ionospheric scintillations over South America has shown that they can occur at all longitudinal sectors during quiet geomagnetic periods, but they are stronger at post-sunset hours in the crest regions of the EIA (equatorial ionospheric anomaly), and seems to be more intense in the southern EIA crest, which is under the effect of the SAMA (South American Magnetic Anomaly) [24, 37, 81]. The scintillation occurrences strongly enhance with the increase of the solar activity [20, 21, 35, 37, 99], and during geomagnetic disturbed periods [13, 38, 75, 93, 94].

It was presented the potentiality of a new procedure for TEC calibration, showing a useful tool to correct the first-order ionospheric delay that improves the traditional single-frequency PPP solutions. Additionally, the results show a high-sensitive solution of PPP/tec to the ionospheric scintillations, even more sensitive in comparison with the impact of the ionospheric scintillation in the TEC level, which indicates that this kind of procedures are emerging as having potential for a wide range of applications for those measuring and predicting the ionospheric scintillations.

Acknowledgements

EC thanks the National Council for Research and Development (CNPq) for individual research support (processes nos. 556872/2009-6, 406690/2013-8, 303299/2016-9) and the National Institute for Space Research (INPE/MCTI). MTAHM thanks the support from CNPq through grant no. 429885/2016-4. FSP and POC are grateful to CNPq (grant no. 309924/2013-8), Fundação de Amparo à Pesquisa do Estado de São Paulo (FAPESP grant no. 2015/15027-7) and to Faculdade de Ciências e Tecnologia of UNESP (FCT/UNESP).

Conflict of interest

The authors declare that they have no conflict of interest.

Author details

Emília Correia[1,2]*, Marcio Tadeu de Assis Honorato Muella[3], Lucilla Alfonsi[4],
Fabricio dos Santos Prol[5] and Paulo de Oliveira Camargo[5]

*Address all correspondence to: ecorreia@craam.mackenzie.br

1 National Institute for Space Research - INPE, São José dos Campos, Brazil

2 CRAAM-Presbiterian Mackenzie University, São Paulo, Brazil

3 University of Vale do Paraíba - UNIVAP, São José dos Campos, Brazil

4 National Institute of Geophysics and Vulcanology - INGV, Rome, Italy

5 Universidade Estadual Paulista-UNESP, Presidente Prudente, Brazil

References

[1] Prolss GW. Ionospheric F-region storms. In: Volland H, editor. Handbook of Atmospheric Electrodynamics. Florida: CRC Press; 1995. pp. 195-248

[2] Prolss GW. Ionospheric storms at mid-latitude: A short review. In: Kintner PM Jr, Coster AJ, Fuller-Rowell T, Mannucci AJ, Mendillo M, Heelis R, editors. Midlatitude Ionospheric Dynamics and Disturbances, Geophysical Monograph Series. Vol. 181. Washington, D.C: AGU; 2008. pp. 9-24. DOI: 10.1029/181GM03

[3] Buonsanto MJ. Ionospheric storms – A review. Space Science Reviews. 1999;**88**:563-601. DOI: 10.1023/A:1005107532631

[4] Danilov AD, Lastovicka J. Effects of geomagnetic storms on the ionosphere and atmosphere. International Journal of Geomagnetism and Aeronomy. 2001;**2**(3):209-224

[5] Tsurutani B, Mannucci A, Iijima B, Abdu MA, Sobral JHA, Gonzalez W, Guarnieri F, Tsuda T, Saito A, Yumoto K, Fejer B, Fuller-Rowell TJ, Kozyra J, Foster JC, Coster A, Vasyliunas VM. Global dayside ionospheric uplift and enhancement associated with interplanetary electric fields. Journal of Geophysical Research-Space. 2004;**109**:A08302. DOI: 10.1029/2003JA010342

[6] Yizengaw E, Dyson PL, Essex EA, Moldwin MB. Ionosphere dynamics over the southern hemisphere during the 31 march 2001 severe magnetic storm using multi instrument measurement data. Annales Geophysicae. 2005;**23**:707-721. DOI: 10.5194/angeo-23-707-2005

[7] Mendillo M. Storms in the ionosphere: Patterns and processes for total electron content. Reviews of Geophysics. 2006;**44**:RG4001. DOI: 10.1029/2005RG000193

[8] de Franceschi G, Alfonsi L, Romano V, Aquino MHO, Dodson A, Mitchell CN, Wernik AW. Dynamics of high latitude patches and associated small scale irregularities. Journal of Atmospheric and Solar - Terrestrial Physics. 2008;**70**:879-888. DOI: 10.1016/j.jastp.2007.05.018

[9] Danilov AD. Ionospheric F-region response to geomagnetic disturbances. Advances in Space Research. 2013;**52**:343-366. DOI: 10.1016/j.asr.2013.04.019

[10] Thomas EG, Baker JBH, Ruohoniemi JM, Clausen LBN, Coster AJ, Foster JC, Erickson PJ. Direct observations of the role of convection electric field in the formation of a polar tongue of ionization from storm enhanced density. Journal of Geophysical Research-Space. 2013;**118**:1180-1189. DOI: 10.1002/jgra.50116

[11] Horvath I, Lovell BC. Storm-enhanced plasma density and polar tongue of ionization development during the 15 May 2005 super storm. Journal of Geophysical Research-Space. 2015;**120**:5101-5116. DOI: 10.1002/2014JA020980

[12] Prikryl P, Ghoddousi-Fard R, Weygand JM, Viljanen A, Connors M, Danskin DW, Jayachandran PT, Jacobsen KS, Andalsvik YL, Thomas EG, Ruohoniemi JM, Durgonics T, Oksavik K, Zhang Y, Spanswick E, Aquino M, Sreeja V. GPS phase scintillation at high latitudes during the geomagnetic storm of 17-18 March 2015. Journal of Geophysical Research-Space. 2016;**121**:10448-10465. DOI: 10.1002/2016JA023171

[13] Correia E, Spogli L, Alfonsi L, Cesaroni C, Gulisano AM, Thomas EG, Ramirez RFH, Rodel AA. Ionospheric F-region response to the 26 September 2011 geomagnetic storm in the Antarctica American and Australian sectors. Annales Geophysicae. 2017;**35**:1113-1129. DOI: 10.5194/angeo-35-1113-2017

[14] Conker RS, El-Arini B, Hegarty CJ, Hsiao T. Modeling the effects of ionospheric scintillation on GPS/satellite-based augmentation system availability. Radio Science. 2003;**38**(1). DOI: 1001. DOI: 10.1029/2000RS002604

[15] Xu R, Liu Z, Li M, Morton Y, Chen W. An analysis of low latitude ionospheric scintillation and its effects on precise point positioning. Journal of Global Positioning Systems. 2012;**11**:22-32. DOI: 10.5081/jgps.11.1.22

[16] Marques HAS, Monico JFG, Marques HA. Performance of the L2C civil GPS signal under various ionospheric scintillation effects. GPS Solutions. 2016;**20**:139-149. DOI: 10.1007/s10291-015-0472-2

[17] Aquino M, Andreotti M, Dodson AH, Strangeways H. On the use of ionospheric scintillation indices as input to receiver tracking models. Advances in Space Research. 2007;**40**:426-435. DOI: 10.1016/j.asr.2007.05.035

[18] Kintner PM, Ledvina BM, de Paula ER. GPS and ionospheric scintillations. Space Weather. 2007;**5**:S09003. DOI: 10.1029/2006SW000260

[19] Spogli L, Alfonsi L, De Franceschi G, Romano V, Aquino MHO, Dodson A. Climatology of GPS ionospheric scintillations over high and mid-latitude European regions. Annales Geophysicae. 2009;**27**:3429-3437. DOI: 10.5194/angeo-27-3429-2009

[20] Aarons J. Global morphology of ionospheric scintillation. Proceedings of the IEEE. 1982;**70**:360-378. DOI: 10.1109/PROC.1982.12314

[21] Sobral JHA, Abdu MA, Takahashi H, Taylor MJ, de Paula ER, Zamlutti CJ, Aquino MG, Borba GL. Ionospheric plasma bubble climatology over Brazil based on 22 years (1977-1998) of 630 nm airglow observations. Journal of Atmospheric and Terrestrial Physics. 2002;**64**:1517-1524. DOI: 10.1016/S1364-6826(02)00089-5

[22] Abdu MA, Kherani EA, Batista IS, de Paula ER, Fritts DC, Sobral JHA. Gravity wave initiation of equatorial spread F/plasma bubble irregularities based on observational data from the Spread FEx campaign. Annales Geophysicae. 2009;**27**:2607-2622. DOI: 10.5194/angeo-27-2607-2009

[23] Cabrera MA, Pezzopane M, Zuccheretti E, Ezquer RG. Satellite traces, range spread-F occurrence, and gravity wave propagation at the southern anomaly crest. Annales Geophysicae. 2010;**28**:1133-1140. DOI: 10.5194/angeo-28-1133-2010

[24] Spogli L, Alfonsi L, Cilliers PJ, Correia E, De Franceschi G, Mitchell CN, Romano V, Kinrade J, Cabrera MA. GPS scintillations and total electron content climatology in the southern low, middle and high latitude region. Annals of Geophysics. 2013;**56**:R0220. DOI: 10.4401/ag-6240

[25] Li G, Ning B, Ren Z, Hu L. Statistics of GPS ionospheric scintillation and irregularities over polar regions at solar minimum. GPS Solutions. 2010;**14**:331-341. DOI: 10.1007/s10291-009-0156-x

[26] Alfonsi L, Spogli L, De Franceschi G, Romano V, Aquino M, Dodson A, Mitchell CN. Bipolar climatology of GPS ionospheric scintillation at solar minimum. Radio Science. 2011;**46**. DOI: RS0D05.DOI: 10.1029/2010RS004571

[27] Chatterjee S, Chakraborty SK. Variability of ionospheric scintillation near the equatorial anomaly crest of the Indian zone. Annales Geophysicae. 2013;**31**:697-711. DOI: 10.5194/angeo-31-697-2013

[28] Bhattacharyya A, Kakad B, Sripathi S, Jeeva K, Nair KU. Development of intermediate scale structure near the peak of the F region within an equatorial plasma bubble. Journal of Geophysical Research. 2014;**119**:3066-3076. DOI: 10.1002/2013JA019619

[29] Akala AO, Amaeshi LLN, Somoye EO, Idolor RO, Okoro E, Doherty PH, Groves KM, Carrano CS, BridgwoodC T, Baki P, D'ujanga FM, Seemala GK. Climatology of GPS amplitude scintillations over equatorial Africa during the minimum and ascending phases of solar cycle 24. Astrophys Space Science. 2015;**357**:17. DOI: 10.1007/s10509-015-2292-9

[30] Cesaroni C, Spogli L, Alfonsi L, de Franceschi G, Ciraolo L, JFG M, Scotto C, Romano V, Aquino M, Bougard B. L-band scintillations and calibrated total electron content gradients over Brazil during the last solar maximum. Journal Space Weather and Space Climate. 2015;**5**:A36. DOI: 10.1051/swsc/2015038

[31] Zhang H, Liu Y, Wu J, Xu T, Sheng D. Observations and modeling of UHF-band scintillation occurrence probability over the low-latitude region of China during the maximum activity of solar cycle 24. Annales Geophysicae. 2015;**33**:93-100. DOI: 10.5194/angeo-33-93-2015

[32] Srinivasu VKD, Brahmanandam PS, Uma G, Prasad DSVVD, Rao PVSR, Mukherjee S. Long-term morphological and power spectral studies of VHF amplitude scintillations recorded over Waltair (17.7_ N, 83.3_ E), India. Terrestrial, Atmospheric and Oceanic Sciences. 2016;**28**:385-394. DOI: 10.3319/TAO.2016.11.08.01

[33] Moraes AO, Costa E, Abdu MA, Rodrigues FS, de Paula ER, Oliveira K, Perrela WJ. The variability of low-latitude ionospheric amplitude and phase scintillation detected by a triple-frequency GPS receiver. Radio Science. 2017;**52**:439-460. DOI: 10.1002/2016RS006165

[34] Muella MTAH, de Paula ER, Monteiro AA. Ionospheric scintillation and dynamics of Fresnel-scale irregularities in the inner region of the equatorial ionization anomaly. Surveys in Geophysics. 2013;**34**:233-251. DOI: 10.1007/s10712-012-9212-0

[35] Muella MTAH, de Paula ER, Jonah OF. GPS L1-frequency observations of equatorial scintillations and irregularity zonal velocities. Surveys in Geophysics. 2014;**35**:335-357. DOI: 10.1007/s10712-013-9252-0

[36] Marques HA, Marques HAS, Aquino M, Sreeja VV, Monico JFG. Accuracy assessment of precise point positioning with multi-constellation GNSS data under ionospheric scintillation effects. Journal of Space Weather and Space Climatology. 2018;**8**:A15. DOI: 10.1051/swsc/2017043

[37] Muella MTAH, Duarte-Silva MH, Moraes AO, de Paula ER, de Rezende LFC, Alfonsi L, Affonso BJ. Climatology and modeling of ionospheric scintillations and irregularity zonal drifts at the equatorial anomaly crest region. Annales Geophysicae. 2017;**35**:1201-1218. DOI: 10.5194/angeo-35-1201-2017

[38] de Paula ER, Kherani EA, Abdu MA, Batista IS, SobralJ HA, Kantor IJ, Takahashi H, Rezende LFC, Muella MTAH, Rodrigues FS, Kintner PM, LedvinaB M, Mitchell C, Groves KM. Characteristics of the ionospheric irregularities over Brazilian longitudinal sector. Indian Journal of Radio & Space Physics. 2007;**36**:268-277

[39] Akala AO, Doherty PH, Valladares CE, Carrano CS, Sheehan R. Statistics of GPS scintillations over South America at three levels of solar activity. Radio Science. 2011;**46**:RS5018. DOI: 10.1029/2011RS004678

[40] Spogli L, Alfonsi L, Romano V, Franceschi GD, Monico JFG, Shimabukuro MH, Bourgard B, Aquino M. Assessing the GNSS scintillation climate over Brazil under increasing solar activity. Journal of Atmospheric and Terrestrial Physics. 2013;**105**:199-206. DOI: 10.1016/j.jastp.2013.10.003

[41] Forbes JM, Bruinsma SL, Zhang X, Oberheide J. Surface-exosphere coupling due to thermal tides. Geophysical Research Letters. 2009;**36**:L15812. DOI: 10.1029/2009GL038748

[42] Fuller-Rowell TJ, Codrescu MV, Moffett RJ, Quegan S. Response of the thermosphere and ionosphere to geomagnetic storms. Journal of Geophysical Research. 1994;**99**(A3):3893-3914. DOI: 10.1029/93JA02015

[43] Richmond AD. The ionospheric wind dynamo: Effects of its coupling with different atmospheric regions, in the upper mesosphere and lower thermosphere: A review of experiment and theory. In: Johnson RM, Killeen TL, editors. Geophysical Monograph Series. Vol. 87. Washington, D.C: AGU; 1995. pp. 49-65. DOI: 10.1029/GM087p0049

[44] Heelis RA. Electrodynamics in the low and middle latitude ionosphere: A tutorial. Journal of Atmospheric and Solar - Terrestrial Physics. 2004;**66**:825-838. DOI: 10.1016/j.jastp.2004.01.034

[45] Fejer BG. Low latitude ionospheric electrodynamics. Space Science Reviews. 2011;**158**: 145-166. DOI: 10.1007/s11214-010-9690-7

[46] Richmond AD. Ionospheric electrodynamics. In: Volland H, editor. Handbook of Atmospheric Electrodynamics. Florida: CRC Press; 1995. pp. 249-290

[47] Fejer BG. The electrodynamics of the low-latitude ionosphere: Recent results and future challenges. Journal of Atmospheric and Solar - Terrestrial Physics. 1997;**59**:1465-1482. DOI: 10.1016/S1364-6826(96)00149-6

[48] Namba S, Maeda K-I. Radio Wave Propagation. Vol. 86. Tokyo: Corona; 1939

[49] Pancheva D, Apostolov E, Lastovicka J, Boska J. Long-period fluctuations of meteorological origin observed in the lower ionosphere. Journal of Atmospheric and Solar - Terrestrial Physics. 1989;**51**:381-388. DOI: 10.1016/0021-9169(89)90120-7

[50] Chen P-R. Two-day oscillation of the equatorial ionization anomaly. Journal of Geophysical Research. 1992;**97**(A5):6343-6357. DOI: 10.1029/91JA02445

[51] Forbes JM, Leveroni S. Quasi 16-day oscillation in the ionosphere. Geophysical Research Letters. 1992;**19**(10):981-984. DOI: 10.1029/92GL00399

[52] Parish HF, Forbes JM, Kamalabadi F. Planetary wave and solar emission signatures in the equatorial electrojet. Journal of Geophysical Research. 1994;**99**(A1):355-368. DOI: 10.1029/93JA02096

[53] Lastovicka J, Ebel A, Ondraskova A. On the transformation of planetary waves of tropospheric origin into waves in radio wave absorption in the lower ionosphere. Studia Geophysica et Geodaetica. 1994;**38**:71-81. DOI: 10.1007/BF02296254

[54] Immel TJ, Mende SB, Hagan ME, KintnerP M, England SL. Evidence of tropospheric effects on the ionosphere. Eos. 2009;**90**:69-80. DOI: 10.1029/2009EO090001

[55] Correia E, Raulin J-P, Kaufmann P, Bertoni F, Quevedo MT. Inter-hemispheric analysis of daytime low ionosphere behavior from 2007 to 2011. Journal of Atmospheric and Solar - Terrestrial Physics. 2013;**92**:51-58. DOI: 10.1016/j.jastp.2012.09.006

[56] Woodman RF, La Hoz C. Radar observations of F-region equatorial irregularities. Journal of Geophysical Research. 1976;**81**:5447-5466. DOI: 10.1029/JA081i031p05447

[57] Woodman R. Vertical drift velocities and east-west electric fields at the magnetic equator. Journal of Geophysical Research. 1970;**75**(31):6249-6259. DOI: 10.1029/JA075i031p06249

[58] Fejer BG. Low latitude electrodynamics plasma drifts: A review. Journal of Atmospheric and Solar - Terrestrial Physics. 1991;**53**:677-693. DOI: 10.1016/0021-9169(91)90121-M

[59] Kelley MC. The Earth's Ionosphere. London: Academic Press; 1989. p. 580

[60] Abdu MA, de Medeiros RT, Sobral JHA, Bittencourt JA. Spread F plasma bubble vertical rise velocities determined from spaced ionosonde observations. Journal of Geophysical Research. 1983;**88**:9197-9204. DOI: 10.1029/JA088iA11p09197

[61] Valladares CE, Villalobos J, Sheehan R, Hagan MP. Latitudinal extension of low-latitude scintillations measured with a network of GPS receivers. Annales Geophysicae. 2004;**22**:3155-3175. DOI: 10.5194/angeo-22-3155-2004

[62] Gwal AK, Dubey S, Wahi R. A study of L-band scintillations at equatorial latitudes. Advances in Space Research. 2004;**34**:2092-2095. DOI: 10.1016/j.asr.2004.08.005

[63] Abdu MA, Sobral JHA, BastitaI S, Rios VH, Medina C. Equatorial spread-F occurrence statistics in the American longitudes: Diurnal, seasonal and solar cycle variations. Advances in Space Research. 1998;**22**:851-854. DOI: 10.1016/S0273-1177(98)00111-2

[64] Abdu MA, SobralJ HA, BatistaI S. Equatorial spread-F statistics in the American longitudes: Some problems relevant to ESF description in the IRI scheme. Advances in Space Research. 2000;**25**:113-124. DOI: 10.1016/S0273-1177(99)00907-2

[65] Sastri JH. Equatorial electric fields of the disturbance dynamo origin. Annales Geophysicae. 1988;**6**:635-642

[66] Tsurutani BT, Verkhoglyadova OP, Mannucci AJ, Saito A, Araki T, Yumoto K, Tsuda T, Abdu MA, Sobral JHA, Gonzalez WD, McCreadie H, Lakhina GS, Vasyliunas VM. Prompt penetration electric fields (PPEFs) and their ionospheric effects during the

great magnetic storm of 30-31 October 2003. Journal of Geophysical Research-Space. 2008;**113**:A05311. DOI: 10.1029/2007JA012879

[67] Huang C-S, Foster JC, Kelley MC. Long duration penetration of the interplanetary electric field to the low-latitude ionosphere during the main phase of magnetic storms. Journal of Geophysical Research-Space. 2005;**110**:A11309. DOI: 10.1029/2005JA011202

[68] Mannucci AJ, Tsurutani BT, Abdu MA, Gonzalez WD, Komjathy A, Echer E, Iijima BA, Crowley G, Anderson D. Superposed epoch analysis of the dayside ionospheric response to four intense geomagnetic storms. Journal of Geophysical Research-Space. 2008;**113**:A00A02. DOI: 10.1029/2007JA012732

[69] Gonzalez WD, Joselyn JA, Kamide Y, Kroehl HW, Rostoker G, Tsurutani BT, Vasyliunas VM. What is a geomagnetic storm? Journal of Geophysical Research-Space. 1994;**99**:5771-5792. DOI: 10.1029/93JA02867

[70] Yeh KC, Liu CH. Radio-wave scintillations in the ionosphere. Proceedings of IEEE. 1982;**70**:324-360. DOI: 10.1109/PROC.1982.12313

[71] Van Dierendonck AJ, Klobuchar J, Hua Q. Ionospheric scintillation monitoring using commercial single frequency C/A code receivers. In: Proceedings of the Sixth International Technical Meeting of the Satellite Division of the Institute of Navigation (ION GPS-93); 22-24 September 1993. Salt Lake City: ION GPS; 1993. pp. 1333-1342

[72] Basu S, Groves KM. Specification and forecasting of outages on satellite communication and navigation systems. Space Weather, Geophysical Monograph, American Geophysical Union, Washington, DC. 2001;**125**:424-430. DOI: 10.1029/GM125p0423

[73] Abdu MA, Bittencourt JA, Batista IS. Magnetic declination of the equatorial F-region dynamo electric field development and spread F. Journal of Geophysical Research. 1981;**86**(467):11443-11446. DOI: 10.1029/JA086iA13p11443

[74] Batista I, Abdu M, Bittencourt J. Equatorial F region vertical plasma drifts: Seasonal and longitudinal asymmetries in the American sector. Journal of Geophysical Research-Space. 1986;**91**:12055-12064. DOI: 10.1029/JA091iA11p12055

[75] Abdu MA, Batista IS, Carrasco AJ, Brum CGM. South Atlantic magnetic anomaly ionization: A review and a new focus on electrodynamic effects in the equatorial ionosphere. Journal of Atmospheric and Solar - Terrestrial Physics. 2005;**67**:1643-1657. DOI: 10.1016/j.jastp.2005.01.014

[76] Valladares CE, Chau JL. The low-latitude ionosphere sensor network: Initial results. Radio Science. 2012;**47**:RS0L17. DOI: 10.1029/2011RS004978

[77] Vani BC, Shimaburo MH, Monico JFG. Visual exploration and analysis of ionospheric scintillation monitoring data: The ISMR query tool. Computers and Geosciences. 2016;**104**:125-134. DOI: 10.1016/j.cageo.2016.08.022

[78] Fejer BG, de Paula ER, Gonzalez SA, Woodman RF. Average vertical and zonal F region plasma drifts over Jicamarca. Journal of Geophysical Research. 1991;**96**:13901-13906. DOI: 10.1029/91JA01171

[79] Sousasantos J, de Oliveira Moraes A, Sobral JHA, Muella MTAH, de Paula ER, Paolini RS. Climatology of the scintillation onset over southern Brazil. Annales Geophysicae. 2018;**36**:565-576. DOI: 10.5194/angeo-36-565-2018

[80] Basu S, Kudeki E, Basu S, Valladares CE, Weber EJ, Zengingonul HP, Bhattacharyya S, Sheehan R, Meriwether JW, Biondi MA, Kuenzler H, Espinoza J. Scintillations, plasma drifts, and neutral winds in the equatorial ionosphere after sunset. Journal of Geophysical Research. 1996;**101**:26795-26809. DOI: 10.1029/96JA00760

[81] de Paula ER, Muella MTAH, Sobral JHA, Abdu MA, Batista IS, Beach TL, Groves KM. Magnetic conjugate point observations of kilometer and hundred-meter scale irregularities and zonal drifts. Journal of Geophysical Research. 2010;**115**:A08307. DOI: 10.1029/2010JA015383

[82] Valladares CE, Meriwether JW, Sheehan R, Biondi MA. Correlative study of neutral winds and scintillation drifts measured near the magnetic equator. Journal of Geophysical Research. 2002;**107**. DOI: SIA7. DOI: 10.1029/2001JA000042

[83] Kil H, Kintner PM, de Paula ER, Kantor IJ. Latitudinal variations of scintillation activity and zonal plasma drifts in South America. Radio Science. 2002;**37**:1006. DOI: 10.1029/2001RS002468

[84] Engavale B, Jeeva K, Nair KU, Bhattacharyya A. Solar flux dependence of coherence scales in scintillation patterns produced by ESF irregularities. Annales Geophysicae. 2005;**23**:3261-3266. DOI: 10.5194/angeo-23-3261-2005

[85] Fejer BG, Souza JR, Santos AS, Pereira AEC. Climatology of F region zonal plasma drifts over Jicamarca. Journal of Geophysical Research. 2005;**110**:A12310. DOI: 10.1029/2005JA011324

[86] Sobral JHA, Abdu MA, Pedersen TR, Castilho VM, Arruda DCS, Muella MTAH, Batista IS, Mascarenhas M, de Paula ER, Kintner PM, Kherani EA, Medeiros AF, Buriti RA, Takahashi H, Schuch NJ, Denardini CM, Zamlutti CJ, Pimenta AA, Souza JR, Bertoni FCP. Ionospheric zonal velocities at conjugate points over Brazil during the COPEX campaign: Experimental observations and theoretical validations. Journal of Geophysical Research. 2009;**114**:A04309. DOI: 10.1029/2008JA013896

[87] Seaton MJ. A possible explanation of the drop in F-region critical densities accompanying many ionospheric storms. Journal of Atmospheric and Terrestrial Physics. 1956;**8**:122-124. DOI: 10.1016/0021-9169(56)90102-7

[88] Prolss GW, Jung MJ. Travelling atmospheric disturbances as a possible explanation for daytime positive storm effects of moderate duration at middle latitudes. Journal of Atmospheric and Terrestrial Physics. 1978;**40**:1351-1354. DOI: 10.1016/0021-9169(78)90088-0

[89] Foster JC. Ionospheric-magnetospheric-heliospheric coupling: Storm-time thermal plasma redistribution. In: Kintner PM, Coster AJ, Fuller-Rowell T, Mannucci AJ, Mendillo M, Heelis R, editors. Mid-Latitude Dynamics and Disturbances. Geophysical Monograph Series. Vol. 181. 2008. pp. 121-134. DOI: 10.1029/181GM12

[90] Sandel BR, King RA, Forrester WT, Gallagher DL, Broadfoot AL, Curtis CC. Initial results from the IMAGE extreme ultraviolet imager. Geophysical Research Letters. 2001;**28**:1439-1442. DOI: 10.1029/2001GL012885

[91] Skone S, Man F, Ghafoori F, Tiwari R. Investigation of scintillation characteristics for high latitude phenomena. Proceedings of the ION GNSS 2008. 2008;**SessionD5**:2425-2434

[92] Kinrade J, Mitchell CN, Smith ND, Ebihara Y, Weatherwax AT, Bust GS. GPS phase scintillation associated with optical auroral emissions: First statistical results from the geographic south pole. Journal of Geophysical Research-Space. 2013;**118**:2490-2502. DOI: 10.1002/jgra.50214

[93] de Abreu AJ, Fagundes PR, Gende M, Bolaji OS, de Jesus R, Brunini C. Investigation of ionospheric response to two moderate geomagnetic storms using GPS–TEC measurements in the south American and African sectors during the ascending phase of solar cycle 24. Advances in Space Research. 2014;**53**:1313-1328. DOI: 10.1016/j.asr.2014.02.011

[94] de Abreu AJ, Martin IM, Fagundes PR, Venkatesh K, Batista IS, de Jesus R, Rockenback M, Coster A, Gende M, Alves MA, Wild M. Ionospheric F-region observations over American sector during an intense space weather event using multi-instruments. Journal of Atmospheric and Solar - Terrestrial Physics. 2017;**156**:1-14. DOI: 10.1016/j.jastp.2017.02.009

[95] Prol FS, Camargo PO, Monico JFG, Muella MTAH. Assessment of a TEC calibration procedure by single frequency PPP. GPS Solutions. 2018;**22**:35. DOI: 10.1007/s10291-018-0701-6

[96] Ø-vstedal O. Absolute positioning with single-frequency GPS receivers. GPS Solutions. 2002;**5**:33-44

[97] Le AQ, Tiberius C. Single-frequency precise point positioning with optimal filtering. GPS Solutions. 2007;**11**:61-69

[98] Sterle O, Stopar B, Prešeren PP. Single-frequency precise point positioning: An analytical approach. Journal of Geodesy. 2015;**89**:793-810

[99] Sreeja VV, Aquino M, Forte B, Elmas Z, Hancock C, de Franceschi G, Alfonsi L, Spogli L, Romano V, Bougard B, Monico JFG, Wernik AW, Sleewaegen J-M, Canto A, da Silva EF. Tackling ionospheric scintillation threat to GNSS in Latin America. Journal of Space Weather and Space Climate. 2011;**1**:A05. DOI: 10.1051/swsc/2011005

Section 4

Present Day Accuracy of GNSS Point Positioning

Chapter 5

Evaluation of GNSS Data with Internet Based Services: The Case of HRUH Station

Mustafa Ulukavak

Additional information is available at the end of the chapter

http://dx.doi.org/10.5772/intechopen.79064

Abstract

Nowadays, as the Internet services are developed, it becomes possible to offer services for many applications in the engineering field online via the Internet. One of these services is the evaluation of online GPS data. The most important feature of Internet-based applications is that these services are free and easy to use. In this study, the data of Global Navigation Satellite Systems (GNSS) of different periods belonging to newly established HRUH permanent GNSS station in Harran University were evaluated through Internet-based services. The evaluation strategy of GNSS data was conducted in 1-, 2-, 6-, 12-, and 24-h campaigns, and the results were compared between different Internet site solution results. When the results obtained are examined, it can be said that the accuracy of the data obtained from these services can be used in many applications requiring precision in centimeter levels and is capable of satisfying the expectancies.

Keywords: PPP, GNSS, RINEX, internet-based GNSS evaluation services, positioning accuracy

1. Introduction

Recently, web-based GNSS positioning services have begun to be developed as an additional option to classical evaluation methods. Such services produce solutions automatically by using some of the GNSSS observations loaded via the web interface over the Internet. GNSS observations collected in the field are recorded in standard data formats such as Receiver INdependent EXchange (RINEX) and then uploaded to web-based positioning services, allowing location coordinates of observation points to be obtained in short time and free of charge [1–3].

Web-based positioning services have been considered as an alternative to scientific or commercial software for 15 years. Wherever the Internet access is available, it is easier to evaluate RINEX data using such services. Another reliable aspect of preferring web-based GNSS software is the use of reliable scientific software (Bernese, Gamit, GIPSY/OASIS II, etc.) running in the background of these systems. These services also provide many advantages to the user by reducing the cost of many software, hardware, tools, personnel and transportation services. The results of evaluations of GNSS observations uploaded to these services also provide many advantages such as the possibility of downloading results from the web interface or sending the results to the users via e-mail. The results from these services are in the form of a summary or detailed report. The standard deviation values of these points are sent together with the estimated point coordinates in the incoming reports. Some services send out summary reports in the form of short summary information, while some services provide detailed reports with detailed and graphical presentations. Many of these services are free and some of them require free membership for accessing with a user name and password while using. In general, these services use the data and products of the high accurate and precise International GNSS Service (IGS). IGS provides these products with high precision of GPS/GLONASS ephemeris, satellite and station clocks, earth orientation parameters (ERP), IGS stations coordinates and velocities, and atmospheric parameters to users. These services provided by IGS have led to the emergence of new approaches and new evaluation methods in positioning with the accuracy increase in data processing, orbit determination, and acquisition of clock information in satellite geodesy [4].

Web-based positioning services have introduced two different types of solutions. The first is the relative positioning approach and the second is the precise point positioning (PPP) solution approach. In this study, web-based precise point positioning solution will be mentioned. The services that are mainly used for the PPP solution approach use only GPS or GPS + GLONASS products such as orbits and clock corrections. The data flow for both web-based positioning services is shown in **Figure 1**.

In this study, four different web-based PPP services, which are most well known and widely used, general properties of services, accessing addresses and analysis results are examined.

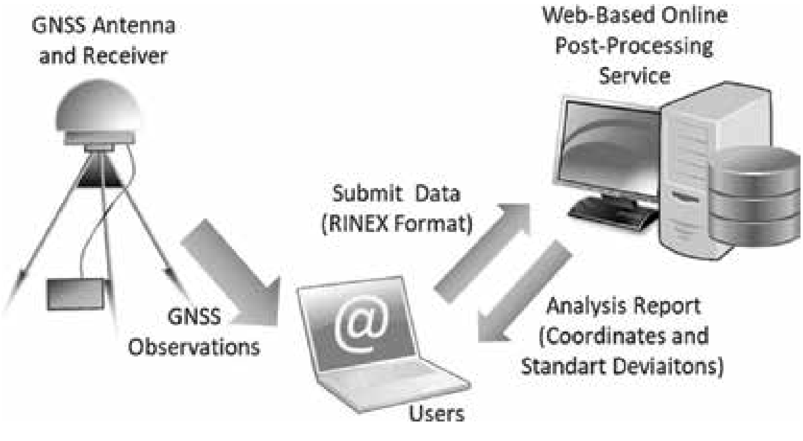

Figure 1. Schematic presentation of web-based positioning services.

1-, 2-, 6-, 12-, and 24-h GNSS observations of the HRUH permanent GNSS station which is established on the roof of the GNSS Laboratory of Harran University Geomatics Engineering Department are evaluated for each web-based positioning service. Then, the same GNSS observations of this station are compared with the analysis results (coordinates and standard deviations) with the scientific GNSS-Inferred Positioning System and Orbit Analysis Simulation Software (GIPSY/OASIS II) developed by NASA's JPL laboratory.

2. Precise point positioning (PPP)

The widespread use of satellite and space techniques has become an indispensable tool in satellite positioning. Nowadays, by using developed techniques and methods, highly accurate position information is obtained with the help of positioning algorithms. These techniques often differ according to the data collection method. Absolute and relative positioning methods from the earliest times of use of positioning systems are the most preferred techniques for application purposes. The relative positioning technique requires at least two receivers to be used by simultaneous GNSS observations. However, PPP is a method that can be applied by removing this necessity. The PPP technique is based on the evaluation of the code and phase measurements collected from a single receiver. In this technique, the receiver position is directly determined by using precise orbits and clock corrections issued by IGS and similar organizations [5, 6]. The success of the positioning with the PPP technique depends largely on the determination of precise orbit changes of GPS satellites. Therefore, in PPP solutions, it is important to obtain precise orbit (ultra-rapid, rapid, and final) and satellite clock information instead of orbital information broadcast from satellites. Accuracy, broadcast latency, update and sample interval for accurate GPS satellite orbits and clock corrections published by IGS are given in **Table 1**.

Nowadays, as the accuracy of precise satellite orbits and clock products published by organizations such as IGS, CODE, and JPL advances, the use of PPP technique is gradually increasing in determining the point positions.

The ionosphere-independent observation equations of pseudorange and carrier phase measurements include receiver location, clock offset, tropospheric delay, carrier phase unknown parameters, and observation errors:

$$\begin{aligned} l_p &= \rho + c(dt - dT) + T_r + I_r + \varepsilon_p \\ l_\varphi &= \rho + c(dt - dT) + N\lambda + T_r + I_r + \varepsilon_\varphi \end{aligned} \tag{1}$$

where l_p and l_φ are the ionosphere-independent combination of the code and phase measurements, respectively; dt is the receiver clock offset which is the difference between receiver time (receiver clock) and system time (GPS); dT is the satellite clock offset which is the difference between satellite time (satellite clock) and system time (GPS); c is the speed of light in space; N is the integer ambiguity of the ionosphere-independent carrier phase; T_r is the tropospheric signal delay, and I_r is the ionospheric signal delay between the satellite and the receiver; λ is

Type		Accuracy	Latency	Updates	Sample interval
Broadcast	Orbits	~100 cm	Real time	---	Daily
	Sat. clocks	~5 ns RMS ~2.5 ns SDev			
Ultra-rapid (predicted)	Orbits	~5 cm	Real time	At 03, 09, 15, 21 UTC	15 min
	Sat. clocks	~3 ns RMS ~1.5 ns SDev			
Ultra-rapid (observed)	Orbits	~3 cm	3–9 h	At 03, 09, 15, 21 UTC	15 min
	Sat. clocks	~150 ps RMS ~50 ps SDev			
Rapid	Orbits	~2.5 cm	17–41 h	At 17 UTC daily	15 min
	Sat. and Stn. clocks	~75 ps RMS ~25 ps SDev			5 min
Final	Orbits	~2.5 cm	12–18 days	Every Thursday	15 min
	Sat. and Stn. clocks	~75 ps RMS ~20 ps SDev			Sat.: 30s Stn.:5 min

Table 1. Accurate GPS satellite orbits and clock corrections issued by IGS.

the wavelength; ε_p and ε_φ are the noise components including the signal reflection [5, 6]. The geometric distance between satellite (X^S, Y^S, Z^S) and receiver (X_R, Y_R, Z_R) is defined as:

$$\rho = \sqrt{(X^S - X_R)^2 + (Y^S - Y_R)^2 + (Z^S - Z_R)^2} \quad (2)$$

PPP technology has different software options such as Bernese, Gamit, GIPSY/OASIS II to determine the position.

3. GNSS measurements processing software

Today, we can classify software that can evaluate GNSS measurements in three different groups. The first of these is commercial software. Commercial software is a software that is bundled with the GNSS set, which is often used in practical engineering applications and is usually purchased by customer companies. These are the more preferred software by institutions and organizations that best determine the solutions offered by the company in order to avoid any problems from the users. Other software that can process GNSS measurements are scientific software. Scientific software has been fully developed at research centers and universities for use in academic and scientific studies. The use of scientific software is more complex than commercial software and web-based data processing services. For this reason, there are

PPP service name	Organizations	Web pages (March, 2018)
CSRS-PPP: Canadian Spatial Reference System- Precise Point Positioning	Natural Resources Canada (NRC)	https://webapp.geod.nrcan.gc.ca/geod/tools-outils/ppp.php?locale=en
GAPS: GPS Analysis and Positioning Software	University of New Brunswick (UNB)	http://gaps.gge.unb.ca/submitadvanced.php
APPS: Automatic Precise Positioning Service	NASA- Jet Propulsion Laboratory (JPL)	http://apps.gdgps.net/apps_file_upload.php
magicGNSS: magic Precise Point Positioning Solution	GMV Aerospace and Defence S.A.U.	https://magicgnss.gmv.com/user/ppp

Table 2. Online services using PPP solution approach.

more training-, information-, and experience-related requirements. In such software, different parameters used in the evaluation can provide a different significance in the results. A third type of software that can process GNSS observations is web-based positioning services. In this service, it is necessary to have only one GNSS receiver and an Internet connection in order to be able to generate the point position information if the observations in the GNSS receiver are aggregated in whatever manner the observations are aggregated in static or kinematic methods. There is no need for any additional financing or equipment other than these equipment. Web-based GNSS services are simple to use and require no additional software knowledge. The data in the RINEX format obtained from the GNSS receivers are processed by uploading them to the web interface of web-based positioning services. Depending on the service to be used, some services require additional information such as the receiving antenna brand and antenna height. At the end of the evaluation process initiated after the uploading process of the GNSS observations, the final report of the relevant GNSS observations is presented to the user via e-mail or a link that can be downloaded from the web interface. The Internet addresses of the web-based positioning services that can process GNSS observations according to the PPP method and provide them to the users are given in **Table 2**.

All of the services mentioned in **Table 2** have limited use. However, they use scientific and academic software in the background to determine the station coordinates. These services present the resultant product using the commonly accepted parameters of the data processing methods for coordinate production from GNSS observations in the literature. The web-based positioning services used in this study are:

3.1. CSRS-PPP: Canadian spatial reference system-precise point positioning

Canadian Spatial Reference System Precise Point Positioning (CSRS-PPP) is a web-based GPS observations processing service provided by the Natural Resources Canada (NRCAN). This service works with a membership system that has the ability to process GNSS observations from single- or dual-frequency receivers based on static or PPP techniques. CSRS-PPP uses precise GPS orbit and clock products provided by the IGS. The solutions of PPP coordinates are represented in both NAD83 and ITRF14 data with detailed graphical analysis reports. This service has actively processed GLONASS data from October 4, 2011 and accepted user-provided ocean tidal loading (OTL) correction files from February 14, 2012.

3.2. GAPS: GPS analysis and positioning software

GPS analysis and positioning software (GAPS) is a web-based processing service for GPS observations provided by the University of New Brunswick (UNB). It is a service that does not require membership registration. This service uses IGS's rapid and final orbit and clock products during the process of GPS observations. GAPS is a service that delivers GNSS solutions to users via e-mail. The coordinate solutions of GAPS are represented in ITRF14 datum.

3.3. APPS: automatic precise positioning service

Automatic precise positioning service (APPS) is a web-based GPS evaluation service operated by NASA Jet Propulsion Laboratory (JPL) and the California Institute of Technology. In the background of this service, the scientific software GIPSY/OASIS II developed in this institution is also run. The system also uses real-time, daily and weekly GPS orbit and clock products produced by JPL. The results of the evaluation can be obtained shortly after the options in the service interface (antenna height, antenna type, e-mail address, etc.) are checked and the GNSS observations are loaded. The solutions of PPP coordinates are represented in ITRF08 datum with detailed analysis reports. APPS is a web-based positioning service that requires membership and offers the use of ftp services for industrial users.

3.4. MagicGNSS: magic precise point positioning solution

Magic Precise Point Positioning Solution is an Internet service created by Spanish GMV Company. MagicGNSS is a positioning service that uses accurate positioning detection technology. The most important advantage of the service is that it can analyze GPS and GLONASS observations together. This system can process both static and kinematic observations. The PPP module of this service uses accurate clock and precise orbit products which are provided by the IGS. The system supports RINEX and all compressed observation formats and offers free 1-GB disk space for member users. The service provides users with a detailed graphical analysis report along with positioning solutions. The solutions of PPP methods are represented in both ETRS89 and ITRF14 data. The service works by downloading or e-mailing the result files from the service's Internet interface.

4. Experimental study

This study provides the accuracy analysis of the web-based online services using PPP solution approaches. For this purpose, HRUH permanent reference station which located on top of the roof of Geomatics Engineering Department's GNSS Laboratory in Harran University

HRUH GNSS station **Observation duration**	*X(m)* $\sigma_X(m)$	*Y(m)* $\sigma_Y(m)$	*Z(m)* $\sigma_Z(m)$
1 h	3,954,667.2472	3,202,680.8771	3,833,020.8337
	0.0460	0.0386	0.0347
2 h	3,954,667.2465	3,202,680.8640	3,833,020.8351
	0.0065	0.0065	0.0060
6 h	3,954,667.2430	3,202,680.8621	3,833,020.8269
	0.0035	0.0031	0.0031
12 h	3,954,667.2426	3,202,680.8609	3,833,020.8263
	0.0025	0.0022	0.0023
24 h	3,954,667.2418	3,202,680.8605	3,833,020.8310
	0.0018	0.0015	0.0016

Table 3. HRUH station hourly coordinates and standard deviations.

was selected for the accuracy analysis. The GPS data segmented into 1-, 2-, 6-, 12-, and 24-h sessions were collected by HRUH station in static mode on April 18, 2018 (DOY 108). The data sampling interval of the GNSS receiver was 30 s. As a result of this study, we have compared the analysis results obtained by using CSRS-PPP, GAPS, APPS, MagicGNSS services, and scientific software (GIPSY/OASIS II) which produce solutions based on PPP technique. All services including GIPSY/OASIS II scientific software (except APPS) use coordinate solutions at ITRF14 datum. In order to be able to compare the analysis results of all services in the same datum, APPS coordinate solutions in ITRF08 datum have been converted to the coordinates of ITRF14 datum with the help of URL [7]. **Table 3** gives the coordinates and standard deviation results in the Cartesian coordinate system according to the 1-, 2-, 6-, 12-, and 24-h GPS observations of the HRUH station with GIPSY/OASIS II scientific software.

The aim of the study was to determine how consistent results from web-based positioning services are. GPS observations for 1-, 2-, 6,- 12-, and 24-h on the same day (DOY 108) belonging to the same station were separated and loaded into each individual web-based positioning system and results were obtained. Apart from the results obtained during the 1-h observation period, the best coordinate precision and accuracy are understood from the results of the APPS service. The consistency between the GIPSY/OASIS II scientific software and the solutions of the GAPS web-based positioning systems is close together. MagicGNSS service provides only the coordinate points, the related standard deviations are not added to the figures. **Figures 2–6** show the results of the coordinates and standard deviation values of the Cartesian coordinate system for 1-, 2-, 6-, 12-, and 24-h GPS observations of the HRUH station produced by the web-based positioning services, respectively.

When the solutions of 1-h GPS observations of the HRUH station in **Figure 2** are examined, the standard deviation values for the CSRS-PPP, GAPS, APPS, and GIPSY/OASIS II coordinate solutions range from 0.01 to 0.1 m. Standard deviation values of the coordinate components

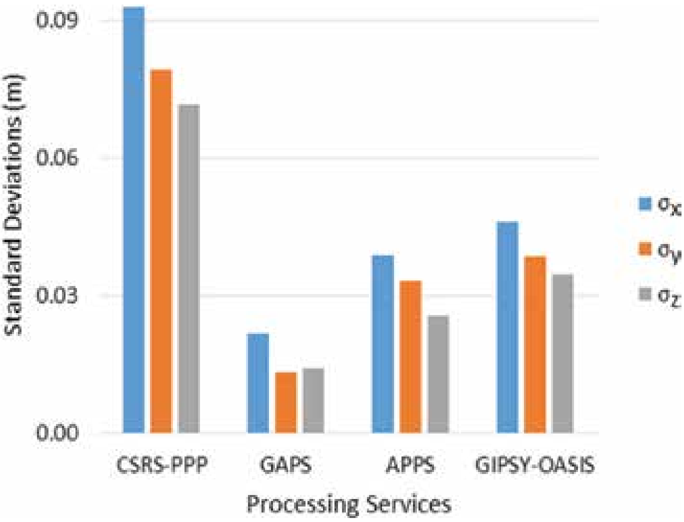

Figure 2. Standard deviations of HRUH station coordinates (1 h).

obtained from the CSRS-PPP service were determined as σ_x = ±0.092 m, σ_y = ±0.079 m, and σ_z = ±0.071 m, respectively. Standard deviation values of the coordinate components obtained from the GAPS service are σ_x = ±0.021 m, σ_y = ±0.033 m, and σ_z = ±0.026 m, respectively, and the standard deviation values of the coordinate components obtained from the APPS service are σ_x = ±0.038 m, σ_y = ±0.033 m, and σ_z = ±0.026 m. Standard deviation values of the coordinate components obtained by GIPSY/OASIS II scientific software are calculated as σ_x = ±0.046 m, σ_y = ±0.038 m, and σ_z = ±0.034 m, respectively.

When the solutions of the 2-h GPS observations of the HRUH station in **Figure 3** are examined, the standard deviation values of the CSRS-PPP, GAPS, APPS, and GIPSY/OASIS II coordinate solutions range from 0.005 to 0.056 m. Standard deviation values of the coordinate components obtained from the CSRS-PPP service were determined as σ_x = ±0.056 m, σ_y = ±0.035 m, and σ_z = ±0.037 m, respectively. Standard deviation values of coordinate components obtained from GAPS service are σ_x = ±0.014 m, σ_y = ±0.006 m, and σ_z = ±0.008 m, respectively and the standard deviation values of coordinate components obtained from APPS service are σ_x = ±0.005 m, σ_y = ±0.005 m, and σ_z = ±0.005 m. Standard deviation values of the coordinate components obtained by GIPSY/OASIS II scientific software were calculated as σ_x = ±0.006 m, σ_y = ±0.006 m, and σ_z = ±0.006 m, respectively.

When the solutions of the 6-h GPS observations of the HRUH station in **Figure 4** are examined, the standard deviation values for the CSRS-PPP, GAPS, APPS, and GIPSY/OASIS II coordinate solutions range from 0.002 to 0.027 m. Standard deviation values of the coordinate components obtained from CSRS-PPP service were determined as σ_x = ±0.027 m, σ_y = ±0.017 m, and σ_z = ±0.018 m, respectively. Standard deviation values of coordinate components obtained from GAPS service are σ_x = ±0.005 m, σ_y = ±0.003 m, and σ_z = ±0.003 m, respectively, and the standard deviation values of coordinate components obtained from APPS service are σ_x = ±0.003 m, σ_y = ±0.003 m, and σ_z = ±0.003 m. Standard deviation values of the coordinate components obtained by GIPSY/OASIS II scientific software were calculated as σ_x = ±0.003 m, σ_y = ±0.003 m, and σ_z = ±0.003 m, respectively.

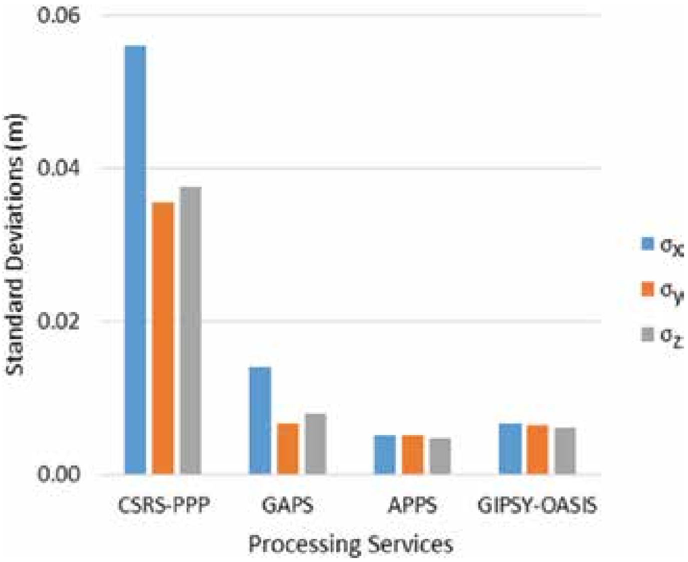

Figure 3. Standard deviations of HRUH station coordinates (2 h).

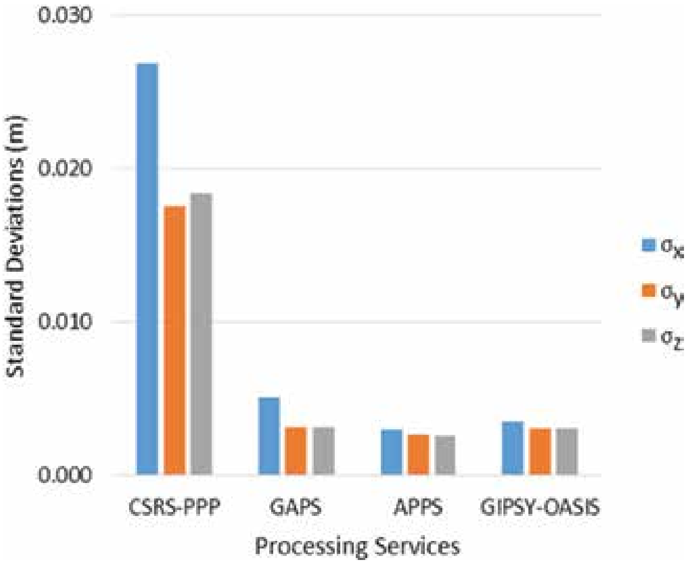

Figure 4. Standard deviations of HRUH station coordinates (6 h).

When the solutions of the 12-h GPS observations of the HRUH station are examined in **Figure 5**, the standard deviation values of the CSRS-PPP, GAPS, APPS, and GIPSY/OASIS II coordinate solutions range from 0.002 to 0.015 m. Standard deviation values of the coordinate components obtained from the CSRS-PPP service were determined as σ_x = ±0.0147 m, σ_y = ±0.0128 m, and σ_z = ±0.0125 m, respectively. Standard deviation values of coordinate components obtained from GAPS service are σ_x = ±0.0026 m, σ_y = ±0.0024 m, and σ_z = ±0.0021 m,

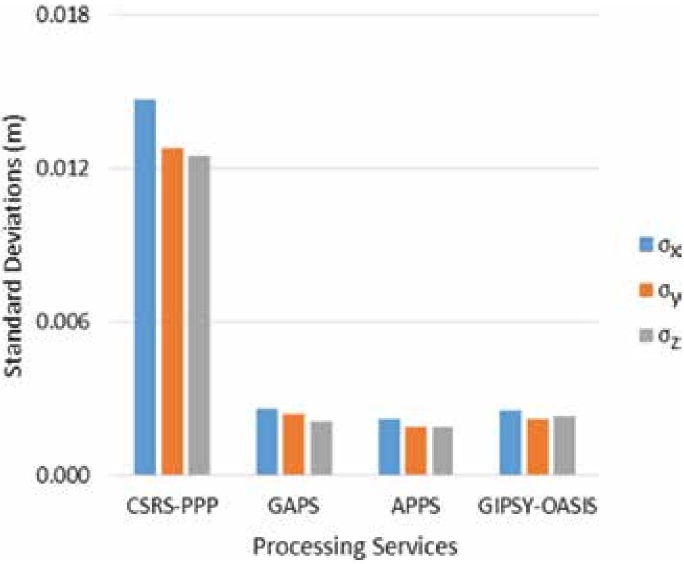

Figure 5. Standard deviations of HRUH station coordinates (12 h).

respectively, and the standard deviation values of coordinate components obtained from APPS service are $\sigma_x = \pm 0.0022$ m, $\sigma_y = \pm 0.0019$ m, and $\sigma_z = \pm 0.0019$ m. Standard deviation values of the coordinate components obtained by GIPSY/OASIS II scientific software are calculated as $\sigma_x = \pm 0.0025$ m, $\sigma_y = \pm 0.0022$ m, and $\sigma_z = \pm 0.0023$ m, respectively.

When the solutions of the 24-h GPS observations of the HRUH station are examined in **Figure 6**, the standard deviation values of the CSRS-PPP, GAPS, APPS, and GIPSY/OASIS II coordinate solutions range from 0.001 to 0.009 m. Standard deviation values of the coordinate components obtained from CSRS-PPP service were determined as $\sigma_x = \pm 0.0096$ m, $\sigma_y = \pm 0.0086$ m, and $\sigma_z = \pm 0.0084$ m, respectively. Standard deviation values of coordinate components obtained from GAPS service are $\sigma_x = \pm 0.0017$ m, $\sigma_y = \pm 0.0015$ m, and $\sigma_z = \pm 0.0015$ m, respectively, and the standard deviation values of coordinate components obtained from APPS service are $\sigma_x = \pm 0.0015$ m, $\sigma_y = \pm 0.0013$ m, and $\sigma_z = \pm 0.0014$ m. Standard deviation values of the coordinate components obtained by GIPSY/OASIS II scientific software are calculated as $\sigma_x = \pm 0.0018$ m, $\sigma_y = \pm 0.0015$ m, and $\sigma_z = \pm 0.0016$ m, respectively.

If the result in **Figures 2–6** will be interpreted graphically, the most sensitive results for the results of different observation periods of each coordinate component evaluated in the web-based positioning services are GAPS service for 1 h observation period; APPS service for 2-, 6-, 12-, and 24-h observation periods. The CSRS-PPP service was at the forefront of all evaluations.

After obtaining the standard deviations of each coordinate component in the Cartesian coordinate system of the web-based positioning services, the obtained coordinates were compared with the coordinates obtained in GIPSY/OASIS II scientific software. The calculated web-based coordinate results were subtracted from the coordinates obtained from GIPSY/OASIS II scientific software and classified according to web-based positioning services and GPS observation times (**Figures 7–10**).

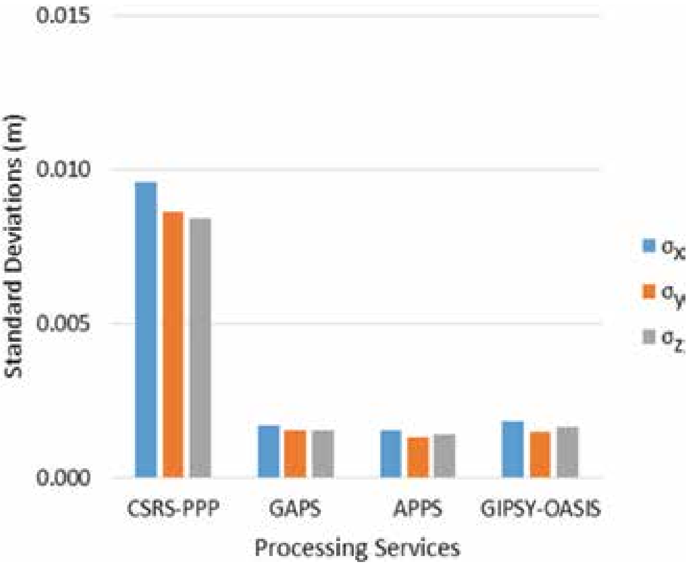

Figure 6. Standard deviations of HRUH station coordinates (24 h).

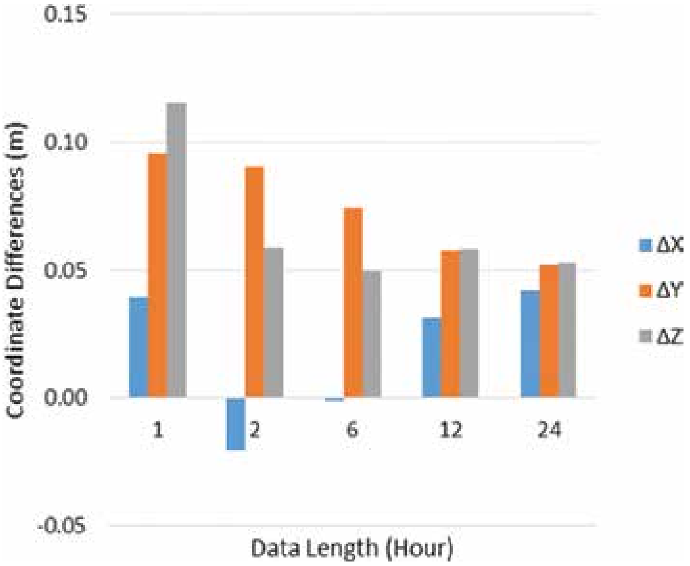

Figure 7. Coordinate differences between CSRS-PPP solution and GIPSY/OASIS II solution.

In **Figure 7**, the differences between the CSRS-PPP web-based positioning service and the coordinate solutions of different GPS observation times obtained by the GIPSY/OASIS II scientific software are calculated. The differences of the coordinate solutions of 1 h GPS observation time are calculated as ΔX = 0.039 m, ΔY = 0.095 m, and ΔZ = 0.115 m. The differences of the coordinate solutions of the 2-h GPS observation time were calculated as ΔX = −0.020 m, ΔY = 0.091 m, and ΔZ = 0.058 m. The differences of the coordinate solutions of the 6-h GPS observation

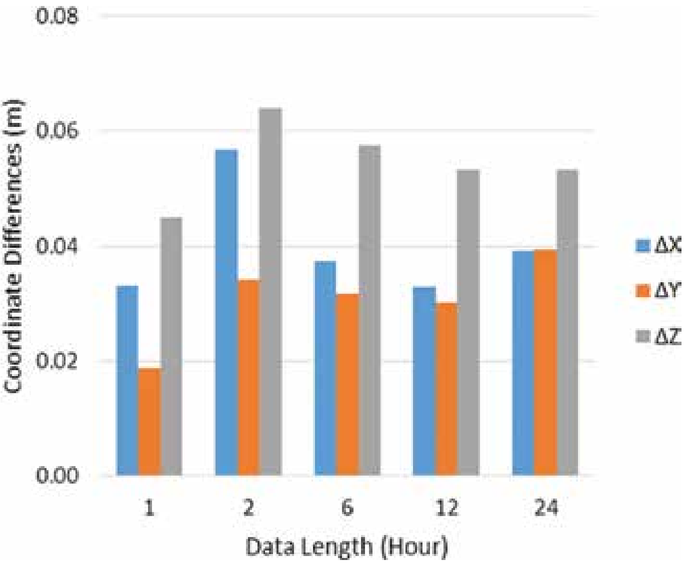

Figure 8. Coordinate differences between GAPS solution and GIPSY/OASIS II solution.

period were calculated as ΔX = –0.001 m, ΔY = 0.074 m, and ΔZ = 0.049 m. The differences of the coordinate solutions of the 12-h GPS observation period were calculated as ΔX = 0.031 m, ΔY = 0.058 m, and ΔZ = 0.058 m. The differences of the coordinate solutions for the 24-h GPS observation period were calculated as ΔX = 0.042 m, ΔY = 0.052 m, and ΔZ = 0.053 m.

In **Figure 8**, the differences between the GAPS web-based positioning service and the coordinate solutions of different GPS observation times obtained by the GIPSY/OASIS II scientific software are calculated. The differences of the coordinate solutions of the 1 h GPS observation period were calculated as ΔX = 0.033 m, ΔY = 0.019 m, and ΔZ = 0.045 m. The differences in coordinate solutions for the 2-h GPS observation period were calculated as ΔX = 0.058 m, ΔY = 0.034 m, and ΔZ = 0.064 m. The differences of the coordinate solutions of the 6-h GPS observation period were calculated as ΔX = 0.037 m, ΔY = 0.032 m, and ΔZ = 0.057 m. The differences of the coordinate solutions of the 12-h GPS observation period were calculated as ΔX = 0.033 m, ΔY = 0.030 m, and ΔZ = 0.053 m. The differences of coordinate solutions for the 24-h GPS observation period were calculated as ΔX = 0.039 m, ΔY = 0.039 m, and ΔZ = 0.053 m.

In **Figure 9**, the differences between the coordinate solutions of different GPS observation times obtained by the APPS web-based positioning service and GIPSY/OASIS II scientific software are calculated. The differences of the coordinate solutions of 1 h GPS observation time are calculated as ΔX = 0.050 m, ΔY = 0.008 m, and ΔZ = 0.039 m. The differences of the coordinate solutions of the 2-h GPS observation period were calculated as ΔX = 0.054 m, ΔY = 0.040 m, and ΔZ = 0.055 m. The differences of the coordinate solutions of the 6-h GPS observation period were calculated as ΔX = 0.052 m, ΔY = 0.042 m, and ΔZ = 0.054 m. The differences of the coordinate solutions for the 12-h GPS observation period were calculated as ΔX = 0.048 m, ΔY = 0.039 m, and ΔZ = 0.052 m. The differences in the coordinate solutions of the 24-h GPS observation period were calculated as ΔX = 0.048 m, ΔY = 0.040 m, and ΔZ = 0.053 m.

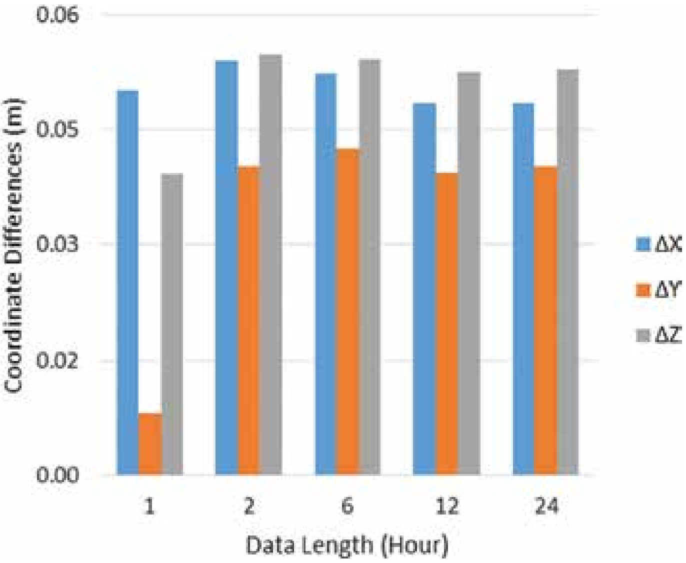

Figure 9. Coordinate differences between APPS solution and GIPSY/OASIS II solution.

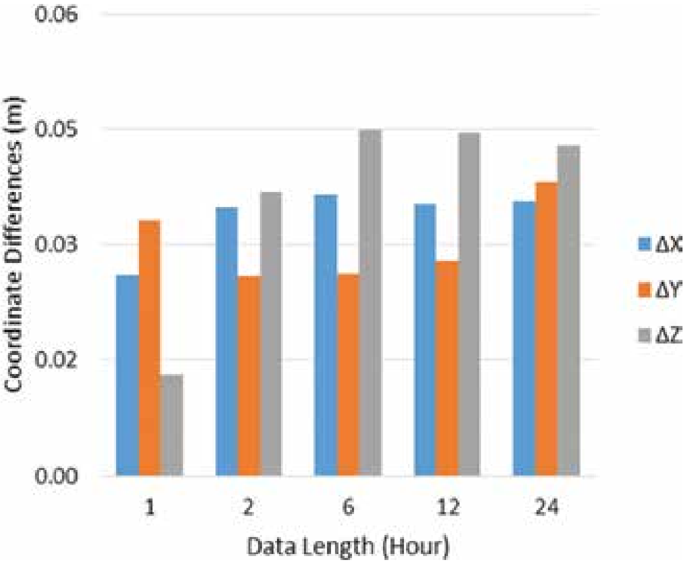

Figure 10. Coordinate differences between MagicGNSS solution and GIPSY/OASIS II solution.

In **Figure 10** the differences between the coordinate solutions of different GPS observation times obtained by the MagicGNSS web-based positioning service and GIPSY-OASIS scientific software are calculated. The differences of the coordinate solutions of 1 h GPS observation time are calculated as ΔX = 0.026 m, ΔY = 0.033 m, and ΔZ = 0.013 m. The differences of coordinate solutions for the 2-h GPS observation time are calculated as ΔX = 0.035 m, ΔY = 0.026 m, and ΔZ = 0.037 m. The differences of the coordinate solutions of the 6-h GPS observation period were calculated as ΔX = 0.036 m, ΔY = 0.026 m, and ΔZ = 0.045 m. The differences in coordinate solutions for the 12-h GPS observation period were calculated as ΔX = 0.035 m, ΔY = 0.028 m, and ΔZ = 0.045 m. The differences of the coordinate solutions of the 24-h GPS observation period were calculated as ΔX = 0.035 m, ΔY = 0.038 m, and ΔZ = 0.043 m.

APPS uses GIPSY/OASIS II in the background. However, the difference in the results between GIPSY/OASIS II and APPS is slightly larger than the difference in results between GIPSY/OASIS II and MagicGNSS. This can be ascribed to the fact that APPS results are based on the ITRF08 but not the ITRF14 on which both GIPSY/OASIS II and MagicGNSS rely.

In **Figures 7–10**, the differences between the coordinate values of the HRUH permanent GNSS station produced by the web-based positioning services for different GPS observation times and the coordinate solutions obtained by the GIPSY/OASIS II scientific software are examined.

In **Figure 7**, when the coordinate solutions obtained from the CSRS-PPP web-based positioning service are compared with the coordinate solutions obtained from the GIPSY/OASIS II scientific software, the coordinate differences between 1- and 2-h observation periods are found to be around 10 cm, coordinate differences for 6- and 12-h observation periods are around 5 cm, and for 24-h observation periods, coordinate differences are less than 5 cm.

In **Figure 8**, when the coordinate solutions obtained from the GAPS web-based positioning service are compared with the coordinate solutions obtained from the GIPSY/OASIS II scientific software, the coordinate differences between 1-h observation period is found to be less than 5 cm, coordinate differences for 2-, 6-, 12-, and 24-h observation periods are around 5 cm.

In **Figure 9**, when the coordinate solutions obtained from the APPS web-based positioning service are compared with the coordinate solutions obtained from the GIPSY/OASIS II scientific software, the coordinate differences between 1-h observation period is found to be less than 5 cm, coordinate differences for 2-, 6-, 12-, and 24-h observation periods are around 5 cm.

In **Figure 10**, when the coordinate solutions obtained from the MagicGNSS web-based positioning service are compared with the coordinate solutions obtained from the GIPSY/OASIS II scientific software, the coordinate differences between 1-, 2-, 6-, 12-, and 24-h observation period is found to be less than 5 cm.

5. Conclusion

Today, PPP technology is becoming increasingly important. With its many advantages, it poses a serious alternative to positioning methods. However, the use of web-based positioning services, which analyze using PPP technology, is becoming widespread. The PPP technique is feasible in the measurement and evaluation process with only one GNSS receiver, and providing these services to the user free of charge on the Internet makes these systems advantageous in many applications. It should not be forgotten that the reliability of the results evaluated according to the PPP technique is directly related to the accuracy of the IGS orbit and clock information.

In such systems, many outcome products can be obtained without the need for GNSS expertise other than basic level. When using web-based positioning services, choosing the solution parameters appropriate to the data structure and the measurement method can bring the coordinate accuracy to the highest level. Applications for scientific research should indicate that such services are not suitable for applications that require expertise, such as ionospheric and tropospheric models, deformation analysis studies, earth orientation parameters, and so on.

The results from web-based location services show that there is not much difference between the results of software that solves with scientific PPP technique when there is enough observation period in GNSS sessions. This is rather obvious in the precision results given in **Figures 2–6**. In the application where PPP services are evaluated, it is seen that the results are directly related to the observation period. Accuracy is increased by increasing the observation time from 1 to 24 h, but the results are still at several centimeters. Precision results given in **Figures 2–6** are very similar to those published by the IGS. In order to be able to obtain accuracy results similar to those of precision results, one needs to adopt equal processing strategy for all software used here but unfortunately this was impossible throughout this study.

The user needs to select the observation period on the point according to the expected accuracy level. The results obtained from such services, which provide a great gain in terms of time and cost, are sufficient to give the position information for many engineering applications.

Acknowledgements

The author thanks to International GNSS Service (IGS) for product supports, and to organizations, which present web-based online services (CSRS-PPP, GAPS, APPS, MagicGNSS). Special thanks to Research Assistants Ali Hasan DOĞAN and Mustafa Fahri KARABULUT in Yildiz Technical University (YTU) for their help in assisting at the post processing stage of GPS observations by using GIPSY-OASIS II scientific software with PPP technique. NASA JPL's software GIPSY/OASIS II is licensed to Department of Geomatic Engineering of YTU.

Author details

Mustafa Ulukavak

Address all correspondence to: mulukavak@gmail.com

Harran University, Sanliurfa, Turkey

References

[1] Ghoddousi-Fard R, Dare P. Online GPS processing services: An initial study. GPS Solutions. 2006;**10**:12-20. DOI: 10.1007/s10291-005-0147-5

[2] El-Mowafy A. Analysis of web-based GNSS post-processing services for static and kinematic positioning using short data spans. Survey Review. 2011;**43**:535-549. DOI: 10.1179/003962611X13117748892074

[3] Gakstatter E. A Comparison of Free GPS Online Post-Processing Services GPS World [Internet]. 2013. Available from: http://gpsworld.com/a-comparison-of-free-gps-online-post-processing-services/ [Accessed: Apr 19, 2018]

[4] Ocalan T, Erdogan B, Tunalioglu N. Analysis of web-based online services for GPS relative and precise point positioning techniques. Boletim de Ciências Geodésicas. 2013;**19**(2):191-207. DOI: 10.1590/S1982-21702013000200003

[5] Zumberge JF, Heflin MB, Jefferson DC, Watkins MM, Webb FH. Precise point positioning for the efficient and robust analysis of GPS data from large networks. Journal of Geophysical Research. 1997;**102**(3):5005-5017. DOI: 10.1029/96JB03860

[6] Dach R, Hugentobler U, Fridez P, Meindl M. Manual of bernese GPS Software Version 5.0. University of Bern: Astronomical Institute; 2007. 612 p

[7] Transformation Parameters from ITRF08 to ITRF2014 [Internet]. 2018. Available from: http://itrf.ign.fr/doc_ITRF/Transfo-ITRF2014_ITRFs.txt [Accessed: Apr 28, 2018]

Chapter 6

Comparative Study of Some Online GNSS Post-Processing Services at Selected Permanent GNSS Sites in Nigeria

Olalekan Adekunle Isioye, Mefe Moses and
Lukman Abdulmumin

Additional information is available at the end of the chapter

http://dx.doi.org/10.5772/intechopen.79924

Abstract

Many applications in surveying and mapping have been made simpler and more precise due to the advent of GNSS, and thus, the demand for using cutting-edge GNSS techniques in surveying and mapping applications has become indispensable. Online GNSS post-processing services are now available to provide support for users in need of precise point positioning or conventional differential positioning services and without requiring a prior knowledge of GNSS processing software. This study evaluates the performance of some online GNSS facilities with emphasis on observation duration (i.e. 1hr, 2hr, 6hr 12hr and 24hr observations). Three of these online facilities (AUSPOS, GAPS and magic-GNSS) were chosen based on their mode of operation and were evaluated at the location of five permanent GNSS stations in Nigeria. The study cut across two epochs in the year 2014 (i.e. seven days each in the months of January and July). Results in this study indicate that users can expect reliable results from these online services and their accuracy is within allowable limits for mapping applications in Nigeria. The similarity of the results between all of the services used is amazing, thus further demonstrates the robustness of the algorithms and processes employed by the different online facilities.

Keywords: Global Navigation Satellite System (GNSS), continuously operating reference stations (CORS), precise point positioning (PPP), GNSS online processing, positioning accuracy

IntechOpen

1. Introduction

Global Navigation Satellite Systems (GNSS) is generic term for a composition of different satellite navigation technologies such as American GPS (Global Positioning System); its Russian equivalent, GLONASS (GLObal Navigation Satellite System); the Chinese system, BeiDou; the Japanese regional system, QZSS; the Indian regional system IRNSS (Indian Regional Navigation Satellite System); finally, is the European Galileo system. The GPS and GLONASS has since attained full operational status. The BeiDou, is expected to achieve completion for worldwide service in 2020, although a limited version of its signal has already been available since December 2012. The QZSS, is at present providing a limited service in the form of an augmented signal for GPS, but should be progressively upgraded and achieve full impartiality in 2023. The IRNSS, is at a final point operation as well. The Galileo system is expected to attain full operational capability in 2020 [1, 2].

Global Navigation Satellite System (GNSS) is one of the most innovative and practical technology developed in recent times. Since its inception it has grown to provide not only world-wide, all weather navigation, but precise position determination capabilities to all manner of users especially for surveying and geodetic applications. In surveying and mapping, this represents a revolutionary departure from conventional surveying procedures, which relied on observed angles and distances for determining point positions [3, 4].

Traditionally, it was necessary to obtain positioning with GNSS using at least two receivers, and the collected data processed for high accurate positioning using the GNSS data processing software whether scientific or commercial. However, the usage of such software is also quite difficult because they generally require deep knowledge of the GNSS, experience in the processing and they mostly need a licencing fee [4–7].

A remarkable volume of information and resources on GNSS are available on the internet including GNSS raw data, precise GNSS satellite orbit and clock files (which are provided by the international GNSS Service (IGS) and many other organisations, as well as some GNSS processing software (e.g., see [8]). This software vary in terms availability for use (cost), accuracy, and their mode of operation which are often dependant on the technical know-how of the users. Some of the very accurate but complex to use software are GAMIT/GLOBK (from Department of Earth Atmospheric and Planetary Sciences, MIT), GIPSY/OASIS-II (from Jet Propulsion Laboratory, JPL), PAGES (from United States National Geodetic Survey, NGS). The BERNESE software (from the Astronomisches Institut der Universitat Bern, Switzerland), is a state-of-the-art GNSS processing software similar to GIPSY and GAMIT but available only commercially at a very high cost. There are also numerous MATLAB based GNSS processing system which are freely available online (e.g., see [8, 9]), however, users require requisite skills to use them. Numerous studies have explore and put forward improvements in GNSS processing system that will aid users confronted with challenges enumerated herein [5, 6, 10].

Regarding the improvements in GNSS data processing methodology, many new opportunities have been offered to the users. In this respect, many organisations have developed online

GNSS processing services. These services provide GNSS processing results to the user free of charge and with unlimited access. The user sends a Receiver Independent Exchange Format (RINEX) file to the service and within a short period of time, the estimated position of the receiver used to collect the RINEX data is sent back to the user. Organisations that provide these free services include: Geohazards Division of Geoscience Australia, the Geodetic Survey Division (GSD) in Canada, the United States' National Geodetic Survey (NGS), Scripps Orbit and Permanent Array Center (SOPAC) at the University of California and the Jet Propulsion Laboratory (JPL) at National Aeronautics and Space Administration (NASA) [7].

The only requirement for using these services is a computer having an internet connection and web browser. These services are designed to be as simple as possible for the user and with minimal input. Users of such systems have to perform uploading/sending of their collected data in RINEX format by using the web site of these services, e-mail or ftp sites to the system and selecting a few processing options. Some of these services process not only the GPS but also the data of other systems, particularly those of GLONASS, and provide resilience and a higher accurate positioning service in certain cases to their users [5].

Currently, there are several online GNSS post-processing services, and are best categorised base on their adopted approach of processing the RINEX files. Categorically, there are those that use the Precise Point Positioning (PPP) approach (see [11–13] for documentation). Those in this category include Canadian Spatial Reference System-Precise Point Positioning (CSRS-PPP), magicGNSS, (APPS) and GPS Analysis and Positioning Software (GAPS). PPP based services used the GNSS data collected with only a single receiver with precise satellite ephemerides and clock data by taking into account corrections like carrier phase wind-up, satellite antenna phase offset, solid and ocean tides. The category of the GNSS online processing services that adopted the conventional relative approach, where user's RINEX files are processed relative to other GNSS continuously operating reference stations (CORS). The Trimble RTX, Australian Surveying and Land Information Group Online GPS Processing Service (AUSPOS) and Online Positioning User Service (OPUS) are based on this approach [5].

The application/usage of these facilities are gaining global acceptance and numerous studies have evaluated the accuracy of different online GNSS processing in different part of the world (e.g. Australia, Egypt, etc.). The results of such studies have demonstrated inherent limitations, the accuracies, conveniences of online post processing of GNSS observations, and have also identified a wide range of uses within the surveying community (e.g., see [13–15]). This chapter is dedicated to the report on the accuracy of three online GNSS processing facilities (magic GNSS, GAPS, and AUSPOS) over the territory of Nigeria. The major objective of the study is to investigate the effects of the variation in the duration of GNSS observation sessions on the positional accuracy when using online processing facilities.

The structure of the paper is as follows: first a general description and status of the different online GNSS post-processing services is presented in Section 2. Section 3 explains the methods used in the data acquisition, processing and evaluation of results. Section 4 describes the results. Lastly, the concluding remarks were presented and additionally, the paper gives insight into possible future expansion of GNSS infrastructures in Nigeria.

2. Overview of GNSS data processing and online services

Currently, there exist several online facilities for GNSS post processing applications. The different facilities or services are provided by different organisations and thus their mode of processing, restrictions, processing options, and format/latency of results varies. **Table 1** gives a summary of the comparison of the different facilities.

Each of the above-mentioned organisations have different technical specifications with respect to service features such as membership requirement, storage limitation of the GPS/GNSS RINEX data to be uploaded, process in static/kinematic modes, evaluation the data collected by single/dual or multi frequency receiver, GPS/GNSS antenna type selection, etc. The basic requirements that the user needs to take advantage of these different services are almost the same: access to the Internet and a valid email address. The user sends a Receiver Independent Exchange Format (RINEX) file to the service and within a short period of time, the estimated position of the receiver used to collect the RINEX data is sent back to the user. Solution quality from the various processing services depends on the availability, proximity and quality of base station data, and the availability of precise satellite orbits and clock corrections.

3. Methodology

Three online GNSS processing software were selected for this study. The selection was based on their mode of processing. One out of the selected three used the relative solution approach (i.e. AUSPOS) and the remaining two utilises the PPP technique (i.e. magicGNSS and GAPS).

The study utilised data from the new Nigerian GNSS Network (NIGNET) [16, 17] for the evaluation of the selected online GNSS services. Daily GNSS data in Hatanaka-compressed ASCII format were downloaded from the NIGNET site at www.nignet.net. The files were uncompressed with the freely available CRX2RNX software. The GNSS data were downloaded at the location of five different stations in the NIGNET (see **Figure 1**) for the year 2014. These stations include: ABUZ (Zaria); BKFP (Birnin-Kebbi); CLBR (Calabar); FUTY (Yola); and UNEC (Enugu). The stations were selected based on the data available per day (data consistency) from each station as the NIGNET is often characterised by large data gaps [18].

The GNSS data were collected at two epochs corresponding to GPS weeks 1774 and 1800, respectively. The data were collected for all 7 days in each week, it cuts across two different seasons of the year (months of January and July). The reason for this was to identify possible seasonal variations in the estimated coordinates from the different online facilities. The daily (24 h) RINEX files (observation data files) at each station were then decimated into 2, 6 and 12 h using the TEQC analysis software. This was done in order to check the effect of the length of observation session on the output of the different online GNSS processing services. The 24 h files and the decimated files were submitted to the three GNSS online processing services (magicGNSS, GAPs, and AUSPOS). After submission, both the 24 h and decimated files were processed and all the results were received via e-mail.

Service short name	Organisation /company	Software	Supported constellations	Data transfer method	Restrictions of length of GPS data set	Available options	Coordinates (Datum)	Websites
AUSPOS	Geoscience Australia USA	Bernese	GPS	Web service (uploading), via anonymous FTP	Minimum of 1 h. Maximum of 7 days of data	Dual frequency, static observations, DGPS only	ITFR2008, GDA 2020, GDA94	http://wwwb.ga.gov.au/bin/gps.pl
CSRS-PPP	Natural Resources Canada	NRCanPPP	GPS, GLONASS	Web Service (uploading)	No minimum Maximum 6-day long Provided uncompressed RINEX file is less than 100 MB	Single and dual frequency in static and kinematic mode, uses velocity grid (NUVEL1-A model) to account for crustal motion, PPP only	IGS 2014, ITRF 2008, NAD83 (CSRS)	http://www.geod.nrcan.gc.ca/online_data_e.php
OPUS	National Geodetic Survey	PAGES	GPS	Web service (uploading)	Minimum 2 h. Maximum 24 h	Dual frequency, static observations. Services available only to central and north America	ITRF 2008	http://www.ngs.noaa.gov/OPUS/
GAPS	University of New Brunswick	GAPS v6.0.0 r587	GPS, Galileo, BeiDou	Uploading via web service (supports RINEX 2, 3, and raw data)	Minimum 2 h	Dual frequency pseudo-range and carrier phase static and kinematic observations, basic and advance mode of processing, PPP only	ITRF 2008, ETRF 2005 & earlier solutions	http://gaps.gge.unb.ca/
APPS	NASA Jet Propulsion Laboratory	AUTO-GIPSY 6.4	GPS, GLONASS, BeiDou	Uploading, FTP, email (RINEX 2, GIPSY TDP files)	Process multiple RINEX files in a single session, multi-day RINEX files	Dual and single frequency, four processing mode(static, kinematic, NRT, most accurate), user input pressure correction, PPP and DGNSS services	ITRF 2008	http://apps.gdgps.net/
Magic-GNSS	GMV Innovating Solutions	Magic PPP client (magicAPK)	GPS, GLONASS, Galileo, BeiDou, QZSS	Uploading and E-mail (RINEX-2, RINEX-3, RTCM 10403.2)	No restrictions	Dual frequency, static and kinematic observations, PPP only	ITRF 2008	http://magicgnss.gmv.com/ppp
Trimble RTX	Trimble Navigation Limited	Trimble office	GPS, GLONASS, Galileo, BeiDou, QZSS	Uploading (RINEX 2, RINEX 3)	Minimum of 1 h Maximum 24 h	Dual frequency pseudo-range and carrier phase observations, static observations, PPP	ITRF 2014 with options for other datum, option of plate model	http://www.trimblertx.com/UploadForm.aspx

Table 1. Overview of the structures, requirements, and processing options of the different online GNSS post-processing services.

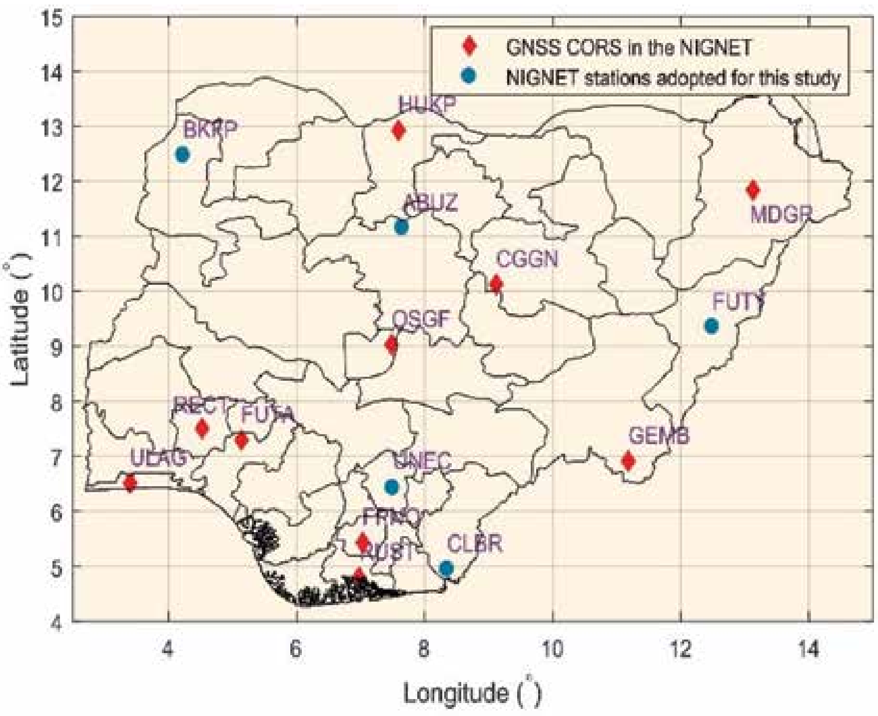

Figure 1. Location of permanent GNSS stations in the Nigerian GNSS network (NIGNET).

To compare the results from the online GNSS post processing facilities with known station coordinates which were originally obtained from long time station average using BERNESE software, the residuals (differences) in northing, easting and heights components were computed for all observations in the two epoch and were employed in subsequent analysis. Consequently, the root-mean-square error (RMSE) in both the vertical and horizontal directions were computed from the differences using Eqs. (1) and (2). Similarly, the Horizontal RMSE (HRMSE) and vertical RMSE (VRMSE) were calculated using Eqs. (3) and (4);

$$RMSE_{North} = \sqrt{\sum_{i=1}^{n} \frac{(P_{i,North} - O_{i,North})^2}{n}} \tag{1}$$

$$RMSE_{East} = \sqrt{\sum_{i=1}^{n} \frac{(P_{i,East} - O_{i,East})^2}{n}} \tag{2}$$

$$HRMSE = \sqrt{(RMSE_{North})^2 + (RMSE_{East})^2} \tag{3}$$

$$VRMSE = \sqrt{\sum_{i=1}^{n} \frac{(P_{i,Vertical} - O_{i,Vertical})^2}{n}} \tag{4}$$

In Eqs. (1), (2), and (4); P_i is the known station coordinates for the NIGNET stations and the estimated coordinates from the different online GNSS services are denote by O_i, and n is the total number of observations.

4. Results and discussions

The coordinate of the NIGNET stations were obtained in geographic unit and were converted to equivalent Universal Traverse Mercator (UTM) coordinate system with projection on the WGS 84 ellipsoid. The coordinates of the selected five NIGNET station for this study in UTM (Northing, Easting and Height) system is presented in **Table 2**. Similarly, all 3D coordinates obtained from the magicGNSS, GAPS, and AUSPOS were converted to UTM system for easy comparison. Appendices A.1–A.5 contain the average 3D coordinates of the stations at the 2, 6, 12, and 24 h observation sessions.

To compare accuracy of magicGNSS, AUSPOS, and GAPS online services, the coordinates of the selected permanent GNSS site which were originally computed using BERNESE software are taken as reference. The coordinate differences of each online services subtracted from reference coordinates of all the stations and RMSE, HRMSE, and VRMSE have been computed by Eqs. (1)–(4). The combined results of the performance measures (RMSE, HRMSE, and VRMSE) is presented in **Table 3** for observations at all the permanent GNSS stations in January 2014 (first epoch).

The RMSE values for the east and north components are typically less than 0.3 m for the magic GNSS and GAPS services; while those of the AUSPOS service were higher and greater than 0.3 m in all instances as seen in **Table 3**. Accordingly, the HRMSE values for the magicGNSS and GAPS were also less than those from AUSPOS; also, the VRMSE values for AUSPOS are higher than those of magicGNSS and GAPS which is an indication that AUSPOS results are less accurate when compared to magicGNSS and GAPS. **Figure 2** is a plot of the different performance measures, it very evident form **Figure 2** that AUSPOS performs less than the other two services. Also, it can be seen the 24 h file do not always give the best results. However, AUSPOS did gave some deterrent messages on the use of 2 h files for processing.

Again, the combined results of the performance measures (RMSE, HRMSE, and VRMSE) is presented in **Table 4** for observations at all the permanent GNSS stations in July 2014 (second epoch).

S/no	Stations	Easting (m)	Northing (m)	Height (m)
1.	ABUZ	352440.6939	1233094.064	705.0536
2.	BKFP	633587.9715	1378678.241	249.9995
3.	CLBR	428111.6667	547205.768	57.1295
4.	FUTY	884308.222	1035426.663	247.3917
5.	UNEC	334662.4162	710405.3358	254.3912

Table 2. The UTM coordinates of the selected GNSS stations from the NIGNET.

Duration (h)	RMSE (E)	RMSE (N)	HRMSE	VRMSE
magicGNSS				
2	0.10823	0.10840	0.04316	0.15318
6	0.09798	0.12607	0.04410	0.15967
12	0.10634	0.11150	0.04231	0.15408
24	0.10768	0.10840	0.04293	0.15280
AUSPOS				
2	0.37673	0.69649	0.34905	0.62703
6	0.36023	0.71277	0.41569	0.63781
12	0.34954	0.71344	0.41882	0.63118
24	0.38925	0.70973	0.42112	0.80946
GAPS				
2	0.22128	0.04342	0.03108	0.22550
6	0.19239	0.04253	0.03108	0.19703
12	0.20384	0.05975	0.03153	0.21242
24	0.22508	0.14803	0.02749	0.26940

Table 3. Performance of online GNSS services during the first epoch of observation.

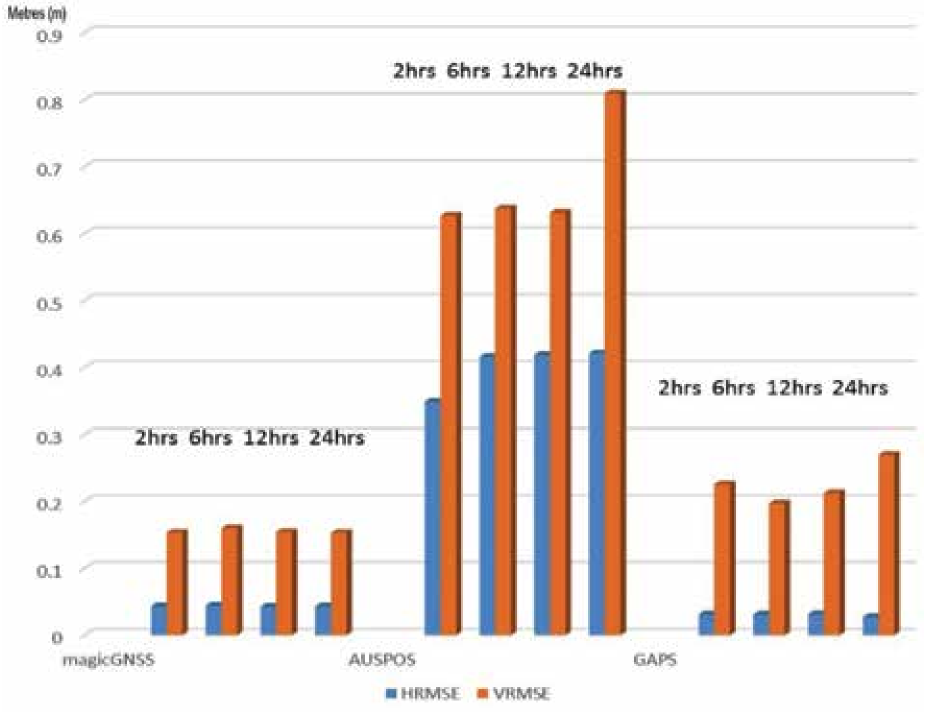

Figure 2. A plot of the HRMSE and VRMSE for the different online GNSS services during the first epoch of observations.

The results from **Table 4** are in very good agreement with those in earlier discussed (**Table 3** for the first epoch of observations). **Figure 3** is a plot of the different performance measures for the second epoch of observation.

From **Figure 3** it is evident that the 24 h observation files and the decimated files (2, 6 and 12 h), produce results with millimetre (mm) to a centimetre (cm) level of accuracy when processed with magicGNSS and GAPS. It is again evident from **Figure 3** that magicGNSS produces the best results, followed by GAPS and then AUSPOS. This is the same for the two epochs.

The AUSPOS is the only one of the three facilities that utilises the relative approach, its results were not pleasing, the poor performances of AUSPOS is attributed long baselines in the processing because of non-availability of nearby IGS stations for the processing. Thus, baselines of shorter lengths will increase the quality of data, the reliability and dependability of the online AUSPOS facilities. As earlier stated, AUSPOS again gave a warning message in processing the 2 h files indicating that the precision of estimated coordinates are outside the confidence level but the situation was different with magicGNSS and GAPS.

All the three services investigated in this study return results to users via email. Time delay on receiving the results depends on several factors including the traffic on the Internet and the number of users accessing the service at the same time. The displayed times in **Table 5** are only a rough estimates in order to compare the speed of each of the services and were obtained by submitting the same 24 h data set to each of the service.

The AUSPOS is the fastest to return results, followed by GAPS and then magicGNSS; again it was found to be more user friendly, followed by magicGNSS (e-mail version) and then GAPS.

Duration (h)	**RMSE (E)**	**RMSE (N)**	**HRMSE**	**VRMSE**
Magic GNSS				
2	0.12714	0.12379	0.03169	0.17745
6	0.10241	0.11328	0.02096	0.15271
12	0.07737	0.11046	0.02095	0.13486
24	0.10147	0.10527	0.02583	0.14622
AUSPOS				
2	0.58026	0.11122	0.44654	0.59082
6	0.56693	0.11216	0.44207	0.57792
12	0.57561	0.11502	0.43894	0.58699
24	0.68495	0.30499	0.44182	0.74979
GAPS				
2	0.03041	0.00040	0.03958	0.03041
6	0.06927	0.00434	0.04003	0.06941
12	0.11972	0.45249	0.03421	0.46806
24	0.26515	0.45061	0.03841	0.52284

Table 4. Performance of online GNSS services during the second epoch of observation.

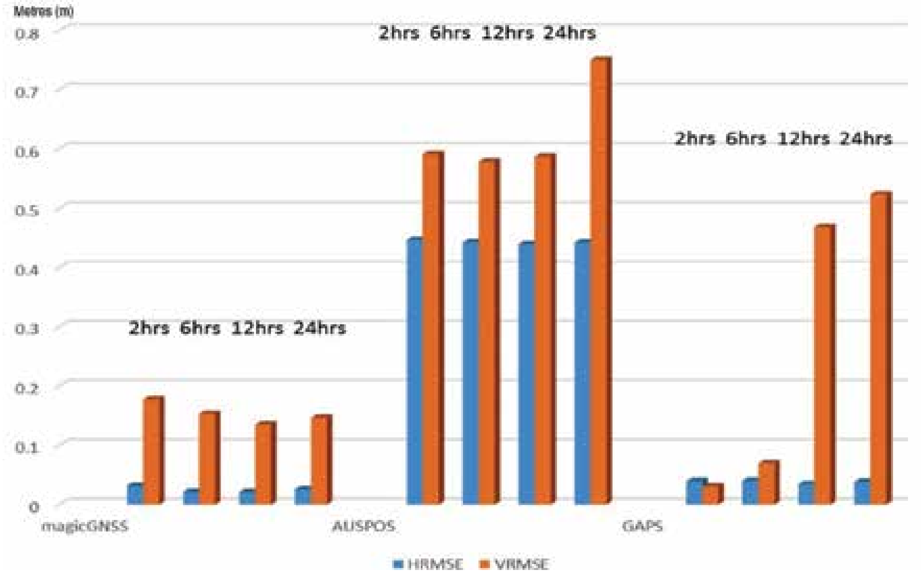

Figure 3. A plot of the HRMSE and VRMSE for the different online GNSS services during the second epoch of observations.

Elapsed time (min)	MagicGNSS		AUSPOS		GAPS	
	Min	**Max**	**Min**	**Max**	**Min**	**Max**
	2	1440	1	2	2	3

Table 5. Latency results from magicGNSS, AUSPOS, and GAPS online GNSS post-processing services.

The GAPS facilities has some security features which sometimes exasperate the process of submitting files for processing. Also, the advanced mode of processing in GAPS gives room to decimate files automatically by just giving the range of observation without going into the tedious processes of doing it with TEQC software.

5. Concluding remarks

In this work, a comparative analysis of some online GNSS post-processing services at locations of permanent GNSS stations in Nigeria has been made. Online GNSS processing services can help users either using precise point positioning (PPP) or differential method, and without requiring a prior knowledge of GNSS processing software. Results in this project indicate that users can expect reliable results from these online services. The similarity of the results between all of the services used is amazing. That they differ only by a few millimetre (mm) or centimetre (cm) demonstrates the robustness of the algorithms and processes they employ in processing GNSS observations. Results for decimated daily RINEX files also show that users can process data sets of less than 24 h observation period and expect almost the same results (or better results in some cases) when compared to the 24 h data set. Among the three online facilities examined in this study, the AUSPOS seems to have the most flexible and user friendly interface, followed by magicGNSS and then GAPS. As mentioned earlier, magicGNSS produces the best result, followed by GAPS and then AUSPOS. When selecting a faster means of obtaining result from these software, AUSPOS is the fastest, followed by GAPS and then magicGNSS. The reason why AUSPOS did not perform as GAPS and magicGNSS is due to the effect of long baselines in the processing and this again affirm the advantage of the PPP techniques. Regardless of the problem that might be encountered in the return of results (processed coordinate values), magicGNSS is undoubtedly the best of the three. Undoubtedly, the online GNSS facilities have brought a paradigm shift in GNSS positioning applications, in view of the accuracy and efficiency (saving cost of buying and operating a second receiver) they offer to users. It is therefore necessary that if any of these facilities (including those not considered in this study) is to be used for processing, the need for reliability and accuracy must first be considered. Finally, creating awareness among surveyors and other professionals on the functionality and dependability of online GNSS post-processing services is needed so that they can fully explore the potential of these facilities in mapping and possibly cadastral applications in Nigeria and other parts of the world.

Acknowledgements

The authors would wish to express their profound gratitude to the numerous reviewers for their productive observations that helped to perk up this chapter. We wish to thank the office of the Surveyor General of the federal republic of Nigeria (OSGOF) for the GNSS data used in the study.

Conflict of interest

The authors avow that there no conflicts of interest regarding the publication of this manuscript.

Authors’ contribution

OAI conceived the idea of the paper, MM and LA downloaded, prepared and processed all dataset used in the report, manuscript was drafted by OAI. All authors read and approved the final draft.

Appendices and nomenclature

The mean station coordinates for ABUZ, BKFP, CLBR, FUTY, and UNEC for the two epochs of study are presented in Appendices A.1–A.5, respectively.

A.1. Mean station coordinates for ABUZ in the two epochs of observation

	Duration (h)	**Station coordinate**		
		Easting (m)	**Northing (m)**	**Height (m)**
		Epoch 1		
MagicGNSS	2	352440.7181	1233094.105	705.054
	6	352440.718	1233094.108	705.051
	12	352440.7182	1233094.103	705.053
	24	352440.7185	1233094.104	705.054
AUSPOS	2	352441.0593	1233094.676	705.234
	6	352441.0581	1233094.679	705.232
	12	352441.0592	1233094.679	705.236
	24	352441.056	1233094.676	705.234
GAPS	2	352440.8165	1233094.156	705.073
	6	352440.8493	1233094.155	705.071
	12	352440.8274	1233094.149	705.07
	24	352440.8165	1233094.154	705.073
		Epoch 2		
MagicGNSS	2	352440.7617	1233094.105	705.053
	6	352440.7508	1233094.103	705.054
	12	352440.7398	1233094.1	705.053
	24	352440.718	1233094.102	705.053
AUSPOS	2	352440.7509	1233094.126	705.237
	6	352440.729	1233094.127	705.239
	12	352440.7508	1233094.122	705.24
	24	352440.7507	1233094.132	705.236
GAPS	2	352440.7302	1233094.15	705.064
	6	352440.7304	1233094.146	705.065
	12	352440.7305	1233094.148	705.063
	24	352440.7299	1233094.148	705.064

A.2. Mean station coordinates for BKFP in the two epochs of observation

	Duration (h)	Coordinates		
		Easting (m)	Northing (m)	Height (m)
		Epoch 1		
MagicGNSS	2	633588.0497	1378678.305	250.049
	6	633588.0494	1378678.302	250.048
	12	633588.0496	1378678.306	250.05
	24	633588.0495	1378678.305	250.048
AUSPOS	2	633588.0703	1378678.9	250.184
	6	633588.07	1378678.902	250.18
	12	633588.0701	1378678.903	250.183
	24	633588.0702	1378678.901	250.184
GAPS	2	633588.0933	1378678.284	250.001
	6	633588.093	1378678.286	250.003
	12	633588.0933	1378678.284	250.004
	24	633588.0932	1378678.285	249.999
		EPOCH 2		
MagicGNSS	2	633588.047	1378678.302	250.012
	6	633588.0472	1378678.303	249.999
	12	633588.047	1378678.303	250
	24	633588.0471	1378678.301	250.013
AUSPOS	2	633588.0402	1378678.778	250.19
	6	633588.0404	1378678.777	250.189
	12	633588.0407	1378678.775	250.19
	24	633588.0402	1378678.777	250.192
GAPS	2	633588.0417	1378678.341	250.012
	6	633588.0418	1378678.342	250.01
	12	633588.042	1378678.34	250.009
	24	633588.0417	1378678.34	250.008

A.3. Mean station coordinates for CLBR in the two epochs of observation

	Duration (h)	Coordinates		
		Easting (m)	Northing (m)	Height (m)
		EPOCH 1		
MagicGNSS	2	428111.7174	547205.8302	57.183
	6	428111.7173	547205.8324	57.184
	12	428111.717	547205.8335	57.183
	24	428111.7171	547205.8314	57.183
AUSPOS	2	428111.8034	547205.8643	57.344
	6	428111.7912	547205.8645	57.343
	12	428111.769	547205.8644	57.344
	24	428111.7468	547205.8649	57.343
GAPS	2	428111.7848	547205.83	57.167
	6	428111.7845	547205.8296	57.17
	12	428111.7846	547205.8293	57.171
	24	428111.7848	547205.8317	57.167
		EPOCH 2		
MagicGNSS	2	428111.7213	547205.8316	57.188
	6	428111.7202	547205.8319	57.185
	12	428111.7191	547205.8312	57.181
	24	428111.718	547205.8316	57.182
AUSPOS	2	428111.7158	547204.7951	57.357
	6	428111.7147	547204.7918	57.358
	12	428111.7158	547204.7929	57.357
	24	428111.9527	547204.3555	57.356
GAPS	2	428111.3121	547204.4158	57.178
	6	428111.2899	547204.4192	57.18
	12	428111.2566	547204.417	57.172
	24	428111.2613	547204.4157	57.178

A.4. Mean station coordinates for FUTY in the two epochs of observation

	Duration (h)	**Coordinates**		
		Easting (m)	**Northing (m)**	**Height (m)**
EPOCH 1				
MagicGNSS	2	884308.2235	1035426.664	247.393
	6	884308.2133	1035426.701	247.401
	12	884308.2334	1035426.668	247.39
	24	884308.2224	1035426.663	247.393
AUSPOS	2	884308.4531	1035426.813	247.572
	6	884308.3431	1035426.81	247.57
	12	884307.1331	1035426.798	247.571
	24	884308.4532	1035426.802	247.572
GAPS	2	884308.2816	1035426.356	247.4
	6	884308.1815	1035426.466	247.404
	12	884308.2246	1035426.555	247.401
	24	884308.2812	1035426.733	247.399
EPOCH 2				
MagicGNSS	2	884308.2342	1035426.7	247.4
	6	884308.1904	1035426.677	247.395
	12	884308.1464	1035426.675	247.4
	24	884308.2225	1035426.662	247.392
AUSPOS	2	884308.2779	1035426.726	247.58
	6	884308.2713	1035426.726	247.578
	12	884308.2669	1035426.725	247.572
	24	884308.2757	1035426.727	247.579
GAPS	2	884307.4646	1035426.76	247.4
	6	884307.5736	1035426.75	247.401
	12	884307.6836	1035426.749	247.401
	24	884307.8574	1035426.754	247.402

A.5. Mean station coordinates for UNEC in the two epochs of observation

	Duration (h)	**Coordinates**		
		Easting (m)	**Northing (m)**	**Height (m)**
		EPOCH 1		
MagicGNSS	2	334662.5036	710405.410	254.383
	6	334662.4914	710405.413	254.380
	12	334662.4899	710405.416	254.384
	24	334662.5036	710405.418	254.383
AUSPOS	2	334662.5126	710405.410	254.573
	6	334662.5134	710405.411	254.570
	12	334662.5105	710405.417	254.569
	24	334662.5145	710405.415	254.573
GAPS	2	334662.4889	710,405. 429	254.394
	6	334662.4919	710405.433	254.389
	12	334662.4962	710405.388	254.390
	24	334662.4979	710405.391	254.390
		EPOCH 2		
magicGNSS	2	334662.4904	710405.4100	254.383
	6	334662.4907	710405.4102	254.380
	12	334662.491	710405.4096	254.378
	24	334662.4916	710405.4106	254.383
AUSPOS	2	334662.483	710405.398	254.6
	6	334662.4826	710405.3992	254.59
	12	334662.4832	710405.3997	254.588
	24	334662.4826	710405.3983	254.588
GAPS	2	334662.4897	710405.4041	254.4
	6	334662.4895	710405.4049	254.399
	12	334662.4899	710405.406	254.397
	24	334662.4871	710405.405	254.399

Author details

Olalekan Adekunle Isioye*, Mefe Moses and Lukman Abdulmumin

*Address all correspondence to: lekkyside4u@yahoo.com

Department of Geomatics, Ahmadu Bello University, Zaria, Kaduna, Nigeria

References

[1] Hoffmann-Wellenhof B, Litchtenegger H, Wasle E. GNSS—Global Navigation Satellite Systems: GPS, GLONASS, Galileo and More. Vienna: Springer-Verlag; 2008. ISBN: 987-3-211-73012-6(print)

[2] Shaw M. GPS Modernization: On the Road to the Future GPS IIR/IIR-M and GPS III.UN/UAE/US Workshop on GNSS Applications, Session 1: Trends in Satellite-Based Navigation Systems; Dubai, UAE. 2011

[3] Awange JL. Environmental Monitoring Using GNSS: Global Navigation Satellite Systems. New York: Springer-Verlag; 2012. ISBN: 978-3-540-88255-8(Print)

[4] Ocalan T. Accuracy assessment of GPS precise point positioning (PPP) technique using different web-based online Services in a forest environment. Sumarski List. 2016;**7-8**: 357-368

[5] Alkan RM, Ozulu M, Ilci V. Web-based GNSS data processing services as an alternative to conventional processing technique. In: FIG Working Week 2016; New Zealand. pp. 1-35

[6] Satirapod C, Wong K, Rizos C. A web-based automated GPS processing system. In: The Proceedings of the 2nd Trans-Tasman Surveyors Congress, Queenstown; 20–26 August 2000; New Zealand. Available from: https://www.researchgate.net/publication/250222229_A_WEB-BASED_AUTOMATED_GPS_PROCESSING_SYSTEM. [Accessed: 2018-05-12]

[7] El-Mowafy A. Analysis of web-based GNSS post-processing services for static and kinematic positioning using short data spans. Survey Review. 2013;**43**(323):535-549. DOI: 10.1179/003962611X13117748892074

[8] On-line Geodesy Resources: GPS. 2018. Available from: http://www3.sympatico.ca/craymer/geodesy/gps.html [Accessed: 2018-05-12]

[9] Strang G, Borre K. Linear Algebra, Geodesy, and GPS. Wellesley: Wellesley-Cambridge Press; 1997. 624 p

[10] Isioye OA, Enebeli I, Shebe MW, Mefe M. Near real time processing solution of differential GPS positioning using internet technology. Asian Journal of Engineering Science and Technology. 2011;**1**(2):58-66. A publication of the Faculty of Engineering, Sciences and

Technology, Iqra University, Karachi, Pakistan, September 2011. Available from: http://ajest.iqra.edu.pk/journal.php. ISSN: 2007-1142

[11] Rizos C, Janssen V, Roberts C, Ve Grinter T. Precise point positioning: Is the era of differential GNSS positioning drawing to an end? In: The Proceedings FIG Working Week; 6-10 May 2012; Rome, Italy. 2012

[12] Zumberge JF. Automated GPS data analysis service. GPS Solutions. 1999;**2**(3):76-78

[13] Zumberge JF, Heflin MB, Jefferson DC, Watkins MM, Webb FH. Precise point positioning for the efficient and robust analysis of GPS data from large networks. Journal of Geophysical Research. 1997;**102**(B3):5005-5017

[14] Ghoddousi-Fard R, Dare P. Online GPS processing services: An initial study. GPS Solutions. 2006;**10**:12-20

[15] Ebner R, Featherstone W. How well can on-line GPS PPP post processing services be used to establish geodetic survey control networks. Journal of Geodesy. 2008;**2**:149-157

[16] Jatau B, Fernandes RMS, Adebomehin A, Goncalves N. NIGNET-the new permanent GNSS network of Nigeria. In: FIG Congress 2010 Facing the Challenges—Building the Capacity Sydney; 11-16 April 2010; Australia

[17] Naibbi AI, Ibrahim SS. An assessment of the existing continuously operating reference stations (CORS) in Nigeria: An exploration using geographical information system (GIS). American Journal of Geographic Information System. 2014;**3**(4):147-157. DOI: 10.5923/j.ajgis.20140304.01

[18] Isioye OA, Combrinck L, Botai J. Evaluation of spatial and temporal characteristics of GNSS-derived ZTD estimates in Nigeria. Theoretical and Applied Climatology. 2017;**132**: 1099. DOI: doi.org/10.1007/s00704-017-2124-7

Section 5

Accuracy of Positions Derived from the Combination of Terrestrial Geodetic Techniques and GNSS

Development of Recurrent Method with Rotation for Combined Adjustment of Terrestrial Geodetic and GNSS Networks in National Spatial Reference System

Ha Minh Hoa

Additional information is available at the end of the chapter

http://dx.doi.org/10.5772/intechopen.78770

Abstract

A construction of national spatial reference systems (NSRS) is promoted in many countries due to modern achievements of Global Navigation Satellite System (GNSS) methods and results of building of high accurate geoid/quasi-geoid models at centimeter level of accuracy. One of the most popular methods used for the construction of the NSRS is related to Helmert block adjustment method, by which we ought to solve techno-scientific task of a separate adjustment of GNSS network in International Terrestrial Reference Frame (ITRF) and next combination of a results of adjustment of the terrestrial geodetic and GNSS networks in the NSRS. In this chapter, we carry out a research on the usage of a recurrent adjustment method with Givens rotation for solving the abovementioned task on an account of its advantages of being effective for application of a technique of sparse matrix, outlier detection and very simple for solving the subsystem of observation equations, created based on the transformation of the results of the separate adjustment of the GNSS network from the ITRF into the NSRS. The experiment results of solving the abovementioned task for the GPS network in the North Vietnam had shown that the horizontal and vertical position accuracy of the GPS points in VN2000–3D had reached the few centimeter level.

Keywords: method of recurrent adjustment, combined adjustment of terrestrial geodetic and GNSS networks, recurrent adjustment method with rotation, method of Givens rotation, national spatial reference system

1. Introduction

In the past, in different countries, national horizontal and vertical reference systems had been constructed independently from each other; in addition, horizontal control points almost did not coincide with vertical control points. A national first- and second-order astro-geodetic network constructed by traditional geodetic methods did not allow to obtain horizontal positioning accuracy of the horizontal control points at the centimeter level. Because of an accumulation of measurement errors in the national horizontal control network, a coordinate transmission from one origin point led to the more horizontal positioning error of the distant horizontal control points. For example, the horizontal position accuracy in NAD83 (1986) reached the level of 1 m [4, 34]. Such analogical situation had also been happened to the vertical control network. For the national first- and second-order astro-geodetic networks of the former Soviet Union in SK95, the maximal RMS of horizontal position of horizontal control points reached the level of 1.5 m [9].

Nowadays, traditional geodetic methods cannot satisfy the accuracy requirements of the national horizontal and vertical reference systems at the centimeter level according to modern techno-scientific achievements. The abovementioned accuracy requirements only will be satisfied by the construction of the NSRS based on modern achievements of the GNSS methods, the construction of the highly accurate national geoid/quasi-geoid model and the geopotential vertical datum.

Present-day worldwide and rapid development of GNSS methods, especially the construction of Continuously Operating Reference Station (CORS) networks of GNSS base stations and mathematical processing of GNSS data in the ITRF with usage of International GNSS Service (IGS) products, and construction of national hybrid geoid/quasi-geoid models with an accuracy at the level of few centimeters had created favorable conditions for building of the NSRS in many countries, for example, ETRS89/DREF91/2016 (Germany), GDA2020 (Australia) [14], NSRS2022 (USA CONUS, Canada, Caribbean Islands. Hawaii and Greenland) [35], and so on.

In case of processing the GNSS data in the ITRF, highly accurate spatial coordinates of geodetic points will be converted from the ITRF to the NSRS by the seven parameter Bursa-Wolf formula. Next, we symbolize $\mathbf{X_0},\ \mathbf{Y_0},\ \mathbf{Z_0},\ \varepsilon_X,\ \varepsilon_Y,\ \varepsilon_Z,\ \mathbf{\Delta m}$ as the seven coordinate transformation parameters from the ITRF to the NSRS by Bursa-Wolf formula, where $\mathbf{X_0},\ \mathbf{Y_0},\ \mathbf{Z_0}$ are the spatial coordinates of the origin of the ITRF with respect to the origin of the NSRS, $\varepsilon_X,\ \varepsilon_Y,\ \varepsilon_Z$ are Euler rotation angles of the coordinate axes of the ITRF with respect to the analogical coordinate axes of the NSRS, $\mathbf{\Delta m}$ is a scale factor change.

For geodetic purposes, the NSRS contains an ellipsoidal surface used as the reference surface for the determination of an ellipsoidal coordinate system and a national plane coordinate system. A Geoid/quasigeoid surface is used for the reference surface of the national vertical reference system. In addition, the national geoid/quasigeoid model creates relationship of the geoid/quasi-geoid surface to the ellipsoidal surface and satisfies the connection of the spatial coordinates of geodetic points with the national vertical reference system.

In practice of the construction of GNSS network by the static relative positioning technique, the components $\mathbf{\Delta X},\ \mathbf{\Delta Y},\ \mathbf{\Delta Z}$ of baseline vector between two GNSS points obtained from the processing of GNSS observations have been used as measured values in the GNSS network. Using IGS products for processing GNSS observations in the ITRF, the components

$\mathbf{\Delta X}$, $\mathbf{\Delta Y}$, $\mathbf{\Delta Z}$ of the baseline vectors have very high accuracy and have been used for the adjustment of the GNSS network. In [19], formulas for apriori assessment of relative horizontal position accuracy $\mathbf{M_{xy}}$ between two GNSS points and accuracy of ellipsoidal height $\mathbf{m_{\overline{H}}}$ had been proposed in the following forms:

$$\mathbf{M_{xy}} = \pm\ \frac{\mathbf{1}}{\sqrt{\mathbf{2}}}.\left(\frac{\mathbf{M_S}}{\mathbf{1\ \ cm}}\right).\mathbf{10^{-9}.b}, \tag{1}$$

$$\mathbf{m_{\overline{H}}} = \pm\ \frac{\mathbf{M_S}}{\sqrt{\mathbf{3}}}.\mathbf{secB}, \tag{2}$$

where $\mathbf{b}$ - is the distance between two GNSS points in units of km; $\mathbf{B}$ - is the geodetic latitude of GNSS point; $\mathbf{M_S}$ (in units of cm) – accuracy of IGS precise ephemerides at the level of 2.5 cm (or 5 cm).

From formulas (1) and (2), we see that for the GNSS network, constructed by the static relative positioning technique, using IGS products for processing of GNSS observations in the ITRF enables very high relative horizontal position accuracy between two any GNSS points and the very high accuracy of ellipsoidal heights. The highly accurate GNSS network can be used for maintenance and improvement of the accuracy of the national horizontal and vertical reference systems. The construction of the NSRS will satisfy the abovementioned demands. For the construction of the NSRS, we can solve for the three of the following main techno-scientific tasks:

- Construction of the passive GNSS network, covering whole national territory;
- Construction of the national geoid/quasigeoid model with the accuracy at centimeter level;
- Combined adjustment of the terrestrial geodetic and passive GNSS networks in the NSRS.

With the purpose of the maintenance and the improvement of the accuracy of the national horizontal and vertical reference systems, apart from some of the CORS stations, the passive GNSS network still consists of horizontal and vertical control points which are called as ground control points and have been selected by the following criteria [1, 7]:

- Their location must satisfy requirements of a good satellite geometry and a sky visibility.
- Quick and easy access to them.
- Selected points may be located on geologically stable positions.

The passive GNSS points may have a 20–100 km density [1, 2, 6–8]. The passive GNSS networks have been built in many countries, for example High Accuracy Reference Network (USA) [33], Passive Control Network (Canada) [3, 38], Auscope GNSS Network (Australia), and so on.

Highly accurate ellipsoidal heights at the vertical control benchmarks which are derived from the processing of co-located GNSS observations in the ITRF, especially for the countries at the low and mid-latitudes, enable determining highly accurate geoid/quasi-geoid heights at those benchmarks. Those are very important data source for the determination of GNSS-leveling geoid/quasigeoid heights used for the improvement of accuracy of the national gravimetric geoid/quasi-geoid models.

Over the last decade, countries in Europe, South America, Canada, the United States of America, and so on had developed the geoid-based vertical reference systems (geopotential datum) [36, 37, 40]. An initial surface of the geopotential datum is the geoid surface with the geopotential $\mathbf{W_0}$. With usage of the geopotential datum, we have determined geopotentials of the vertical control benchmarks that will be used for the construction of the geopotential field model on the national territory or in a region. In addition to this, highly accurate ellipsoidal heights determined by the GNSS methods at the vertical control benchmarks allow calculating anomalous geopotentials of those control benchmarks which are additional data source for making more precision of spherical harmonic coefficients of the Earth Gravitational Model [21].

In [25], it is shown that in the NSRS, the relative accuracy of spatial coordinates may reach the level of 10^{-9}. Based on this criterion, in [20], it had been proved that the accuracy of the national geoid/quasi-geoid model can be improved to a level of higher than ±4 cm. At present, the national geoid/quasigeoid models in many countries, for example, AUSGeoid09 (Australia), USGG2012 (USA), CGG2013 (Canada), OSGM15 (UK), GCG2016 (Germany), and so on, have the accuracy higher than the abovementioned limitation, which guarantees to obtain orthometric/normal heights of points of interest with accuracy at the centimeter level based on the highly accurate national geoid/quasi-geoid model and results of GNSS data processing in the ITRF.

With the purpose of the maintenance and the improvement of accuracy of the national horizontal and vertical reference systems, in this chapter, we research on methods used for combined adjustment of terrestrial geodetic and passive GNSS networks, especially on a recurrent method with rotation for a combined adjustment of terrestrial geodetic and GNSS networks in the NSRS.

Although we use the terminology "combined adjustment of terrestrial geodetic and GNSS networks in the NSRS," the terrestrial geodetic network comprising horizontal and vertical control networks had been adjusted previously. Therefore, in this chapter, we understand this terminology as "combination of the results of separate adjustment of terrestrial geodetic and GNSS networks in the NSRS."

2. Methodology

2.1. Methods for combined adjustment of terrestrial geodetic and passive GNSS networks

A terrestrial geodetic network contains the national horizontal and vertical control networks that had been adjusted separately in the national horizontal and vertical reference systems. For the ground control points selected from the national horizontal and vertical control points and used for the construction of the passive GNSS network, their national ellipsoidal coordinates play very important role in solving the task of the combined adjustment of the terrestrial geodetic and the passive GNSS networks. The accuracy improvement of the national ellipsoidal coordinates (or corresponding spatial coordinates) of the abovementioned ground control points in the NSRS is the purpose of solving of the abovementioned task.

In common case, it is assumed that the national reference ellipsoid and the global reference ellipsoid are different form each other. For the national horizontal control points from results of processing of colocated GNSS observations in the ITRF according to the global reference ellipsoid, we will create relationship between the global geodetic latitudes, longitudes and the national geodetic latitudes, longitudes of these points by the Molodensky formula. This allows to obtain the national geodetic latitude, longitude of the vertical control benchmarks on which GNSS observations had been performed.

The orthometric/normal height of the national horizontal control points can be obtained by precise spirit (geometric) leveling or using a national geopotential field model with determined geopotential $\mathbf{W_0}$ of the national geoid. The first national geopotential field model in Vietnam had been declared in [23].

Such national ellipsoidal heights of the ground control points fully can be derived based on the highly accurate national geoid/quasigeoid model and the GNSS method. By such ways, we will obtain the national ellipsoidal coordinates of the ground control points, which will then be used for the calculation of approximate spatial coordinates $\mathbf{X}, \mathbf{Y}, \mathbf{Z}$ of these points in the NSRS.

In geodetic practice have been created two different directions related to development of methods for the combined adjustment of the terrestrial geodetic and GNSS networks. In the first direction, the components $\mathbf{\Delta X}, \mathbf{\Delta Y}, \mathbf{\Delta Z}$ of baseline vectors in the GNSS network have been used as pseudo-observations for the combined adjustment with different terrestrial observations on the national reference ellipsoid and for them in observation equations unknown parameters are ellipsoidal coordinate corrections and coordinate transformation parameters $\varepsilon_X, \varepsilon_Y, \varepsilon_Z, \Delta m$ [26]. In case the seven coordinate transformation parameters by Bursa-Wolf formula are known, the components $\Delta X, \Delta Y, \Delta Z$ of baseline vectors will be transformed from the ITRF to the NSRS. After that, those components $\mathbf{\Delta X}, \mathbf{\Delta Y}, \mathbf{\Delta Z}$ of baseline vectors can be transformed to $\mathbf{s}, \alpha, \mathbf{\Delta h}$, where $\mathbf{s}, \alpha$ - is length and azimuth of the geodesic; $\mathbf{\Delta h}$ - is the difference of ellipsoidal heights. The values $\mathbf{s}, \alpha, \mathbf{\Delta h}$ will be used as pseudo-observations for the combined adjustment with various terrestrial observations on the national reference ellipsoid [26, 27].

The second direction is related to the development of methods for the combined adjustment of the terrestrial geodetic and GNSS networks based on the Helmert block method by principle: a separate adjustment of the terrestrial geodetic and GNSS networks and their next combination. The separate adjustment of the passive GNSS network will be performed with two following purposes:

- Outlier detection and their removal (if they exist) in the passive GNSS network.
- Determination of highly accurate spatial coordinates of the GNSS points in the ITRF.

We will continue the research of the second direction in the following contents of this chapter.

It is assumed that the passive GNSS network consists of NP points, in which np common points (np ≤ NP) are the ground control points. In addition, these points have the approximate spatial coordinates in the NSRS presented in the form of the national spatial coordinate vector:

$$\boldsymbol{\tau} = (\mathbf{X}_1,\ \mathbf{Y}_1,\ \mathbf{Z}_1,...,\mathbf{X}_{np},\ \mathbf{Y}_{np},\ \mathbf{Z}_{np})^{\mathbf{T}} \tag{3}$$

with variance–covariance matrix $\mathbf{K}_{\tau}^{\mathbf{kxk}} = \boldsymbol{\mu}_{\tau}.\mathbf{Q}_{\tau}$, where $k = 3.np$ - order of matrix; $\boldsymbol{\mu}_{\tau}$ - RMS of the unit weight determined apriori.

Without the loss in generality, we arrange ground control points in the first orders. After the separate adjustment of the passive GNSS network in the ITRF, we obtain the adjusted spatial coordinate vector of the NP GNSS points in following form:

$$\mathbf{S} = (\overline{\mathbf{X}}_1,\ \overline{\mathbf{Y}}_1,\ \overline{\mathbf{Z}}_1,...,\overline{\mathbf{X}}_{np},\ \overline{\mathbf{Y}}_{np},\ \overline{\mathbf{Z}}_{np} \mid \overline{\mathbf{X}}_{np+1},\ \overline{\mathbf{Y}}_{np+1},\ \overline{\mathbf{Z}}_{np+1},...,\overline{\mathbf{X}}_{NP},\ \overline{\mathbf{Y}}_{NP},\ \overline{\mathbf{Z}}_{NP})^{\mathbf{T}} = (\mathbf{S}_1 \mid \mathbf{S}_2)^{\mathbf{T}}, \tag{4}$$

with variance-covariance matrix $\mathbf{K}_{\mathbf{S}} = \boldsymbol{\mu}_{\mathbf{S}}^{2}.\mathbf{R}_{\mathbf{S}}^{-1}$, where μ_S is the RMS of the unit weight and $\mathbf{R}_{\mathbf{S}}$ is the normal matrix of the order K obtained from the process of the separate adjustment of the passive GNSS network. In addition, the order K = 3.NP; $\mathbf{S}_1$ is a subvector of the spatial coordinates of the np ground control points in the ITRF; $\mathbf{S}_2$ is a subvector of the spatial coordinates of the remaining (NP – np) GNSS points in the ITRF.

In common case, for the GNSS points, the spatial coordinates $\overline{\mathbf{X}}, \overline{\mathbf{Y}}, \overline{\mathbf{Z}}$ in the ITRF are related to the spatial coordinates in the NSRS by Bursa-Wolf formula in the following form:

$$\begin{pmatrix}\mathbf{X}\\ \mathbf{Y}\\ \mathbf{Z}\end{pmatrix} = \begin{pmatrix}\overline{\mathbf{X}}\\ \overline{\mathbf{Y}}\\ \overline{\mathbf{Z}}\end{pmatrix} + \begin{pmatrix}\mathbf{X}_0\\ \mathbf{Y}_0\\ \mathbf{Z}_0\end{pmatrix} + \begin{bmatrix}\Delta\mathbf{m} & \varepsilon_{\mathbf{Z}} & -\varepsilon_{\mathbf{Y}}\\ -\varepsilon_{\mathbf{Z}} & \Delta\mathbf{m} & \varepsilon_{\mathbf{X}}\\ \varepsilon_{\mathbf{Y}} & -\varepsilon_{\mathbf{X}} & \Delta\mathbf{m}\end{bmatrix} . \begin{pmatrix}\overline{\mathbf{X}}\\ \overline{\mathbf{Y}}\\ \overline{\mathbf{Z}}\end{pmatrix}. \tag{5}$$

Now we symbolize $\boldsymbol{\omega} = (\mathbf{X}_0,\ \mathbf{Y}_0,\ \mathbf{Z}_0,\varepsilon_{\mathbf{X}},\ \varepsilon_{\mathbf{Y}},\ \varepsilon_{\mathbf{Z}},\ \Delta\mathbf{m})^{\mathbf{T}}$ as seven coordinate transformation parameters from the ITRF to the NSRS; $\tilde{\boldsymbol{\tau}}$ as vector of the adjusted spatial coordinates of the ground control points in the NSRS, which will be obtained after the combined adjustment of the terrestrial geodetic and passive GNSS networks and has the following form:

$$\tilde{\boldsymbol{\tau}} = \boldsymbol{\tau} + \boldsymbol{\delta\tau}. \tag{6}$$

where vector $\boldsymbol{\tau}$ is represented in form (3); $\boldsymbol{\delta\tau}$ - is vector of spatial coordinate corrections. $\widetilde{\mathbf{S}} = \mathbf{S} + \boldsymbol{\delta}\mathbf{S}$ as vector of the adjusted spatial coordinates of the GNSS points in the ITRF obtained after the combined adjustment of the terrestrial geodetic and passive GNSS networks. In addition, vector $\widetilde{\mathbf{S}}$ and vector of spatial coordinate corrections $\boldsymbol{\delta}\mathbf{S}$ have following forms with respect to vector **S** represented in form (4):

$$\widetilde{\mathbf{S}} = \begin{pmatrix} \widetilde{\mathbf{S}}_1 \\ \widetilde{\mathbf{S}}_2 \end{pmatrix}, \tag{7}$$

$$\delta\mathbf{S} = \begin{pmatrix} \boldsymbol{\delta}\mathbf{S}_1 \\ \boldsymbol{\delta}\mathbf{S}_2 \end{pmatrix}. \tag{8}$$

With above presented notations, for the np ground control points from formula (5) yields

$$\widetilde{\boldsymbol{\tau}} = \widetilde{\mathbf{S}}_1 + \mathbf{G}.\boldsymbol{\omega}. \tag{9}$$

where block matrix **G** with dimension NP × 7 has form:

$$\mathbf{G}_{\mathbf{NPx7}} = \begin{pmatrix} \mathbf{G}_1 \\ \mathbf{G}_2 \\ \cdot \\ \cdot \\ \mathbf{G}_{\mathbf{NP}} \end{pmatrix},$$

additionally sub-block matrix $\mathbf{G}_\mathbf{i}$ with order 3 × 7 (i = 1,2,...,NP) is represented in following form:

$$\mathbf{G}_\mathbf{i} = \begin{pmatrix} \mathbf{1} & \mathbf{0} & \mathbf{0} & \mathbf{0} & -\overline{\mathbf{Z}}_\mathbf{i} & \overline{\mathbf{Y}}_\mathbf{i} & \overline{\mathbf{X}}_\mathbf{i} \\ \mathbf{0} & \mathbf{1} & \mathbf{0} & \overline{\mathbf{Z}}_\mathbf{i} & \mathbf{0} & -\overline{\mathbf{X}}_\mathbf{i} & \overline{\mathbf{Y}}_\mathbf{i} \\ \mathbf{0} & \mathbf{0} & \mathbf{1} & -\overline{\mathbf{Y}}_\mathbf{i} & \overline{\mathbf{X}}_\mathbf{i} & \mathbf{0} & \overline{\mathbf{Z}}_\mathbf{i} \end{pmatrix}.$$

When the seven coordinate transformation parameters of Bursa-Wolf formula are unknown, the mathematical model of the combined adjustment of the terrestrial geodetic and GNSS network had been proposed in Ref. [31] in the following form:

$$\mathbf{V}_{\boldsymbol{\tau}}^{\mathbf{kx1}} = \boldsymbol{\delta\tau}^{\mathbf{kx1}}, \quad \mathbf{P}_{\boldsymbol{\tau}} = \boldsymbol{\mu}_{\mathbf{S}}^{\mathbf{2}}.\mathbf{K}_{\boldsymbol{\tau}}^{-\mathbf{1}},$$

$$\mathbf{V}_{\mathbf{S}} = \boldsymbol{\delta}\mathbf{S}^{\mathbf{Kx1}}, \quad \mathbf{P}_{\mathbf{S}} = \mathbf{R}_{\mathbf{S}}, \tag{10}$$

$$\boldsymbol{\delta}\mathbf{S}_{\mathbf{1}}^{\mathbf{kx1}} - \boldsymbol{\delta\tau}^{\mathbf{kx1}} + \mathbf{G}.\boldsymbol{\omega} + \mathbf{L} = \mathbf{0},$$

where the third condition equation in the abovementioned model is inferred from the relation (9) accounting for formulas (6), (7), (8); vector of misclosures $\mathbf{L} = \mathbf{S_1} - \boldsymbol{\tau}$.

System of observation equations (10) has K + k + 7 unknown parameters, in which there are K + k spatial coordinate corrections.

In case the approximate values of the seven coordinate transformation parameters of Bursa-Wolf formula $\boldsymbol{\omega}^{(0)} = (\mathbf{X}_0^{(0)}, \mathbf{Y}_0^{(0)}, \mathbf{Z}_0^{(0)}, \boldsymbol{\varepsilon}_{\mathbf{X}}^{(0)}, \boldsymbol{\varepsilon}_{\mathbf{Y}}^{(0)}, \boldsymbol{\varepsilon}_{\mathbf{Z}}^{(0)}, \boldsymbol{\Delta}\mathbf{m}^{(0)})^{\mathbf{T}}$ had been determined, we fully can convert vector **S** (4) from the ITRF to the NSRS and get a vector of the transformed spatial coordinates $\boldsymbol{\theta}$ of the all GNSS points in the NSRS in the following form:

$$\boldsymbol{\theta} = \begin{pmatrix} \boldsymbol{\theta}_1 \\ \boldsymbol{\theta}_2 \end{pmatrix}, \tag{11}$$

where the subvector $\boldsymbol{\theta}_1$ corresponds to the np ground control points; subvector $\boldsymbol{\theta}_2$ refers to the remaining (NP – np) GNSS points.

In this case, a difference between the vector $\boldsymbol{\tau}$ (3) and the subvector $\boldsymbol{\theta}_1$ in (11) mainly was caused by the existence of errors in the vector $\boldsymbol{\tau}$ (3) and the vector of approximate seven coordinate transformation parameters $\boldsymbol{\omega}^{(0)}$. For the task of the combined adjustment of the terrestrial geodetic and passive GNSS networks in the NSRS, when we use the vector of the spatial coordinates $\boldsymbol{\theta}$ (11) as the vector of pseudo-measurements, an improvement in the accuracy of the national spatial coordinate vector $\boldsymbol{\tau}$ (3) will be obtained due to the high accuracy of the vector $\boldsymbol{\theta}$, large number of redundant pseudo-measurements and taking account of variance–covariance matrix $\mathbf{K}_{\mathbf{S}} = \boldsymbol{\mu}_{\mathbf{S}}^{\mathbf{2}}.\mathbf{R}_{\mathbf{S}}^{-\mathbf{1}}$ of the vector $\boldsymbol{\theta}$.

We will carry out a research on the method of the combined adjustment of the terrestrial geodetic and passive GNSS networks in the NSRS proposed in [16]. In this method, the subvector $\boldsymbol{\theta}_2$ in the form of (11) will be used for the subvector of approximate spatial coordinate of the remaining (NP – np) GNSS points in the NSRS. Then taking into account vector $\boldsymbol{\tau}$ (3), the vector of the approximate spatial coordinate $\hat{\tau}$ of the all GNSS points in the NSRS has the following form:

$$\hat{\boldsymbol{\tau}} = \begin{pmatrix} \boldsymbol{\tau} \\ \boldsymbol{\theta}_2 \end{pmatrix}. \tag{12}$$

Vector of spatial coordinate correction $\boldsymbol{\delta\hat{\tau}}$ and vector of last spatial coordinate $\tilde{\hat{\boldsymbol{\tau}}} = \hat{\boldsymbol{\tau}} + \boldsymbol{\delta\hat{\tau}}$ are represented in the following forms:

$$\boldsymbol{\delta\hat{\tau}} = \begin{pmatrix} \boldsymbol{\delta\tau} \\ \boldsymbol{\delta\tau}_{\mathbf{NP-np}} \end{pmatrix}, \tag{13}$$

$$\tilde{\hat{\boldsymbol{\tau}}} = \begin{pmatrix} \tilde{\boldsymbol{\tau}} \\ \tilde{\boldsymbol{\theta}}_{\mathbf{2}} \end{pmatrix}. \tag{14}$$

With the purpose of decrease in influence of the errors in the vector of approximate seven coordinate transformation parameters $\boldsymbol{\omega}^{(0)}$ on the results of the combined adjustment of the terrestrial geodetic and passive GNSS networks in the NSRS, we will use vector of corrections $\boldsymbol{\delta\omega} = \left(\mathbf{\delta X_0, \delta Y_0, \delta Z_0}\right)^{\mathbf{T}}$ applied to transformed coordinates by formula (5). For the vector of transformed spatial coordinates $\boldsymbol{\theta}$ (11), its last value $\tilde{\boldsymbol{\theta}} = \boldsymbol{\theta} + \mathbf{V_S}$ is represented in the form:

$$\tilde{\boldsymbol{\theta}} = \begin{pmatrix} \tilde{\boldsymbol{\theta}}_{\mathbf{1}} \\ \tilde{\boldsymbol{\theta}}_{\mathbf{2}} \end{pmatrix}, \tag{15}$$

where $\mathbf{V_S}$ is the vector of corresponding spatial coordinate corrections.

From the relation

$$\tilde{\boldsymbol{\theta}} + \boldsymbol{\Omega}.\boldsymbol{\delta\omega} = \tilde{\hat{\boldsymbol{\tau}}},$$

where the block matrix $\boldsymbol{\Omega}$ with dimension NP x 3 has the form:

$$\boldsymbol{\Omega}_{\mathbf{NPx3}} = \begin{pmatrix} \mathbf{E_1} \\ \mathbf{E_2} \\ \cdot \\ \cdot \\ \mathbf{E_{NP}} \end{pmatrix}, \tag{16}$$

additionally sub-block matrix $\mathbf{E_i}$ is an unit matrix of the order of 3x3 (i = 1,2,..,NP), taking into account the formulas (11), (12), (13), (14), (15). We obtain the system of observation equations in the following form:

$$\mathbf{V_S^{Kx1}} = \boldsymbol{\delta\hat{\tau}}_{\mathbf{S}}^{\mathbf{Kx1}} - \boldsymbol{\Omega}.\boldsymbol{\delta\omega}^{\mathbf{3x1}} + \mathbf{L_S^{Kx1}},$$

where the vector of free components has the form:

$$\mathbf{L}_S^{Kx1} = \hat{\boldsymbol{\tau}} - \boldsymbol{\theta} = \begin{bmatrix} \boldsymbol{\tau} - \boldsymbol{\theta}_1 \\ \dots\dots\dots\ \dots\dots \\ \mathbf{O} \end{bmatrix},$$

O is the subvector corresponding to the subvector $\boldsymbol{\theta}_2$ and containing (K – k) zeros.

Finally, we obtain the mathematical model of the combined adjustment of the terrestrial geodetic and passive GNSS networks in the NSRS in the following form [16, 20]:

$$\begin{aligned} &\mathbf{V}_\tau^{kx1} = \delta\boldsymbol{\tau}^{kx1}, \quad \mathbf{P}_\tau = \mu_S^2.\mathbf{K}_\tau^{-1}, \\ &\mathbf{V}_S^{Kx1} = \delta\hat{\boldsymbol{\tau}}_S^{Kx1} - \boldsymbol{\Omega}.\delta\boldsymbol{\omega}^{3x1} + \mathbf{L}_S^{Kx1}, \quad \mathbf{P}_S = \mathbf{R}_S, \end{aligned} \tag{17}$$

where the vector of spatial coordinate corrections $\delta\hat{\boldsymbol{\tau}}$ has the form (13).

It should be underlined that at present we can determine the seven coordinate transformation parameters of Bursa-Wolf formula $\boldsymbol{\omega}^{(0)} = (\mathbf{X}_0^{(0)}, \mathbf{Y}_0^{(0)}, \mathbf{Z}_0^{(0)}, \boldsymbol{\varepsilon}_X^{(0)}, \boldsymbol{\varepsilon}_Y^{(0)}, \boldsymbol{\varepsilon}_Z^{(0)}, \boldsymbol{\Delta}\mathbf{m}^{(0)})^T$ with very high accuracy. In this case, the variance-covariance matrix $\mathbf{K}_S = \mu_S^2.\mathbf{R}_S^{-1}$, obtained after the separate adjustment of the passive GNSS network in the ITRF is considered to be unchanged in the process of the transformation of spatial coordinates of GNSS points from the ITRF into the NSRS. Therefore, the weight matrix $\mathbf{P}_S = \mathbf{R}_S$ is assigned to the second subsystem of observation equations in (17).

System of observation equations (17) has all K + 3 unknown parameters. A study of the method of Givens rotation for solving this system of observation equations is performed in Subsection 2.4.

2.2. Brief description of the method of recurrent adjustment of geodetic network with Givens rotation

To obtain the best linear unbiased estimate of unknown parameters by the least squares method, we must adopt an outlier detection method for geodetic observations in geodetic networks. In [29], a method of recurrent adjustment of geodetic networks had been developed, which allows for the detection of outliers in the calculation process and is realized by the following procedure: A recurrent adjustment process is performed sequentially for every measured value in combination with outlier detection method for redundant measurements. Because the method of recurrent adjustment is working with an inverse matrix **Q** related to a normal matrix **R** by the formula $\mathbf{Q} = \mathbf{R}^{-1}$, this method is called as "Q – recurrent algorithm."

First, we will investigate the method of recurrent adjustment of geodetic networks containing n independent measurements and k unknown parameters. For the *i*th measured value y_i (i = 1,2,…,n), its adjusted value $\tilde{y}_i = y_i + v_i$ is related to the adjusted vector of unknown parameters $\tilde{\mathbf{X}} = \mathbf{X}^{(0)} + \delta\mathbf{X}$ by a function $\tilde{\mathbf{y}}_{\mathbf{i}} = \varphi_{\mathbf{i}}(\tilde{\mathbf{X}})$, where $\mathbf{v}_{\mathbf{i}}$ - is correction (residual) to the *i*th measured value $\mathbf{y}_{\mathbf{i}}$; $\mathbf{X}^{(0)}$ - is vector of approximate values of the unknown parameters with dimension k × 1; $\delta\mathbf{X}$ - is vector of corrections to the vector $\mathbf{X}^{(0)}$ with dimension k × 1; k – number of unknown parameters.

After performing the Taylor linear expansion, we obtain the observation equation of the *i*th measurement $\mathbf{y}_{\mathbf{i}}$ in the following form:

$$\mathbf{v}_{\mathbf{i}} = \mathbf{a}_{\mathbf{i}}.\delta\mathbf{X}_{\mathbf{i}} + \mathbf{l}_{\mathbf{i}}^{(0)}, \tag{18}$$

according to weight $\mathbf{p}_{\mathbf{i}}$, where $\mathbf{a}_{\mathbf{i}}$ - row vector of coefficients with dimension 1 × k; $\mathbf{l}_{\mathbf{i}}^{(0)} = \varphi_{\mathbf{i}}(\mathbf{X}^{(0)}) - \mathbf{y}_{\mathbf{i}}$ - free component.

For the every *i*th measured value $\mathbf{y}_{\mathbf{i}}$, inserted in recurrent adjustment process, we will calculate an inverse matrix $\mathbf{Q}_{\mathbf{i}}$ of the order of k x k, vector of corrections $\delta\mathbf{X}_{\mathbf{i}}$ and value $\mathbf{\Phi}_{\mathbf{i}} = [\mathbf{V}^{\mathbf{T}}\mathbf{PV}]_{\mathbf{i}}$.

To start the recurrent adjustment process, we obtain:

the initial inverse matrix $\mathbf{Q}_{\mathbf{0}} = \mathbf{10}^{\mathbf{m}}.\mathbf{E}_{\mathbf{kxk}}$,

initial vector of corrections $\delta\mathbf{X}_{\mathbf{0}} = \mathbf{0}$,

initial value $\mathbf{\Phi}_{\mathbf{0}} = [\mathbf{V}^{\mathbf{T}}\mathbf{PV}]_{\mathbf{0}} = \mathbf{0}$,

where the number m is equal to 6 and $\mathbf{E}_{\mathbf{kxk}}$ is the identity matrix of the order of k × k.

It is assumed that after performing the recurrent adjustment process for (i − 1) first measured values, we have obtained the inverse matrix $\mathbf{Q}_{\mathbf{i-1}}$, vector of corrections $\delta\mathbf{X}_{\mathbf{i-1}}$ and value $\mathbf{\Phi}_{\mathbf{i-1}} = [\mathbf{V}^{\mathbf{T}}\mathbf{PV}]_{\mathbf{i-1}}$. The recurrent adjustment process for the *i*th measurement $\mathbf{y}_{\mathbf{i}}$ with the observation equation (18) will be performed by the following way:

$$\mathbf{Q}_{\mathbf{i}} = \mathbf{Q}_{\mathbf{i-1}} - \frac{\mathbf{Z}_{\mathbf{i}}^{\mathbf{T}}\mathbf{Z}_{\mathbf{i}}}{\mathbf{g}_{\mathbf{i}}},$$

$$\delta\mathbf{X}_{\mathbf{i}} = \delta\mathbf{X}_{\mathbf{i-1}} - \frac{\mathbf{Z}_{\mathbf{i}}^{\mathbf{T}}}{\mathbf{g}_{\mathbf{i}}}\mathbf{l}_{\mathbf{i}},$$

$$\mathbf{\Phi}_{\mathbf{i}} = \mathbf{\Phi}_{\mathbf{i-1}} + \frac{\mathbf{l}_{\mathbf{i}}^{\mathbf{2}}}{\mathbf{g}_{\mathbf{i}}},$$

where the vector

$$\mathbf{Z}_i^T = \mathbf{Q}_{i-1}.\mathbf{a}_i^T,$$

the free component

$$\mathbf{l}_i = \mathbf{a}_i.\delta\mathbf{X}_{i-1} + \mathbf{l}_i^{(0)}. \tag{19}$$

The number $\mathbf{g}_i$ is an inverse weight of the free component $\mathbf{l}_i$ and is calculated by the formula:

$$\mathbf{g}_i = \mathbf{p}_i^{-1} + \mathbf{a}_i.\mathbf{Z}_i^T. \tag{20}$$

The *i*th measurement $\mathbf{y}_i$ will be recognized as the redundant measurement, if number $\mathbf{g}_i$ satisfies the condition $\mathbf{g}_i \leq \frac{\mathbf{100}}{\mathbf{p}_i}$ [30]. When $\mathbf{y}_i$ is the redundant measurement, the outlier detection will be performed based on the comparison of the free component $\mathbf{l}_i$ with its limitation $(\mathbf{l}_i)_{\mathbf{lim}} = \mathbf{3}.\boldsymbol{\mu}_0.\sqrt{\mathbf{g}_i}$, where $\boldsymbol{\mu}_0$ - is the RMS error of measurements determined apriori. If $(\mathbf{l}_i)_{\mathbf{lim}} > \mathbf{l}_i$, then we have base to accept an assumption that in the first i measured values outliers exist.

In the case of the absence of any outliers in the geodetic network, after accomplishment of the recurrent adjustment process for n measurements, the vector of adjusted parameters $\tilde{\mathbf{X}}$ and the RMS error of weight unit $\boldsymbol{\mu}$ after adjustment of the geodetic network have been calculated by the following formulas:

$$\tilde{\mathbf{X}} = \mathbf{X}^{(0)} + \delta\mathbf{X}_n, \tag{21}$$

$$\boldsymbol{\mu} = \pm\sqrt{\frac{\boldsymbol{\Phi}_n}{\mathbf{n} - \mathbf{k}}}. \tag{22}$$

Although the recurrent algorithm Q has the ability to detect outliers in recurrent adjustment process, the inverse matrix **Q** is a full matrix that leads to a decrease in the efficiency of the adjustment of a large geodetic network. The method of Givens rotation becomes efficient in case of using a sparse matrix technique [12]. In [13], the usage of Givens rotation method had been proposed for the adjustment of large geodetic networks. The method of Givens rotation allows the transformation of the elements of the coefficients matrix $\mathbf{A}_{\mathbf{nxk}}$ in the system of observation equations to the elements of an upper triangular matrix $\mathbf{T}_{\mathbf{kxk}}$ related to the normal matrix **R** by the formula $\mathbf{R} = \mathbf{T}^{\mathbf{T}}\mathbf{T}$.

On an account of abilities of the method of recurrent adjustment for outlier detection in recurrent adjustment process and the method of Givens rotation for using the technique of a sparse matrix, in [15], a method of recurrent adjustment with rotation that had been constructed based on the method of Givens rotation had been proposed by using the technique of sparse matrix and has been performed in the procedure of recurrent adjustment process with outlier detection. This method is called as "T – recurrent algorithm" with an initial matrix of $\mathbf{T_0}$ of the recurrent adjustment process represented in the following form:

$$\mathbf{T_0} = \mathbf{10^{-m}.E_{kxk}}, \tag{23}$$

where the number m is equal to 6; $\mathbf{E_{kxk}}$- is identity matrix of order k; k is number of unknown parameters.

It is necessary to underline that for the method of Givens rotation, a transformation of every element of the row vector of coefficients $\mathbf{a_i}$ in the observation equation (18) requires four multiplications. For a method of fast rotation proposed in [10], the transformation of every element of the row vector of coefficients $\mathbf{a_i}$ in the observation equation (18) requires two multiplications. However using the initial matrix $\mathbf{T_0}$ (23) for starting the recurrent adjustment process, the method of fast rotation leads to an increase of the transformed elements of the upper triangular matrix $\mathbf{T_{kxk}}$. That is why in [17] it had been proposed that the method of mean rotation for that in the recurrent adjustment process the transformation of every element of the row vector of coefficients $\mathbf{a_i}$ in the observation equation (18) requires three multiplications. For the method of mean rotation, the upper triangular matrix $\mathbf{T_{kxk}}$ is represented in the form $\mathbf{T_{kxk}} = \mathbf{D.\hat{T}}$, where $\mathbf{D}$ is a diagonal matrix containing diagonal elements of the upper triangular matrix $\mathbf{T_{kxk}}$, $\mathbf{\hat{T}}$ is an upper triangular matrix with unit diagonal elements.

In this chapter, we carry out a research on the usage of T - recurrent algorithm for the recurrent adjustment of geodetic networks containing n independent values of measurements. We symbolize $\mathbf{Y}$ as the vector of transformed free components related to the vector of corrections $\mathbf{\delta X}$ by the system of equations.

$$\mathbf{T.\delta X = Y}. \tag{24}$$

For starting the recurrent adjustment process, we get the initial matrix $\mathbf{T_0}$ form (23), initial vector of transformed free components $\mathbf{Y_0 = 0}$ and initial value $\mathbf{\Phi_0 = [V^T PV]_0 = 0}$. It is assumed that after performing the recurrent adjustment process for the first (i − 1) values of measurements, we have obtained an upper triangular matrix $\mathbf{T_{i-1}}$, a vector of transformed free components $\mathbf{Y_{i-1}}$ and a value $\mathbf{\Phi_{i-1} = [V^T PV]_{i-1}}$.

For sequential insertion of the *i*th measured value $\mathbf{y_i}$ with the observation equation (18) in the recurrent adjustment process, we will create auxiliary matrix $\mathbf{B^{(0)}}$ with dimensions (k + 1) × (k + 1) in the following form ([15], [18]):

$$\mathbf{B}^{(0)} = \left[\begin{array}{c:c} \mathbf{T}_{i-1} & \mathbf{Y}_{i-1} \\ \hdashline \sqrt{\mathbf{p}_i} \cdot \mathbf{a}_i & \sqrt{\mathbf{p}_i} \cdot \mathbf{l}_i^{(0)} \end{array}\right] \tag{25}$$

We symbolize $\mathbf{b}_j$ $(j = 1,2,.., k)$ as *j*th row of matrix $\mathbf{B}^{(0)}$ (25), $\xi^{(0)}$ as $(k+1)$th row of matrix $\mathbf{B}^{(0)}$ (25). A rotation transformation will be sequentially performed from row $\mathbf{b}_1$ to row $\mathbf{b}_k$ of the matrix $\mathbf{B}^{(0)}$. It is assumed that after performing rotation transformation on first (j − 1) rows, we have got the matrix $\mathbf{B}^{(j-1)}$ with (j − 1) transformed rows and transformed $(k+1)$th row $\xi^{(j-1)}$. For the rotation transformation of *j*th row $\mathbf{b}_j$ of matrix $\mathbf{B}^{(j-1)}$, we build a rotation matrix $\mathbf{H}_j$ in underrepresented form (26). The elements $\mathbf{C}_j$ and $\mathbf{S}_j$ of the rotation matrix $\mathbf{H}_j$ are calculated by the following formulas:

$$\mathbf{C}_j = \frac{(\mathbf{b}_j)_j}{\mathbf{f}}, \quad \mathbf{S}_j = -\frac{\xi_j^{(j-1)}}{\mathbf{f}},$$

where $(\mathbf{b}_j)_j$ is the *j*th element of row $\mathbf{b}_j$; $\xi_j^{(j-1)}$ is the *j*th element of the $(k+1)$th row $\xi^{(j-1)}$; $\mathbf{f} = \sqrt{\left\{(\mathbf{b}_j)_j\right\}^2 + \left\{\xi_j^{(j-1)}\right\}^2}$.

The elements $\mathbf{C}_j$ and $\mathbf{S}_j$ of the rotation matrix $\mathbf{H}_j$ are located on the *j*th and $(k+1)$th rows as well as on the *j*th and $(k+1)$th columns as represented in form (26).

Multiplying matrix $\mathbf{B}^{(j-1)}$ on the left by the rotation matrix $\mathbf{H}_j$, we will obtain the transformed matrix $\mathbf{B}^{(j)}$ that is.

$$\mathbf{B}^{(j)} = \mathbf{H}_j.\mathbf{B}^{(j-1)} = \mathbf{H}_j.\mathbf{H}_{j-1}...\mathbf{H}_1.\mathbf{B}^{(0)}.$$

$$\mathbf{H}_j = \begin{bmatrix} 1 & 0 & .. & 0 & .. & 0 & .. & 0 \\ 0 & 1 & .. & 0 & .. & 0 & .. & 0 \\ \cdots & \cdots & \cdots & \cdots & \cdots & \cdots & \cdots & \cdots \\ 0 & 0 & .. & \mathbf{C}_j & .. & 0 & .. & -\mathbf{S}_j \\ \cdots & \cdots & \cdots & \cdots & \cdots & \cdots & \cdots & \cdots \\ 0 & 0 & ... & 0 & .. & 1 & .. & 0 \\ 0 & 0 & ... & \mathbf{S}_j & .. & 0 & .. & \mathbf{C}_j \end{bmatrix}_{(k+1)\times(k+1)} \tag{26}$$

By such a way after the accomplishment of rotation transformation of all k rows of the matrix $\mathbf{B}^{(0)}$(25), we obtain the transformed matrix

$$\tilde{\mathbf{B}} = \mathbf{B}^{(k)} = \mathbf{H}_k \cdot \mathbf{H}_{k-1} \cdots \mathbf{H}_1 \cdot \mathbf{B}^{(0)}, \tag{27}$$

which has the following form:

$$\tilde{\mathbf{B}} = \begin{bmatrix} \mathbf{T}_i & \mathbf{Y}_i \\ \mathbf{0} & \sqrt{\Delta\mathbf{\Phi}_i} \end{bmatrix}. \tag{28}$$

When $\mathbf{\Phi}_i = [\mathbf{V}^T\mathbf{PV}]_i = \mathbf{\Phi}_{i-1} + \Delta\mathbf{\Phi}_i$. With the purpose of the outlier detection for the *i*th measurement $\mathbf{y}_i$, which is a redundant measured value, we will calculate a vector $\mathbf{t}_i$ from the system $\mathbf{T}_{i-1}^T \cdot \mathbf{t}_i = \mathbf{a}_i^T$. The free component $\mathbf{l}_i$ (19) and its inverse weight $\mathbf{g}_i$ (20) are calculated by the following formulas [15, 18]:

$$\mathbf{l}_i = \mathbf{t}_i^T \cdot \mathbf{Y}_{i-1} + \mathbf{l}_i^{(0)},$$
$$\mathbf{g}_i = \mathbf{p}_i^{-1} + \mathbf{t}_i^T \cdot \mathbf{t}_i.$$

The outlier detection will then be performed by a way, analogous to the Q – recurrent algorithm. After the accomplishment of the recurrent adjustment process for the n measured values, the vector of corrections $\mathbf{\delta X}$ is calculated from the system of equations (24). The vector of adjusted parameters $\tilde{\mathbf{X}}$ and the RMS error of weight unit $\boldsymbol{\mu}$ after the adjustment of the geodetic network are then calculated by formulas (21), (22).

The correctness of the form (28), obtained from Givens rotation, can be checked by the following way [15, 18]. It is assumed that for the first (i-1) measured values in a geodetic network, we have a system of observation equations in the following form:

$$\mathbf{V}_{i-1} = \mathbf{A}_{i-1}.\delta\mathbf{X}_{i-1} + \mathbf{L}_{i-1}^{(0)} \tag{29}$$

with a weight matrix $\mathbf{P}_{i-1}$.

Solving the system of observation equations (29) by the least squares method, we obtain the system of normal equations:

$$\mathbf{R}_{i-1}.\delta\mathbf{X}_{i-1} + \mathbf{b}_{i-1} = \mathbf{0}, \tag{30}$$

where $\mathbf{R}_{i-1} = \mathbf{A}_{i-1}^T.\mathbf{P}_{i-1}.\mathbf{A}_{i-1}$ is the normal matrix and $\mathbf{b}_{i-1} = \mathbf{A}_{i-1}^T.\mathbf{P}_{i-1}.\mathbf{L}_{i-1}^{(0)}$ is the vector of free components of the system of normal equations.

After the Cholesky decomposition, the system of normal equations (30) has been transformed into a system of equivalent equations:

$$\begin{aligned} \mathbf{T}_{i-1}^{T}.\mathbf{Y}_{i-1} &= -\mathbf{b}_{i-1}, \\ \mathbf{T}_{i-1}.\delta\mathbf{X}_{i-1} &= \mathbf{Y}_{i-1}, \end{aligned} \tag{31}$$

where $\mathbf{Y}_{i-1}$ is the vector of transformed free components, $\mathbf{T}_{i-1}$ is the upper triangular matrix obtained from the Cholesky decomposition $\mathbf{R}_{i-1} = \mathbf{T}_{i-1}^{T}.\mathbf{T}_{i-1}$.

From formula (31), we can obtain the following value:

$$(\delta\mathbf{X}_{i-1}^{T}.\mathbf{b}_{i-1})^{T} = \delta\mathbf{X}_{i-1}^{T}.\mathbf{b}_{i-1} = -\mathbf{Y}_{i-1}^{T}.\mathbf{Y}_{i-1}. \tag{32}$$

On an account of the formulas (30) and (32) from (29), we will obtain a following value:

$$\mathbf{\Phi}_{i-1} = \mathbf{V}_{i-1}^{T}.\mathbf{P}_{i-1}.\mathbf{V}_{i-1} = \left(\mathbf{L}_{i-1}^{(0)}\right)^{T}.\mathbf{P}_{i-1}.\mathbf{L}_{i-1}^{(0)} - \mathbf{Y}_{i-1}^{T}.\mathbf{Y}_{i-1}. \tag{33}$$

Now after insertion of the *i*th measured value $\mathbf{y}_i$ with the observation equation (18) in the adjustment process, we will obtain some known relations:

$$\begin{aligned} \mathbf{R}_{i} &= \mathbf{T}_{i}^{T}.\mathbf{T}_{i} = \mathbf{R}_{i-1} + \mathbf{p}_{i}.\mathbf{a}_{i}^{T}.\mathbf{a}_{i} = \mathbf{T}_{i-1}^{T}.\mathbf{T}_{i-1} + \mathbf{p}_{i}.\mathbf{a}_{i}^{T}.\mathbf{a}_{i}, \\ \mathbf{T}_{i}^{T}.\mathbf{Y}_{i} &= -\mathbf{b}_{i} = -\mathbf{b}_{i-1} - \mathbf{p}_{i}.\mathbf{a}_{i}^{T}.\mathbf{l}_{i}^{(0)} = \mathbf{T}_{i-1}^{T}.\mathbf{Y}_{i-1} - \mathbf{p}_{i}.\mathbf{a}_{i}^{T}.\mathbf{l}_{i}^{(0)}. \end{aligned} \tag{34}$$

By an analogous way to formula (33), we have

$$\mathbf{\Phi}_{i} = \mathbf{V}_{i}^{T}.\mathbf{P}_{i}.\mathbf{V}_{i} = \left(\mathbf{L}_{i}^{(0)}\right)^{T}.\mathbf{P}_{i}.\mathbf{L}_{i}^{(0)} - \mathbf{Y}_{i}^{T}.\mathbf{Y}_{i}. \tag{35}$$

On an account of the relation $\left(\mathbf{L}_{i}^{(0)}\right)^{T}.\mathbf{P}_{i}.\mathbf{L}_{i}^{(0)} = \left(\mathbf{L}_{i-1}^{(0)}\right)^{T}.\mathbf{P}_{i-1}.\mathbf{L}_{i-1}^{(0)} + \mathbf{p}_{i}.(\mathbf{l}_{i}^{(0)})^{2}$, from formulas (33) and (35) will be inferred the following value:

$$\Delta\mathbf{\Phi}_{i} = \mathbf{\Phi}_{i} - \mathbf{\Phi}_{i-1} = \mathbf{p}_{i}.(\mathbf{l}_{i}^{(0)})^{2} - \mathbf{Y}_{i}^{T}.\mathbf{Y}_{i} + \mathbf{Y}_{i-1}^{T}.\mathbf{Y}_{i-1}. \tag{36}$$

Because the rotation matrix $\mathbf{H}_j$(26) is the orthogonal matrix that satisfies the condition $\mathbf{H}_{j}^{T}.\mathbf{H}_{j} = \mathbf{E}_{(k+1)x(k+1)}$, where $\mathbf{E}_{(k+1)x(k+1)}$ is the unit matrix of the order of (k + 1) × (k + 1), from formula (27), we obtain the following relationship:

$$\tilde{\mathbf{B}}^{T}.\tilde{\mathbf{B}} = (\mathbf{B}^{(0)})^{T}.\mathbf{B}^{(0)}. \tag{37}$$

Substituting $\mathbf{B}^{(0)}$ (25) and $\tilde{\mathbf{B}}$ (28) into (37), we obtain the known formulas (34) and (36). That proved the correctness of the form (28), obtained from Givens rotation after the insertion of the *i*th measured value $\mathbf{y}_i$ with the observation equation (18) in the recurrent adjustment process.

In the case outliers exist in the geodetic network, we will determine the corrections vector $\mathbf{V}^{(0)}$ for n measurements that will be used for finding outliers. A method for finding outliers is investigated in Subsection 2.3.

2.3. Method for finding outliers in the geodetic network

In case the dispersion σ of measurements has not been derived confidently and has been changed in whole measurement process, i. e. $0 \le \sigma < \infty$, errors of measurements obey a Laplace distribution [32]. In this case apart from random errors, errors of measurements still consist of gross errors and as the maximum likelihood estimate, the least absolute residuals (LAR) estimate will be established under the following L_1 - norm condition:

$$\sum_{\mathbf{i}=\mathbf{1}}^{\mathbf{n}} \left| \bar{\mathbf{v}}_{\mathbf{i}} \right| = \mathbf{min}, \tag{38}$$

where $\bar{\mathbf{v}}_{\mathbf{i}} = \sqrt{\mathbf{p}_{\mathbf{i}}}.\mathbf{v}_{\mathbf{i}}$; $\mathbf{p}_{\mathbf{i}}$ is the weight of *i*th measurement $\mathbf{y}_{\mathbf{i}}$;$\mathbf{v}_{\mathbf{i}}$ is the correction (residual) to this *i*th measurement and i = 1,2,…,n.

The LAR method is more efficient in estimating the parameters of the regression model; in the case, the data are contaminated with gross errors. The LAR method has the ability of resisting against blunders (outliers) [39]. Accounting for the popularity of the calculation schema by the least squares method, in [11] had been proposed an iteratively reweighted least squares (IRLS) method, through which condition (38) is represented in the form:

$$\sum_{\mathbf{i}=\mathbf{1}}^{\mathbf{n}} \left| \bar{\mathbf{v}}_{\mathbf{i}} \right| = \sum_{\mathbf{i}=\mathbf{1}}^{\mathbf{n}} \bar{\mathbf{p}}_{\mathbf{i}} \cdot \bar{\mathbf{v}}_{\mathbf{i}}^{\mathbf{2}} = \mathbf{min}, \tag{39}$$

where weight $\bar{\mathbf{p}}_{\mathbf{i}} = \dfrac{\mathbf{1}}{\left| \bar{\mathbf{v}}_{\mathbf{i}} \right|}$.

In [5], a convergence of the iterative calculation process by the IRLS method and a diminution of amplitude of absolute residuals after every iteration under the condition had been proven (39). The experiments show that the IRLS method allows outliers to be found reliably only for such dense geodetic networks with large number of redundant measurements such as traditional triangulation, the GNSS network and the vertical network created by leveling lines between nodal benchmarks [18].

First, we symbolize $\overline{m}$ as the number of iterations ($\overline{m}$ = 0,1,2,...). As presented in Subsection 2.2, after adjusting the geodetic network by the T- recurrent algorithm with the discovery of existence of outliers in the geodetic network, we have calculated the vector $\mathbf{V}^{(0)}$ of corrections to n measurements that will be used for the iterative adjustment of the geodetic network by the IRLS method in order to find outliers. In the $\overline{m}$th iteration, based on the condition (39) for the *i*th measurement $\mathbf{y}_{\mathbf{i}}$ the observation equation (18) will be expressed in the following form:

$$\bar{\mathbf{v}}_{\mathbf{i}}^{(\bar{\mathbf{m}})} = \bar{\mathbf{a}}_{\mathbf{i}}.\delta \mathbf{X}_{\mathbf{i}}^{(\bar{\mathbf{m}})} + \bar{\mathbf{l}}_{\mathbf{i}}^{(0)} \tag{40}$$

with weight $\bar{\mathbf{p}}_{\mathbf{i}}^{(\bar{\mathbf{m}})} = \dfrac{1}{\left|\bar{\mathbf{v}}_{\mathbf{i}}^{(\bar{\mathbf{m}}-1)}\right|}$ ’ where $\bar{\mathbf{a}}_{\mathbf{i}} = \sqrt{\mathbf{p}_{\mathbf{i}}}.\mathbf{a}_i$ is the row vector of coefficients; $\bar{\mathbf{l}}_{\mathbf{i}}^{(0)} = \sqrt{\mathbf{p}_{\mathbf{i}}}.\mathbf{l}_{\mathbf{i}}^{(0)}$ is the free component; $\bar{\mathbf{v}}_{\mathbf{i}}^{(\bar{\mathbf{m}}-1)} = \sqrt{\mathbf{p}_{\mathbf{i}}}.\mathbf{v}_{\mathbf{i}}^{(\bar{\mathbf{m}}-1)}$, and $\mathbf{v}_{\mathbf{i}}^{(\bar{\mathbf{m}}-1)}$ are the correction for the *i*th measurement $\mathbf{y}_{\mathbf{i}}$ which is obtained in previous ($\bar{m}-1$) th iteration; $\mathbf{p}_{\mathbf{i}}$ is the weight of the *i*th measurement $\mathbf{y}_{\mathbf{i}}$.

The observation equation (40) will be sequentially inserted in the recurrent adjustment process by the T- recurrent algorithm. After the accomplishment of $\bar{m}$th iterative recurrent adjustment of the geodetic network with n measured values, we will calculate the vector of the adjusted parameters $\tilde{\mathbf{X}}^{(\bar{\mathbf{m}})}$ in the $\bar{m}$th iteration by the formula $\tilde{\mathbf{X}}^{(\bar{\mathbf{m}})} = \mathbf{X}^{(0)} + \delta \mathbf{X}^{(\bar{\mathbf{m}})}$. The vector $\tilde{\mathbf{X}}^{(\bar{\mathbf{m}})}$ will be used for the determination of the vector $\mathbf{V}^{(\bar{\mathbf{m}})}$ of corrections to n measured values serving next ($\bar{m}$ +1) th iterative recurrent adjustment of the geodetic network.

A process of the iterative recurrent adjustment of the geodetic network will be ended, if in two ($\bar{m}$ -1)th and $\bar{m}$th adjacent iterations for all residuals satisfy the following condition:

$$\left|\left|\mathbf{v}^{(\mathbf{m})}\right| - \left|\mathbf{v}^{(\mathbf{m}-1)}\right|\right| \le \boldsymbol{\varepsilon},$$

where ε is a small positive number. The outliers can be found from the measured values which have the largest residuals (corrections).

2.4. Application of the recurrent adjustment method with Givens rotation for separate adjustment of GNSS network in the ITRF and next its combination to the NSRS

For the GNSS network comprising NP GNSS points, the components $\mathbf{\Delta X}$, $\mathbf{\Delta Y}$, $\mathbf{\Delta Z}$ of baseline vectors are used as pseudo-observations for the adjustment of this network. It is assumed that the GNSS network contains N baseline vectors. We symbolize $\bar{\mathbf{Y}}_{\mathbf{i}}$ (i = 1,2,..., N) as the vector of pseudo-observations between two GNSS points $\mathbf{s},\mathbf{h}$. Additionally,

$$\bar{\mathbf{Y}}_{\mathbf{i}} = \begin{bmatrix} \mathbf{\Delta X}_{\mathbf{i}} \\ \mathbf{\Delta Y}_{\mathbf{i}} \\ \mathbf{\Delta Z}_{\mathbf{i}} \end{bmatrix} \tag{41}$$

with variance-covariance matrix $\mathbf{C}_{\mathbf{i}}$ of the order of 3. That means that $\mathbf{\Delta X}_{\mathbf{i}}$, $\mathbf{\Delta Y}_{\mathbf{i}}$, $\mathbf{\Delta Z}_{\mathbf{i}}$ are dependent observations to which the system of observation equations corresponds in the following form:

$$\mathbf{V_i} = \mathbf{A_i}.\delta\mathbf{H_i} + \mathbf{L_i}^{(0)}, \tag{42}$$

where $\mathbf{V_i}$ is a vector of corrections (residuals) to the measured values $\Delta\mathbf{X_i}$, $\Delta\mathbf{Y_i}$, $\Delta\mathbf{Z_i}$ in the vector of pseudo-observations $\overline{\mathbf{Y}}_\mathbf{i}$ (41). The matrix of coefficients with dimension 3 x K (K = 3. NP – total number of unknown parameters in the GNSS network) has the form:

$$\mathbf{A_i} = \begin{bmatrix} \mathbf{a_1} \\ \mathbf{a_2} \\ \mathbf{a_3} \end{bmatrix},$$

additionally $\mathbf{a_1} = (-1\ 0\ 0\ \ldots\ 1\ 0\ 0)$, $\mathbf{a_2} = (0\ -1\ 0\ \ldots\ 0\ 1\ 0)$, $\mathbf{a_3} = (0\ 0\ -1\ldots\ 0\ 0\ 1)$; $\delta\mathbf{H_i}$ is a vector of unknown corrections to approximate spatial coordinates of GNSS points in the ITRF, obtained after the insertion of *i*th vector of pseudo-observations $\overline{\mathbf{Y}}_\mathbf{i}$ (41) in the recurrent adjustment process; $\mathbf{L_i}^{(0)}$ is a vector of free components which has form:

$$\mathbf{L_i}^{(0)} = \begin{bmatrix} \mathbf{X_h}^{(0)} - \mathbf{X_s}^{(0)} - \Delta\mathbf{X_i} \\ \mathbf{Y_h}^{(0)} - \mathbf{Y_s}^{(0)} - \Delta\mathbf{Y_i} \\ \mathbf{Z_h}^{(0)} - \mathbf{Z_s}^{(0)} - \Delta\mathbf{Z_i} \end{bmatrix},$$

where $\mathbf{X_s}^{(0)}, \mathbf{Y_s}^{(0)}, \mathbf{Z_s}^{(0)}$ and $\mathbf{X_h}^{(0)}, \mathbf{Y_h}^{(0)}, \mathbf{Z_h}^{(0)}$ are the approximate spatial coordinates of the GNSS **s** and **h**.

A weight matrix $\mathbf{P_i}$ of the order 3 is assigned to the vector of pseudo-observations $\overline{Y}_i$ (41) and represented in form:

$$\mathbf{P_i} = \boldsymbol{\mu}_\mathbf{0}^\mathbf{2} \cdot \mathbf{C_i}^{-1}, \tag{43}$$

where $\boldsymbol{\mu}_\mathbf{0}$ is the RMS of unit weight determined apriori.

As we had seen in Subsection 2.2, with the purpose of outlier detection, the recurrent adjustment method is effectively realized for independent observations. The components $\Delta\mathbf{X_i}$, $\Delta\mathbf{Y_i}$, $\Delta\mathbf{Z_i}$ are the dependent observations. Therefore, for the application of the recurrent adjustment method, we must transform the dependent observations $\Delta\mathbf{X_i}$, $\Delta\mathbf{Y_i}$, $\Delta\mathbf{Z_i}$ to the independent ones. For that, we represent the weight matrix $\mathbf{P_i}$ in the form $\mathbf{P_i} = \mathbf{U_i^T}.\mathbf{U_i}$, and the system of observation equations (42) will be expressed as [20]:

$$\overline{\mathbf{V}}_{\mathbf{i}} = \overline{\mathbf{A}}_{\mathbf{i}}.\delta\mathbf{H}_{\mathbf{i}} + \overline{\mathbf{L}}_{\mathbf{i}}^{(0)}, \tag{44}$$

where $\overline{\mathbf{V}}_{\mathbf{i}} = \mathbf{U}_{\mathbf{i}}.\mathbf{V}_{\mathbf{i}}$, $\overline{\mathbf{A}}_{\mathbf{i}} = \mathbf{U}_{\mathbf{i}}.\mathbf{A}_{\mathbf{i}}$, $\overline{\mathbf{L}}_{\mathbf{i}}^{(0)} = \mathbf{U}_{\mathbf{i}}.\mathbf{L}_{\mathbf{i}}^{(0)}$.

By such a way, the system of observation equations (44) has a unit weight matrix $\overline{\mathbf{P}}_{\mathbf{i}} = \mathbf{E}_{\mathbf{3x3}}$, where $\mathbf{E}_{\mathbf{3x3}}$ is the unit matrix of the order of 3 x 3. In [20], an algorithm for a transformation of a matrix $\frac{1}{\mu_0^2}\cdot\mathbf{C}_{\mathbf{i}}$ in formula (43) to an upper triangular matrix $\mathbf{U}_{\mathbf{i}}$ of the order of 3 had been proposed by the following way. We arrange the elements of the matrix $\frac{1}{\mu_0^2}\cdot\mathbf{C}_{\mathbf{i}}$ in turn by columns in array **C** of length 6. After the performance of operations sequentially by the below represented procedure:

$$\mathbf{C(6) = 1/\sqrt{C(6)};\quad C(5) = C(5).C(6);\quad C(4) = C(4).C(6);}$$

$$\mathbf{C(3) = \frac{1}{\sqrt{C(3) - C(5)^2}};\quad C(2) = \left[C(2) - C(4).C(5)\right].C(3);}$$

$$\mathbf{C(1) = \frac{1}{\sqrt{C(1) - C(2)^2 - C(4)^2}};\quad C(2) = -C(1).C(2).C(3);}$$

$$\mathbf{C(4) = -\left[C(1).C(4) + C(2).C(5)\right].C(6);\quad C(5) = -C(3).C(5).C(6),}$$

we will obtain corresponding elements of the upper triangular matrix $\mathbf{U}_{\mathbf{i}}$ arranged by columns.

Before the separate adjustment of the GNSS network, we ought to choose one GNSS point to be "a fixed point" that has spatial coordinates in both the ITRF and the NSRS. Without losing generality, this fixed point is numbered with the number sign 1. Based on a method of a temporary fixation of an initial point, proposed in [18], an inverse weight matrix $\overline{\mathbf{Q}}_{\mathbf{F}}$ of the spatial coordinates of the fixed point in the ITRF is accepted to be $\mathbf{10^{-2m}.E_{3x3}}$, that is.

$$\overline{\mathbf{Q}}_{\mathbf{F}} = \mathbf{10^{-2m}.E_{3x3}}, \tag{45}$$

where number m is equal to 6, $\mathbf{E}_{\mathbf{3x3}}$-unit matrix of the order of 3 × 3.

The choice of a fixed point guarantees the nonsingularity of normal matrix obtained in a process of the adjustment of the GNSS network. Below, we will prove that after the combined adjustment of terrestrial geodetic and GNSS networks, the temporary fixation of the initial point will be automatically eliminated.

To start the separate adjustment of the GNSS network in the ITRF, on an account of formula (45), we obtain an initial upper triangular matrix $(\mathbf{T_S})_0$ of the order of K for the recurrent adjustment process in the following form:

$$(\mathbf{T_S})_0 = \begin{bmatrix} \mathbf{10^m.E_{3x3}} & \mathbf{0} \\ \mathbf{0} & \mathbf{10^{-m}.E_{(K-3)x(K-3)}} \end{bmatrix}.$$

The recurrent adjustment process will be realized by the T- recurrent algorithm sequentially for every observation equation from the system of observation equations (44). The outlier detection will be performed if the *i*th vector of pseudo-observations $\overline{\mathbf{Y}}_\mathbf{i}$ (41) is redundant.

After the accomplishment of the separate adjustment of the GNSS network with the insertion of all N vectors of pseudo-observations in the form (41) in the recurrent adjustment process by the T-recurrent algorithm, if outliers are encountered in the network, we will perform outlier detection using the method represented in Subsection 2.3.

If the GNSS network does not contain outliers, the obtained upper triangular matrix $\mathbf{T_S} = (\mathbf{T_S})_\mathbf{N}$ of the order of K will be related to the normal matrix $\mathbf{R_S}$ in the system of observation equations (17) by the formula $\mathbf{R_S} = \mathbf{T_S^T.T_S}$. Therefore for the combined adjustment of the terrestrial geodetic and GNSS networks with the solving of the system of observation equations (17) by the T-recurrent algorithm, second subsystem of observation equations in (17) will be expressed in the form:

$$\overline{\mathbf{V}}_\mathbf{S}^\mathbf{Kx1} = \mathbf{T_S}.\boldsymbol{\delta}\hat{\boldsymbol{\tau}}_\mathbf{S}^\mathbf{Kx1} - \overline{\boldsymbol{\Omega}}.\delta\boldsymbol{\omega}^\mathbf{3x1} + \overline{\mathbf{L}}_\mathbf{S}^\mathbf{Kx1}, \tag{46}$$

where $\overline{\mathbf{V}}_\mathbf{S}^\mathbf{Kx1} = \mathbf{T_S}.\mathbf{V}_\mathbf{S}^\mathbf{Kx1}$; $\overline{\boldsymbol{\Omega}} = \mathbf{T_S}.\boldsymbol{\Omega}$; $\overline{\mathbf{L}}_\mathbf{S} = \mathbf{T_S}.\mathbf{L_S}$; $\mathbf{T_S}$ is the upper triangular matrix obtained from the separate adjustment of the GNSS network in the ITRF.

The usage of the T-recurrent algorithm for solving the system of observation equations (17) has the remarkable advantage of being very simple for solving the subsystem of observation equations (46), created based on the transformation of the results of the separate adjustment of the GNSS network from the ITRF into the NSRS.

The subsystem of observation equations (46) has a unit weight matrix $\overline{\mathbf{P}}_\mathbf{S} = \mathbf{E_{KxK}}$ of the order of K. To start the combined adjustment of the terrestrial geodetic and GNSS networks in the NSRS by the T-recurrent algorithm, we obtain an initial upper triangular matrix $\mathbf{T_0}$ with the order of K + 3 of the recurrent adjustment process in the following form:

$$\mathbf{T}_{0} = \begin{bmatrix} \mathbf{T}_{\tau}^{\mathbf{kxk}} & \mathbf{0} \\ \mathbf{0} & \mathbf{10}^{-\mathbf{m}}.\mathbf{E}_{\overline{\mathbf{K}}\mathbf{x}\overline{\mathbf{K}}} \end{bmatrix}, \tag{47}$$

where an upper triangular matrix $\mathbf{T}_{\tau}^{\mathbf{kxk}}$ is related to weight matrix $\mathbf{P}_{\tau}$ of the first subsystem of observation equations in (17) by the formula $\mathbf{P}_{\tau} = \mathbf{T}_{\tau}^{\mathbf{T}}.\mathbf{T}_{\tau}$ order $\overline{\mathbf{K}} = \mathbf{K} + \mathbf{3} - \mathbf{k}.$

The task of the combined adjustment of the terrestrial geodetic and GNSS networks in the NSRS will be performed by the T-recurrent algorithm based on a sequential insertion of observation equations from the subsystem of observation equations (46) in the recurrent adjustment process with the usage of the initial matrix $\mathbf{T}_0$(47). Because the outlier detection in the GNSS network had been performed in the process of the separate adjustment of this network, then in the process of solving the abovementioned task, the outlier detection will be performed for the data of terrestrial geodetic network. The results of the combined adjustment of the terrestrial geodetic and GNSS networks in the NSRS will be performed by the T-recurrent algorithm determined by the formulas (21), (22), (24) represented in Subsection 2.2.

For the end of this subsection, we prove that performing the separate adjustment of the GNSS network in the ITRF, the temporary fixation of an initial point by assigning the inverse matrix $\overline{\mathbf{Q}}`_{\mathbf{F}}$(45) to the spatial coordinates of the fixed point will be automatically eliminated after the combined adjustment of the terrestrial geodetic and GNSS networks.

It is assumed that for all N baseline vectors in the GNSS network, a system consisting of 3.N observation equations has been created in the following form:

$$\mathbf{V} = \mathbf{A}.\delta\mathbf{H} + \mathbf{L}^{(0)} \tag{48}$$

with weight matrix **P**.

Solving the system of observation equations (48) under condition $\mathbf{V}^{\mathbf{T}}\mathbf{PV} = \mathbf{min}$, we obtain a normal matrix $\hat{\mathbf{R}}_{\mathbf{S}} = \mathbf{A}^{\mathbf{T}}\mathbf{PA}$. If in the GNSS network there is not any fixed point, that is, the GNSS network becomes the free network, then the normal matrix $\hat{\mathbf{R}}_{\mathbf{S}}$ will be singular due to the rank defect d = 3. In this case, the matrix of coefficients $\mathbf{A}$ with dimension 3.N × K has the rank defect d = 3 and satisfies the condition:

$$\mathbf{A}.\mathbf{\Omega} = \mathbf{0}, \tag{49}$$

where matrix $\mathbf{\Omega}$ has the form (16) with K = 3.NP rows and 3 columns.

For the strict separate adjustment of the GNSS network in the ITRF and avoiding the singularity of the normal matrix $\hat{\mathbf{R}}_{\mathbf{S}}$, on an account of the formula (45), we performed the above represented method of the temporary fixation of initial point with an additional usage of system of observation equations $V_F = E_1.\delta H_1$ to which the weight matrix $P_F = \overline{Q}_F^{-1} = 10^{2m}.E_{3x3}$ has been assigned, where E_1 is the unit matrix of the order of 3; δH_1 is the subvector of corrections to the spatial coordinates of the fixed point with number sign 1 of the GNSS network. In this case the separate adjustment of the GNSS network in the ITRF will be accomplished based on simultaneous solving the above mentioned system of observation equations with the system of observation equations (48) under the condition $V_F^T P_F V_F + V^T P V = \mathbf{min}$. As a result, we obtain the normal matrix.

$$R_S = \hat{R}_S + \hat{P}_F, \tag{50}$$

where the matrix $\hat{P}_F$ has the form:

$$\hat{P}_F = \begin{bmatrix} P_F^{3x3} & 0 \\ 0 & 0 \end{bmatrix}_{KxK} \tag{51}$$

As mentioned in Subsection 2.1, the normal matrix R_S (50) is used as the weight matrix P_S assigned to the second subsystem of observation equations in (17).

On an account of (49), the product $\hat{R}_S.\Omega = 0$. When we get relationship from (50):

$$R_S.\Omega = \hat{P}_F.\Omega = \begin{bmatrix} P_F & 0 & ...0 \end{bmatrix}^T. \tag{52}$$

Therefrom we infer the equality:

$$\Omega^T.R_S.\Omega = \Omega^T.\hat{P}_F.\Omega = P_F \tag{53}$$

Now performing the combined adjustment of the terrestrial geodetic and GNSS networks in the NSRS with solving the system of observation equations (17) under the condition $V_\tau^T.P_\tau.V_\tau + V_S^T.P_S.V_S = V_\tau^T.P_\tau.V_\tau + V_S^T.R_S.V_S = \mathbf{min}$, where normal matrix R_S has the form (50), we obtain a system of normal equations in the following form:

$$\begin{bmatrix} \Omega^T.R_S.\Omega & \vdots & -\Omega^T.R_S \\ \cdots\cdots\cdots & \cdots\cdots & \cdots\cdots\cdots \\ -R_S.\Omega & \vdots & \hat{P}_\tau + R_S \end{bmatrix} . \begin{bmatrix} \delta\omega \\ \cdots \\ \delta\hat{\tau}_S \end{bmatrix} + \begin{bmatrix} -\Omega^T.R_S.L_S \\ \cdots\cdots \\ R_S.L_S \end{bmatrix} = 0 \tag{54}$$

Additionally, the matrix $\hat{P}_\tau$ has the form:

$$\hat{\mathbf{P}}_{\tau} = \begin{bmatrix} \mathbf{P}_{\tau}^{\mathbf{kxk}} & \mathbf{0} \\ \mathbf{0} & \mathbf{0} \end{bmatrix}_{\mathbf{KxK}}.$$

For the system of normal equations (54), substituting $\boldsymbol{\delta\omega} = \left(\boldsymbol{\Omega}^{\mathbf{T}}.\mathbf{R}_{\mathbf{S}}.\boldsymbol{\Omega}\right)^{-1}.\boldsymbol{\Omega}^{\mathbf{T}}.\mathbf{R}_{\mathbf{S}}.(\boldsymbol{\delta}\hat{\boldsymbol{\tau}}_{\mathbf{S}} + \mathbf{L}_{\mathbf{S}})$ inferred from the first subsystem of normal equations into the second subsystem of normal equations, we will obtain a transformed system of normal equations in the form:

$$\left[\hat{\mathbf{P}}_{\tau} + \mathbf{R}_{\mathbf{S}} - \mathbf{R}_{\mathbf{S}}.\boldsymbol{\Omega}\left(\boldsymbol{\Omega}^{\mathbf{T}}.\mathbf{R}_{\mathbf{S}}.\boldsymbol{\Omega}\right)^{-1}.\boldsymbol{\Omega}^{\mathbf{T}}.\mathbf{R}_{\mathbf{S}}\right].\boldsymbol{\delta}\hat{\boldsymbol{\tau}}_{\mathbf{S}} + \left[\mathbf{R}_{\mathbf{S}} - \mathbf{R}_{\mathbf{S}}.\boldsymbol{\Omega}\left(\boldsymbol{\Omega}^{\mathbf{T}}.\mathbf{R}_{\mathbf{S}}.\boldsymbol{\Omega}\right)^{-1}.\boldsymbol{\Omega}^{\mathbf{T}}.\mathbf{R}_{\mathbf{S}}\right].\mathbf{L}_{\mathbf{S}} = \mathbf{0}. \quad (55)$$

On an account of the formulas (16), (50), (51), (52), (53) we obtain:

$$\mathbf{R}_{\mathbf{S}} - \mathbf{R}_{\mathbf{S}}.\boldsymbol{\Omega}\left(\boldsymbol{\Omega}^{\mathbf{T}}.\mathbf{R}_{\mathbf{S}}.\boldsymbol{\Omega}\right)^{-1}.\boldsymbol{\Omega}^{\mathbf{T}}.\mathbf{R}_{\mathbf{S}} = \hat{\mathbf{R}}_{\mathbf{S}} + \hat{\mathbf{P}}_{\mathbf{F}} - \hat{\mathbf{P}}_{\mathbf{F}}.\boldsymbol{\Omega}.\mathbf{P}_{\mathbf{F}}^{-1}.\boldsymbol{\Omega}^{\mathbf{T}}.\hat{\mathbf{P}}_{\mathbf{F}}^{\mathbf{T}} = \hat{\mathbf{R}}_{\mathbf{S}} + \hat{\mathbf{P}}_{\mathbf{F}} - \hat{\mathbf{P}}_{\mathbf{F}} = \hat{\mathbf{R}}_{\mathbf{S}}. \quad (56)$$

Finally, substituting (56) into (55), we obtain the following system of normal equations:

$$\left(\hat{\mathbf{P}}_{\tau} + \hat{\mathbf{R}}_{\mathbf{S}}\right).\boldsymbol{\delta}\hat{\boldsymbol{\tau}}_{\mathbf{S}} + \hat{\mathbf{R}}_{\mathbf{S}}.\mathbf{L}_{\mathbf{S}} = \mathbf{0},$$

in which the effect of the temporary fixation of an initial point, made in the process of the separate adjustment of the GNSS network in the ITRF, fully has been eliminated.

It can be concluded that the usage of the method of the temporary fixation of initial point for the strict separate adjustment of the GNSS network in the ITRF and avoiding the singularity of the normal matrix $\hat{\mathbf{R}}_{\mathbf{S}}$ does not cause any influence on the results of the combined adjustment of the terrestrial geodetic and GNSS networks in the NSRS. Moreover, this method allows the spatial coordinates of the initial point be corrected after the abovementioned combined adjustment. We will lose valuable priori information regarding the spatial coordinates of the initial point of the GNSS network for the accuracy improvement of the national spatial coordinates of GNSS points in the NSRS, if the spatial coordinates of the abovementioned initial point of the GNSS network are considered to be nonerroneous.

3. Experimental results

3.1. Data

In [22], the results of the construction of the initial national spatial reference system VN2000–3D on the base of the orientation of the WGS84 ellipsoid to best fit it to the Hon Dau local quasigeoid at tide gauge Hon Dau with using the most stable 164 colocated GPS observations performed at the first- and second-order benchmarks had been presented. The GPS data had been processed in the ITRF2008 in the period 2009–2010. The coordinate transformation parameters from the ITRF to the VN2000–3D have the following values:

$$X_0 = 204{,}511083\,m,\;\; Y_0 = 42{,}192468\ m,\;\; Z_0 = 111{,}417880\ m,$$

$$\varepsilon_X = -0''.011168229,\; \varepsilon_Y = 0''.085600577,\; \varepsilon_Z = -0''.400462723,\; \Delta m = 0.$$

In [24], the results of the construction of the initial national quasigeoid model VIGAC2017 with the accuracy level of ±5.8 cm had been presented.

From 11 to 14 November 2013, Vietnam Institute of Geodesy and Cartography (VIGAC) had accomplished four sessions of 24 h GPS observations at 11 points of the GPS network in the North Vietnam (see **Figure 1**). Average distance between GPS points is 105 km. The GPS data had been processed in the ITRF2008 by the software Bernese v. 5.2 using IGS service products.

The GPS network has five common (ground control) points C052, C022, C045, C033, C004, that have the approximate national spatial coordinates in VN2000–3D (see **Table 1**) and have been numbered sequentially from 1 to 5. In Vietnam, horizontal coordinates of geodetic points are determined in VN2000-2D, and their normal heights are determined in national the vertical reference system Haiphong1972 (HP72). On an account of the national quasigeoid model VIGAC2017, the RMS of the national ellipsoidal coordinates of the geodetic points had been considered equal to $m_B = 0''.002;\ \ m_L = 0''.0015;\ \ m_H = 0.097\ \ m$ After expressing the $m_B,\ \ m_L$ in the radian unit, we had created the variance–covariance matrix $\mathbf{K}^{\mathbf{3x3}}_{\mathbf{B,L,H}}$, that is considered equivalent to the abovementioned five common points. From that for every common point, we had created the variance–covariance matrix $\mathbf{K}^{\mathbf{3x3}}_{\mathbf{XYZ}} = \chi.\mathbf{K}^{\mathbf{3x3}}_{\mathbf{B,L,H}}.\chi^{\mathbf{T}}$, where.

$$\chi = \begin{bmatrix} -(\rho_M + H).\sin B.\cos L & -(\rho_N + H).\cos B.\sin L & \cos B.\cos L \\ -(\rho_M + H).\sin B.\sin L & (\rho_N + H).\cos B.\cos L & \cos B.\sin L \\ (\rho_M + H).\cos B & 0 & \sin B \end{bmatrix},$$

ρ_M is the radius of curvature in the meridian plane; ρ_N is the radius of curvature in the first vertical plane.

On the basis of the algorithm of transformation of the variance-covariance matrix to the upper triangular matrix, represented in Subsection 2.4, we had got the upper triangular matrices for five common points in the NSRS in the following forms:

$$T_1 = \begin{bmatrix} 0.112997 & -0.291820 & -0.678800 \\ 0 & 0.057843 & 0.179161 \\ 0 & 0 & 0.074068 \end{bmatrix}; \quad T_2 = \begin{bmatrix} 0.112708 & -0.2999733 & -0.713919 \\ 0 & 0.057491 & 0.182105 \\ 0 & 0 & 0.074403 \end{bmatrix}$$

$$T_3 = \begin{bmatrix} 0.112522 & -0.287024 & -0.680706 \\ 0 & 0.057661 & 0.182140 \\ 0 & 0 & 0.074355 \end{bmatrix}; \quad T_4 = \begin{bmatrix} 0.113212 & -0.306647 & -0.716235 \\ 0 & 0.057659 & 0.179026 \\ 0 & 0 & 0.074115 \end{bmatrix}$$

$$T_5 = \begin{bmatrix} 0.113795 & -0.325441 & -0.750297 \\ 0 & 0.057674 & 0.176483 \\ 0 & 0 & 0.073903 \end{bmatrix}.$$

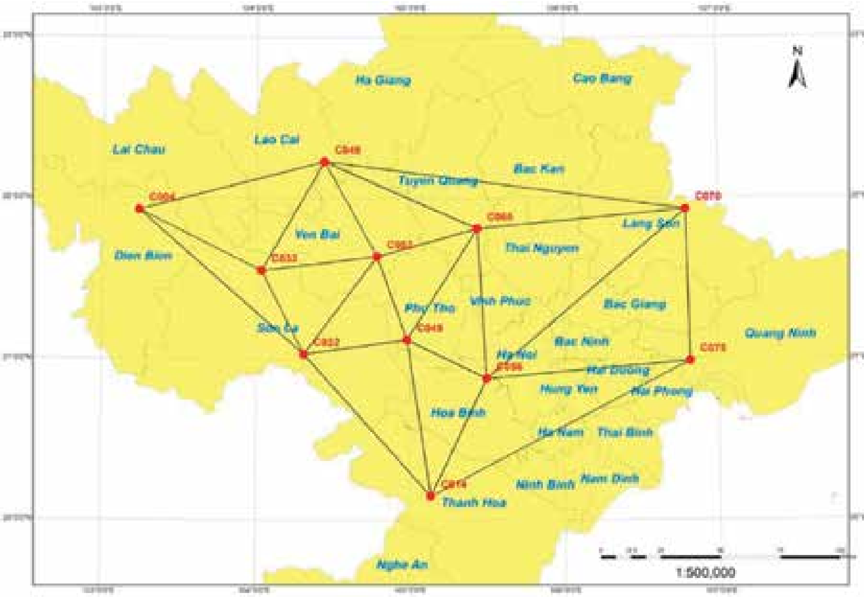

Figure 1. The GPS network in the North Vietnam.

No	Common (ground control) points	Approximate spatial coordinates in VN2000–3D		
		$X_\tau^{(0)}$ (m)	$Y_\tau^{(0)}$ (m)	$Z_\tau^{(0)}$ (m)
1	C052	−1513714.136	5735121.344	2337092.916
2	C022	−1472179.244	5771490.833	2274632.893
3	C045	−1538604.244	5750184.813	2283824.080
4	C033	−1439254.798	5758082.515	2328258.441
5	C004	−1355466.287	5762595.502	2367026.391

Table 1. Approximate national spatial coordinates of the ground control points C052, C022, C045, C033, C004 in VN2000–3D.

These upper triangular matrices will be used for creating the submatrix T_τ^{15x15} in the initial upper triangular matrix T_0 in the form (36) with the purpose of the combined adjustment of the GPS network, shown in **Figure 1**, into VN2000–3D.

3.2. Results

In [28], the experiments of the combined adjustment of the GPS network, shown in **Figure 1**, in VN2000–3D had been accomplished. The GPS network had been adjusted separately in the ITRF2008 by the T-recurrent algorithm with the temporary fixation of an initial point for GPS point C052. The adjusted spatial coordinates of all 11 GPS points had been transformed from the ITRF2008 to VN2000–3D (see **Table 2**).

The last spatial coordinates of all 11 GPS points in VN2000–3D obtained after the combined adjustment of the GPS network in VN2000–3D based on insertion of the system of observation equations in the recurrent adjustment process by the T–recurrent algorithm are shown in **Table 3**.

No	Points	$X_\theta^{(0)}$ (m)	$Y_\theta^{(0)}$ (m)	$Z_\theta^{(0)}$ (m)
1	C052	−1513714.080	5735121.312	2337092.905
2	C022	−1472179.140	5771490.861	2274632.888
3	C045	−1538604.194	5750184.888	2283824.115
4	C033	−1439254.730	5758082.565	2328258.478
5	C004	−1355466.208	5762595.543	2367026.437
6	C049	−1473387.470	5720475.157	2397685.449
7	C065	−1576880.962	5710639.604	2355075.723
8	C056	−1592782.951	5745126.896	2259055.940
9	C014	−1564014.757	5782717.956	2183131.028
10	C075	−1723353.397	5702825.750	2270215.032
11	C070	−1710134.998	5667162.050	2367393.077

Table 2. Spatial coordinates of all 11 GPS points had been transformed from the ITRF2008 to VN2000–3D.

No	Points	$\tilde{X}$ (m)	$\tilde{Y}$ (m)	$\tilde{Z}$ (m)
1	C052	−1513714.150	5735121.372	2337092.873
2	C022	−1472179.207	5771490.916	2274632.850
3	C045	−1538604.253	5750184.910	2283824.046
4	C033	−1439254.784	5758082.567	2328258.392
5	C004	−1355466.267	5762595.567	2367026.370
6	C049	−1473387.532	5720475.185	2397685.386
7	C065	−1576881.025	5710639.642	2355075.670
8	C056	−1592783.012	5745126.934	2259055.888
9	C014	−1564014.818	5782717.991	2183130.973
10	C075	−1723353.458	5702825.780	2270214.971
11	C070	−1710135.062	5667162.086	2367393.020

Table 3. Final spatial coordinates of all 11 GPS points in VN2000–3D after the combined adjustment of the GPS network.

The mean values of the RMS of national ellipsoidal coordinates of GPS points after solving the task of the combined adjustments of the GPS network in VN2000–3D are equal to $m_{\tilde{B}} = 0''.0007;\ m_{\tilde{L}} = 0''.0005;\ m_{\tilde{H}} = 0.023\ m.$ That confirmed the significant improvement of positional accuracy of the GNSS points in the NSRS after solving of the task of the combined adjustments of the GNSS network in the NSRS.

4. Conclusions

A tendency of construction of the NSRS strongly is promoted in many countries in the world due to development of the passive GNSS networks, comprising the ground control points and some CORS stations, based on the GNSS methods and results of building of the highly accurate national geoid/quasigeoid models at the centimeter level of accuracy thanks to detailed gravimetric data and the Earth gravitational models with high resolution.

From demands of usage of the high accurate spatial coordinates of GNSS points in the ITRF for different geodetic applications and next their usage for the construction of the national spatial reference frame has been arisen techno-scientific task of the separate adjustment of the passive GNSS network in the ITRF and next its combined adjustment with the terrestrial geodetic network in the NSRS.

In this chapter, a recurrent adjustment method with Givens rotation had been represented for solving the above mentioned task on an account of its abilities to use the technique of sparse matrix, to detect outliers in the recurrent adjustment process and to find them, especially to use effectively results of the separate adjustment of the passive GNSS network in the ITRF for creating the system of observation equations (46) and its realization in the process of the combined adjustment of the passive GNSS network with the terrestrial geodetic network in the NSRS.

In this chapter, the method of the temporary fixation of an initial point used for the separate adjustment of the passive GNSS network in the ITRF had been represented. The abovementioned temporary fixation of an initial point allows not only to perform the strict adjustment of the passive GNSS network in the ITRF and to avoid the singularity of transformed matrix but also to correct the spatial coordinates of fixed point after the combined adjustment of the GNSS network in the NSRS. Additionally, the temporary fixation of the initial point does not cause any influence to the results of the above represented combined adjustment.

The results of experiments performed on the basis of the usage of the T-recurrent algorithm for the separate adjustment of the GPS network in the North Vietnam and the its combined adjustment into VN2000–3 D confirmed the significant improvement of positional accuracy of the GPS points in VN2000–3 D and effectivity of the T-recurrent algorithm in mathematical processing of the GPS network for the construction of the national spatial reference frame. Apart from that, after the combined adjustment of the GPS network in VN2000–3 D, the horizontal and vertical position accuracy of the GPS points had reached the few centimeter level. The mean values of the RMS of national ellipsoidal coordinates of GPS points after solving task of the combined adjustments of the GPS network in VN2000–3D are equal to $m_{\tilde{B}} = 0''.0007; \; m_{\tilde{L}} = 0''.0005; \; m_{\tilde{H}} = 0.023 \; m$ ./.

Acknowledgements

The author is thankful to InTech Open for invitation and helps to write this chapter in book project "Positioning Accuracy of GNSS methods".

Author details

Ha Minh Hoa

Address all correspondence to: minhhoavigac@gmail.com

Vietnam Institute of Geodesy and Cartography, Hanoi, Vietnam

References

[1] Active GPS and Survey Marks. Paper Prepared by ICSM Geodesy Group 2008. Executive Summary. http://www.icsm.gov.au/publications/ActiveGPSAndSurveyMarks.pdf

[2] Biagi L, Caldera S, Crespi M, Manzino AM, Mazzoni A, Roggero M, Sansò F. A zero order network of permanent GNSS stations for positioning services in Italia: Some hypotheses and tests. In: Print on EUREF2007 Workshop Proceedings, 2007a. 2007. 13 p

[3] Canadian Spatial Reference System (CSRS). Natural Resources Canada http://www.nrcan.gc.ca/earth-sciences/geomatics/geodetic-reference-systems/9052

[4] Craymer MR. The evolution of NAD83 in Canada. Geomatica. 2006;**60**(2):151-164

[5] Demidenko, E.Z, 1981. Linear and Nonlinear Regression. Moscow, Finances and Statistics. 302 p

[6] Doskocz A. The current state of the creation and modernization of national geodetic and cartographic resources in Poland. Open Geosciences. 2016, 2016;**8**:579-592. De Gruyter Open. DOI: 10.1515/geo-2016-0059

[7] Doyle DR. Development of the National Spatial Reference System. American Congress on Surveying and Mapping, August 1994. https://www.ngs.noaa.gov/PUBS_LIB/develop_NSRS.html

[8] Doyle DR. Elements of the National Spatial Reference System, Minerals Management Service; September 13, 2000. 62 p., info_center@ngs.noaa.gov

[9] Draznhuk AA, Lazarev XA, Makarenko NL, Demianov GV, Zubinskii VI, Ephimov GN, Maksimov VG. Accomplishment of Adjustment of State Geodetic Network and Usage of New National Geodetic Coordinate System. Report at Techno – Scientific Conference on "Status and Perspective for Geodesy, Aerophotogrammetry, Cartography and GIS", Part I. Moscow: TXNHIIGAiK; 1998. pp. 11-20

[10] Gentlemen WM. Row elimination for solving sparse linear systems and least squares problems. In: Numerical Analysis. Lecture Notes in Mathematics. 1976;**506**:122-133

[11] Fletcher R, Grand JA, Hebden MD. The calculation of linear least L_p-approximations. Computer Journal. 1971;**14**(3):277-279

[12] George A, Heath MT. Solution of sparse linear least squares problems using Givens rotation. Linear Algebra and its Applications. Elsevier; 1980;**34**:69-83

[13] Golub GH, Plemmons RJ. Large scale geodetic least squares adjustment by dissection and orthogonal decomposition. Linear Algebra and its Applications. Elsevier; 1980;**34**:3-27

[14] Gowans N. GDA2020 in NSW. Proceedings of the 22th Association of Authority Surveyors Conference (APAS2017), Shoal Bay, New South Wales, Australia, 20–22 March Vol. 2017. 2017. 11 p

[15] Hoa HM. Once more about recurrent adjustment of dependent measurements. Scientific Journal Izvestiya Vuzov Geodesy and Aerophotography. 1992;**2**:37-47. Moscow University of Geodesy and Cartography (MIIGAiK). ISSN: 0536-101X. Federasion of Russia. www.elibrary.ru

[16] Hoa HM. Methods for combination of terrestrial and satellite geodetic networks with application of Givens rotation. Scientific Journal Izvestiya Vuzov Geodesy and

Aerophotography. 1995a;**1**:54-66. Moscow University of Geodesy and Cartography (MIIGAiK). ISSN: 0536-101X. Federasion of Russia. www.elibrary.ru

[17] Hoa HM. A modification of Givens – Gentlemen's schema for recurrent adjustment with application of rotation method. Scientific Journal Izvestiya Vuzov Geodesy and Aerophotography. 1995b;**3**:38-51. Moscow University of Geodesy and Cartography (MIIGAiK). ISSN: 0536-101X. Federasion of Russia. www.elibrary.ru

[18] Hoa HM. Recurrent Adjustment Method with Rotation. Hanoi: Science and Technique Publisher; 2013. 287 p

[19] Hoa HM, Lau NN. Theory and practice of satellite geodesy. Hanoi: Science and Technique Publisher. 276 p; 2013

[20] Hoa HM. Method for Mathematical Processing of National Geodetic Networks. Hanoi: Science and Technique Publisher; 2014. 244 p

[21] Hoa HM. Development of national hight system of the Vietnam based on geopotential of local geoid. Scientific Journal Izvestiya Vuzov Geodesy and Aerophotography. 2015;**2**:10-13. Moscow State University of Geodesy and Cartography. ISSN: 0536-101X. Federasion of Russia. www.elibrary.ru

[22] Hoa HM. Construction of initial national quasigeoid model VIGAC2017, First step to national spatial reference system in Vietnam. Vietnam Journal of Earth Sciences. 2017a; **39**(2):155-166. DOI: 10.15625/0866-7187/39/2/9702. Vietnam Academy of Science and Technology, http://www.vjs.ac.vn/index.php/jse

[23] Hoa HM. Using of collocation method for determination of geopotential at GNSS point based on geopotentials of first, second orders stable benchmarks and EGM2008. Scientific Report in Proceedings of the 15th Conference on Science and Technology, Geomatics Engineering Section, pp. 1–13, Ho Chi Minh University of Technology, Vietnam National University HCMC; October 20th 2017; 2017b

[24] Hoa HM. Improvement of the accuracy of the quasigeoid model VIGAC2017. Vietnam Journal of Earth Sciences. 2018;**40**(1):38-45. DOI: 10.15625/0866-7187/40/1/10914. Vietnam Academy of Science and Technology, http://www.vjs.ac.vn/index.php/jse

[25] Ihde J. Status of the European Vertical Reference System (EVRS). EVRS Workshop, Frankfurt Main 5–7 April 2004; 2004

[26] Kadaj R. The combined geodetic network adjusted on the reference ellipsoid – A comparison of three functional models for GNSS observations. Geodesy and Cartography. 2016; **65**(2):229-257. Polish Academy of Sciences. DOI: 10.1515/geocart-2016-0013

[27] Landau H. GPS baseline vectors in a three-dimensional integrated adjustment approach. In: Landau H, Eissfeller B, Hein G, (editors). GPS Research 1985 at the Institute of Astronomical and Physical Geodesy. Heft 19;1986. pp. 127-159. ISBN: 0173-1009

[28] Luong Thanh Thach. Research of ability of accuracy improvement of national geodetic heights due to solving of task of the combined adjustment of the terrestrial geodetic and

GNSS networks in the NSRS VN2000-3D. Journal of Geodesy and Cartography. 2017;**33** (September 2017):11-18.Vietnam Institute of Geodesy and Cartography, ISSN: 0866-7705

[29] Markuze YI. Adjustment of geodetic networks with outlier detection. Scientific Journal Izvestiya Vuzov Geodesy and Aerophotography. 1989;**5**:9-18. Moscow State University of Geodesy and Cartography (MIIGAiK). ISSN: 0536-101X. Federasion of Russia. www.elibrary.ru

[30] Markuze YI. Bases of Adjustment Calculation. Moscow, Nedra. 1990. 290 p

[31] Markuze YI, Welsch WM. Two algorithms of combination of terrestrial and satellite geodetic networks. Scientific Journal Izvestiya Vuzov Geodesy and Aerophotography. 1995;**2**:45-64. Moscow State University of Geodesy and Cartography (MIIGAiK). ISSN: 0536-101X. Federasion of Russia. www.elibrary.ru

[32] Mudrov VI, Kusko VL. Methods for Processing of Measurements. Moscow, Sov. Radio; 1976. 192 p

[33] NAD83 (NSRS2007) National Readjustment. https://www.ngs.noaa.gov/NationalReadjustment/

[34] NOAA/NOS's VDatum: A Tutorial on Datums https://vdatum.noaa.gov/docs/datums.html

[35] Roman D. The U.S. National Spatial Reference System in 2022 (8841). FIG Working Week 2017: Surveying the World of Tomorrow – From Digitalisation to Augmented Reality, Helsinki, Finland, May 29 – June 2, 2017

[36] Sacher M, Ihde J, Liebsch G, Mäkinen J. EVRF as Realization of the European Vertical Reference System. EUREF Symposium, June 17–21 2008, Brussels; 2008. 25 p

[37] Sánchez L. Definition and Realization of the SIRGAS Vertical Reference System within a Globally Unified Height System. Dynamic Planet, International Association of Geodesy Symposia, Vol. 130. Berlin, Heidelberg: Springer; 2007. pp. 638-645. DOI: 10.1007/978-3-540-49,350-1_92

[38] Technical Support NAD83 (CSRS), 2016. NOVA SCOTIA https://geonova.novascotia.ca/sites/default/files/resource-library/NSCRS%20Technical%20Support

[39] Thanoon FH. Robust regression by least absolute deviations method. International Journal of Statistics and Applications. 2015;**5**(3):109–112

[40] Véronneau M. The Canadian Geodetic Vertical Datum of 2013. Canadian Institute of Geomatics, Ottawa Branch, 29 April 2014, Natural Resources Canada; 2014. 33 p

Edited by Dogan Ugur Sanli

Following the GPS, new GNSS techniques are emerging today. Various surveying and processing methods are available for the analysis of GNSS data. Equipment and software are also varied. The orbit quality, controlled by the system designer, and the IGS are continuously improved. The user is mainly interested in the quality of position and of the deformation rates produced by the GNSS. Hence, research needs to guide the user in terms of selecting the best combination of the available methods and instrumentation to produce the desired accuracy. This book reviews the current available accuracy obtainable using the GNSS methods. In fact, the main aim of this book is to make an impact on young researchers so that they keep updating the accuracy of GNSS for future generations.

Published in London, UK

IntechOpen

ISBN 978-1-83881-824-1